Università degli Studi di Ferrara

DOTTORATO DI RICERCA IN
"SCIENZE CHIMICHE E FARMACEUTICHE"

CICLO XXIX

COORDINATORE Prof. Carlo Alberto Bignozzi

"Synthesis and biological evaluation *in vitro* and *in vivo* of novel potent anticancer agents affecting tubulin polymerization"

Settore Scientifico Disciplinare CHIM/08

Dottorando
Dott. Filippo Prencipe

Tutore
Prof. Pier Giovanni Baraldi

Co-tutore
Prof. Romeo Romagnoli

Anni 2014/2016

Contents

1. Intoduction

During cell division in eukariotyc cells each daughter cell must inherit a complete copy of the mother's genome. In order to ensure this fundamental process, mother cell must first replicate its DNA in the synthetic phase and then, during the mitotic phase of the cell cycle, must separate evenly to the daughter cells one copy of the replicated chromosomes.

Imperfections in both chromosomes replication and segregation events can heavily affect the cell cycle progression leading to genetic instability, aneuploidy and eventually contribute to oncogenesis and tumor malignancy [1,2]

In order to prevent such a dire consequences and ensure a faithful chromosomes segregation, eukaryotic cells have developed highly coordinated control mechanisms of the cell cycle called checkpoints.[3]

The checkpoint control system dictates the progression of the cell cycle by sensing defects that may occur during DNA replication or chromosomes segregation, inducing cell cycle arrest until these are repaired.

When defects are irreparable, the cell undergoes programmed death, apoptosis, by triggering specific biochemical pathways [4].

DNA repair processes and cell cycle checkpoints have been intimately linked with cancer due to their functions regulating genome stability and cell progression, respectively. Notably, cancer cells often are able to by-pass defective checkpoint allowing for uncontrolled cell proliferation.

Therefore, targeting certain processes or proteins involved in the cell cycle machinery could be really effective in pharmacological treatment of cancer. [5]

In particular, among the various strategy developed to block cell cycle, design molecules that bind to tubulin and inhibit the formation of mitotic spindle remains important for the development of anticancer agents [6]

Microtubule-targeted drugs have proven to be one of the most effective class of cancer chemotherapeutic drugs available to date.[7] Among these, paclitaxel and vinblastine are clinically used to treat different human tumours, e.g. ovarian, mammary, lung, and hematological cancers.

More recently has been reported that microtubule-targeted drugs can act as vascular disrupting agents (VDA), rapidly depolymerizing microtubules of the newly formed vasculature to shut down the blood supply to tumors. [8]

However, restrictions due to toxicity, drug resistance, complex formulations and limited bioavailability highlight the need for novel tubulin inhibitors.

2. Microtubules and tubulin

Microtubules (MTs), key components of cytoskeleton of all eukaryotic cells, are dynamic tubular proteins essential in a variety of fundamental cellular processes, including mitosis, formation and maintenance of cell shape, regulation of motility, cell signaling, secretion and intracellular transport.

MT are long hollow tubes of about 250 Å in diameter that are assembled from α-tubulin/β-tubulin (αβ-tubulin) heterodimers in a GTP-dependent manner.

The αβ subunits form heterodimers which interact in head to tail manner to form a protofilament. The tubulin (TB) subunits make two types of filament contacts: longitudinal contacts run the length of the microtubule forming protofilaments, and lateral contacts between protofilaments (generally α-tubulin to α-tubulin and β-tubulin to β-tubulin) form the circumference of the microtubule.

About 13 protofilaments associate in parallel making the microtubule wall and giving rise to a polymer with a well-defined polarity. Adjacent protofilaments are offset axially, resulting in a helical of lattice of monomers. (Figure 1)

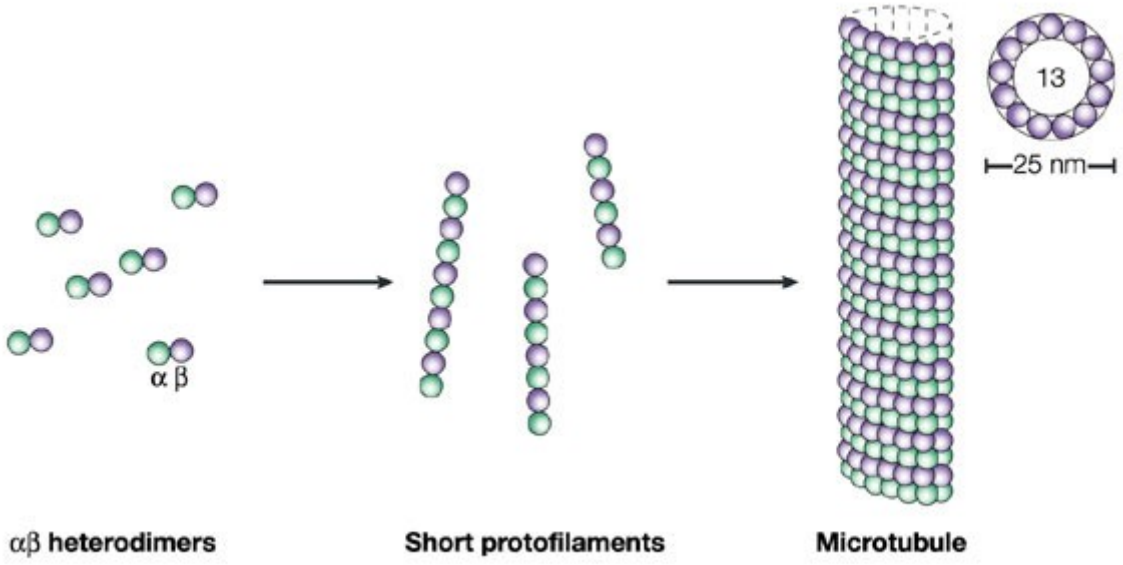

Figure 1. Microtubule components

The structures of α- and β -tubulin are basically identical: each monomer is formed by a core of two β-sheets surrounded by α-helices.

The monomer structure is very compact, but can be divided into three functional domains: the amino-terminal domain containing the nucleotide-binding region (residues 1 to 205), an intermediate domain containing the Taxol-binding site (residues 206 to 384), and the carboxy-terminal domain (residues 385 to the C-terminus), which probably constitutes the binding surface for motor proteins [9].

The α- and β -tubulins share 40% amino-acid sequence identity, both exist in several isotype forms, and both undergo a variety of posttranslational modifications.

Each tubulin monomer binds a guanine nucleotide, which is nonexchangeable when it is bound in the α subunit, or N-site, and exchangeable when bound in the β subunit, or E-site. [7]

Tubulin dimer structure has been solved at 3.7 Å by electron crystallography of the two-dimensional crystalline sheets of TB that form in the presence of zinc ions (Figure 2) [9].

The model indicates that the α,β heterodimer takes on a straight conformation within the protofilaments, the same conformation found in microtubules. In contrast with Zn-sheets, microtubules are formed by the parallel association of protofilaments.

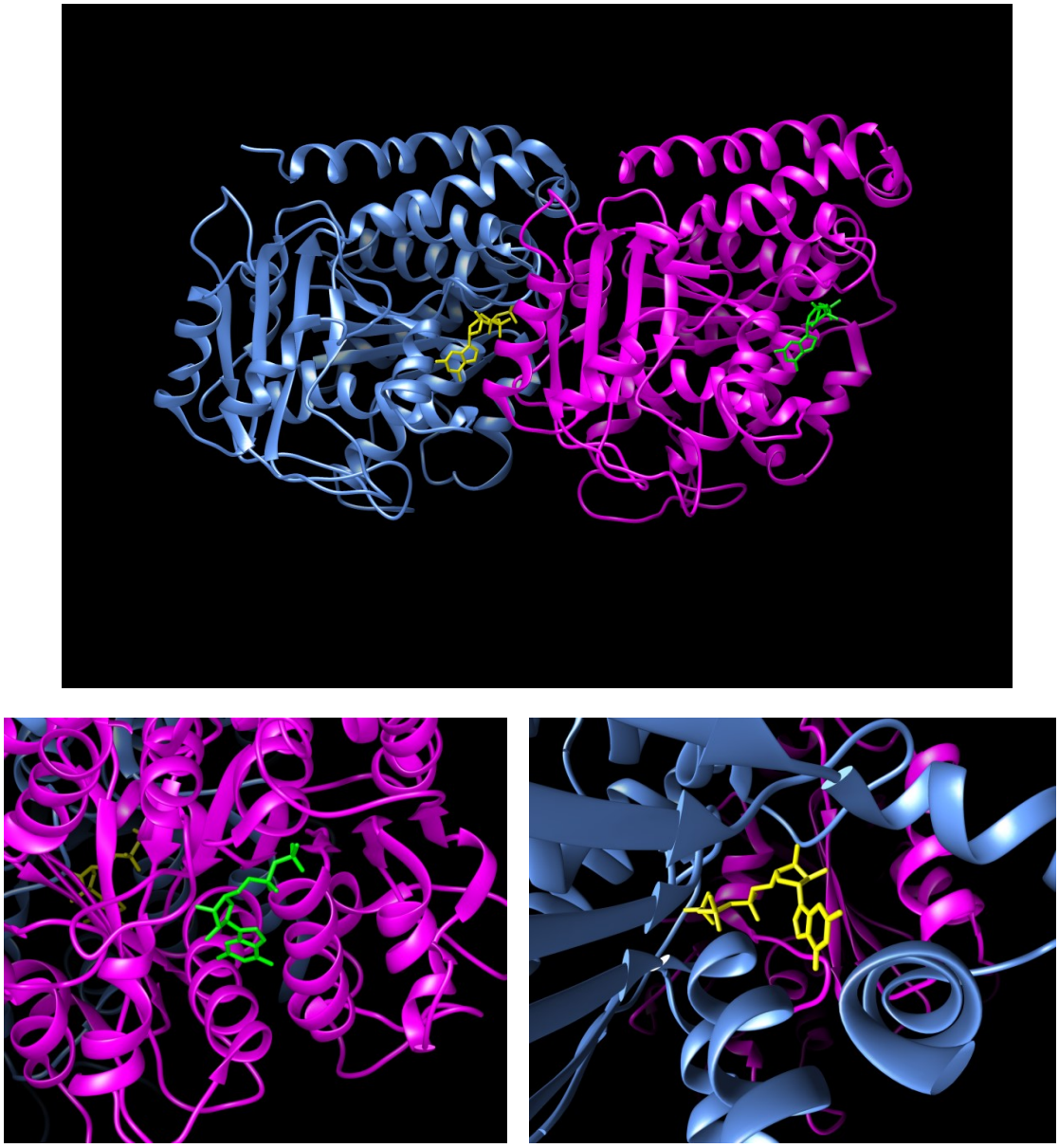

Figure 2. Ribbon diagram of the electron crystallography structure of zinc-induced αβ-tubulin sheets (α-tubulin in blue, β-tubulin in magenta, GDP in green, GTP in yellow; PDB code: 1JFF

Moreover it has been also reported the structure, at 3.5Å resolution, of tubulin in complex with the stathmin-like domain (SLD) protein. [10] (figure 3)

Stathmin is a 17 kDa ubiquitous cytosolic phosphoprotein that sequesters two tubulin heterodimers preventing the incorporation of the complexed tubulin into microtubules.

The model shows the interaction of RB3-SLD with two tubulin heterodimers in a curved complex capped by the SLD amino-terminal domain, which prevents the incorporation of the complexed tubulin into microtubules.

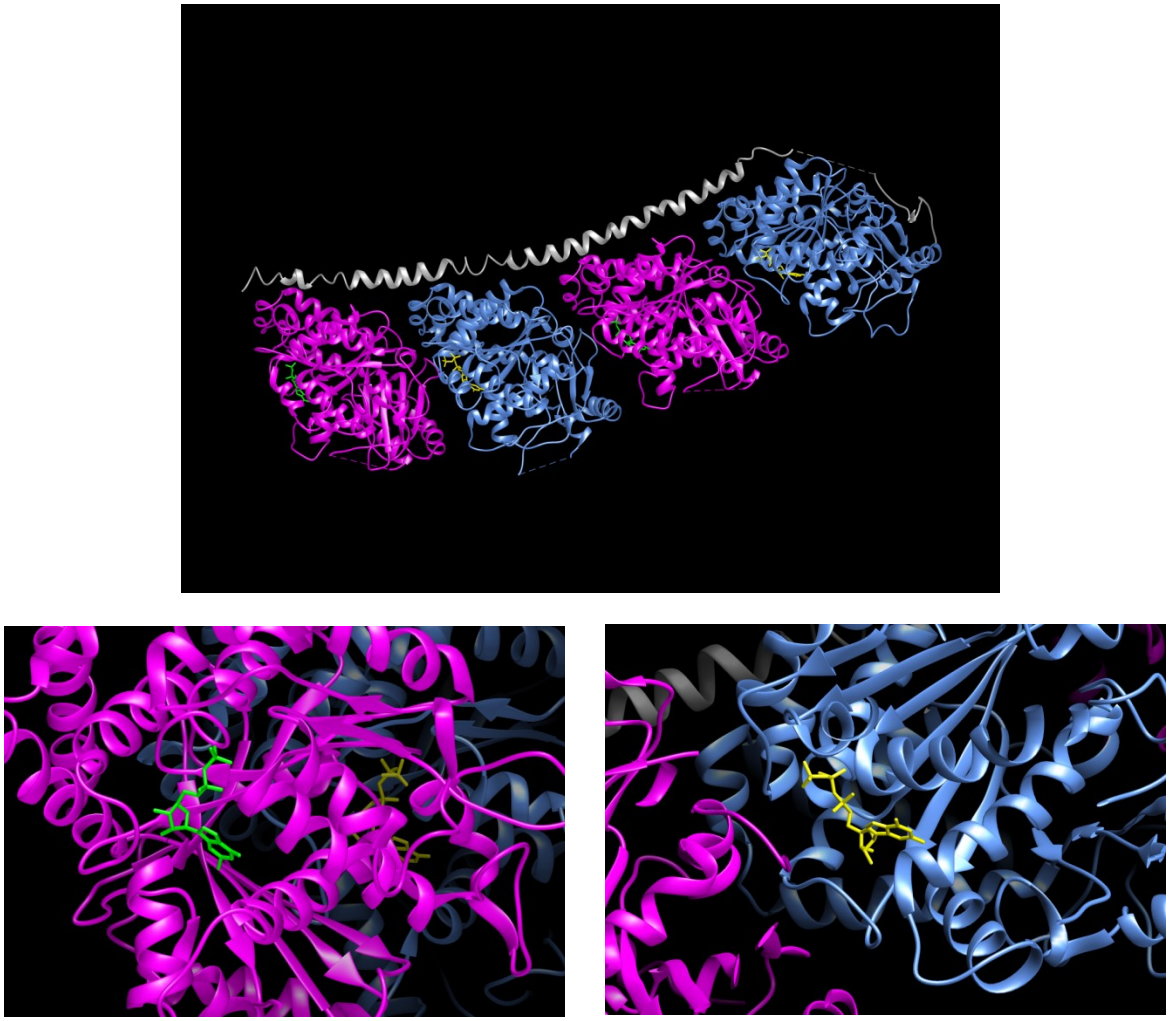

Figure 3. Ribbon diagram of the X-ray structure of tubulin(α1β1α2β2)/ stathmin-like domain complex (α1-, α2-tubulin in blue, β1-, β2-tubulin in magenta, GDP in green, GTP in yellow, stathmin-like domain in gray; PDB code: 1SA0

A comparison with the structure of tubulin in protofilaments and Zn-sheets shows changes in the subunits of tubulin as it switches from its straight conformation to a curved one[10].

These conformational changes affect lateral contacts between tubulin monomer and provide a rationale for the rapid microtubule depolymerization process.

The specific parallel interaction of protofilaments gives rise to a well-defined polymer polarity (figure 4a).

The plus end of the microtubule is capable of rapid growth and is kinetically more dynamic than the minus end, which tends to lose subunits if not stabilized. Although both ends alternately grow or shorten, net growing occurs at the plus end and net shortening at the minus end. [11]

The centrosome, organized around a pair of centrioles, cylindrical structures arranged at right angles to each other in an L-shaped configuration, serves as the central anchor point for microtubules within the cell and represents the site from which microtubules are nucleated [12].

The plus ends of the microtubules are often free in the cytoplasm or located near the plasma membrane, whereas the slow-growing or minus ends of the microtubules are frequently associated at a single site in the cell named the microtubule organizing center (MTOC) or centrosome.

Contained within the MTOC is another type of tubulin, γ-tubulin, which shows a 28- 35% homology with α- and β-TB and is expressed in lower amounts than these latter isoforms.

The γ-tubulin combines with several other associated proteins to form a lock washer-like structure known as the "γ-tubulin ring complex" (γ-TuRC). This complex acts as a template for α/β-tubulin dimers to begin polymerization; it acts as a cap of the (−) end while microtubule growth continues away from the MTOC in the (+) direction. [12, 13]. (Figure 4)

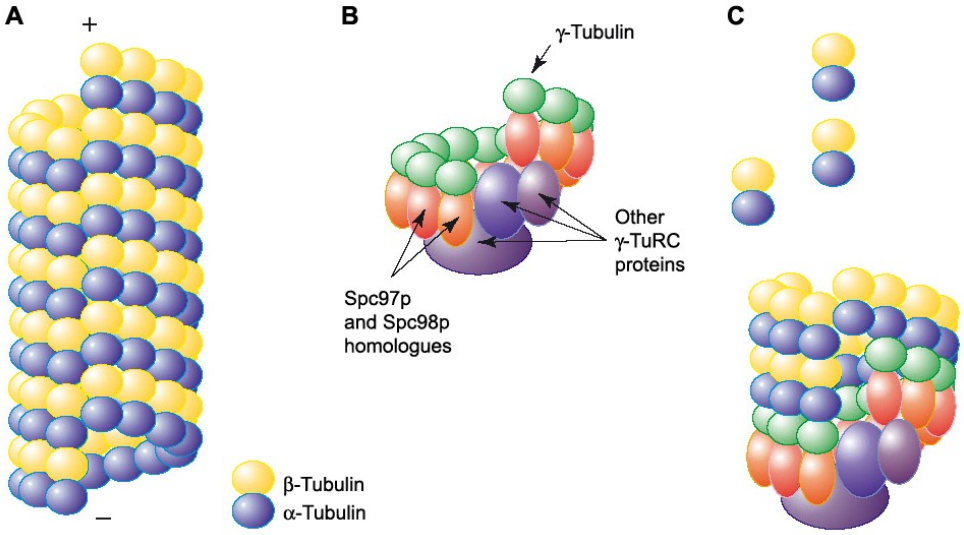

Figure 4. A: Schematic diagram of a microtubule. **B**: Model for the structure of the γ-tubulin ring complex (γ-TuRC). **C**: Microtubule nucleation by the γ-TuRC

Microtubules display rapid polymerization dynamics that are of clear importance to maintaining morphology of microtubule array.

The polymerization of microtubules occurs by a nucleation-elongation mechanism in which the slow formation of a microtubule "nucleus" is followed by rapid elongation at its ends by the reversible non-covalent additions of αβ-tubulin dimers.

Microtubule are not simple equilibrium polymers; their complex polymerization dynamics are modulated by GTP hydrolysis. Their biological functions are determined and regulated mainly by their polymerization dynamics [14,15].

Microtubules show two kind of non-equilibrium dynamics, both in vitro and in cells. (Figure 5)

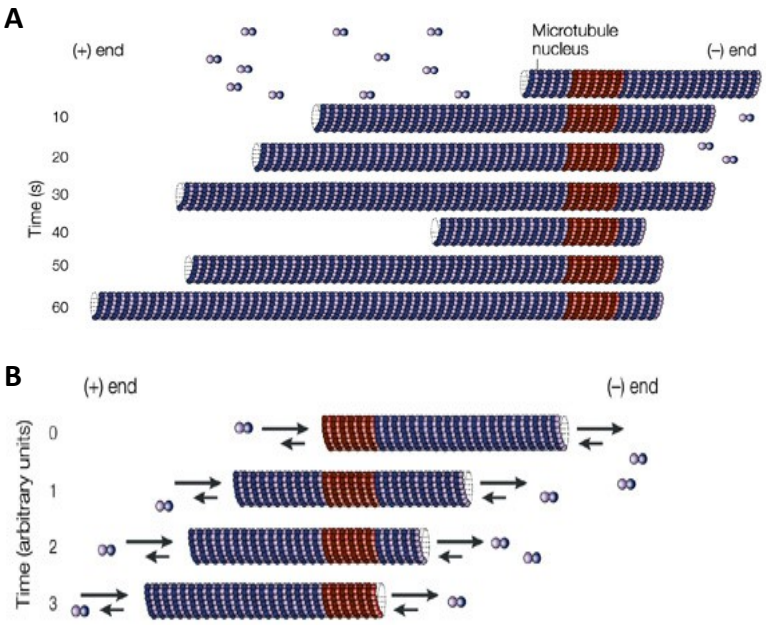

Figure 5. Different movement of the tubulin heterodimer involved into the dynamic instability (**A**)

and the treadmilling (**B**).

The first dynamic behavior, proposed in 1984 by Mitchison and Kirschner, is called "dynamic instability". It is a process in which microtubules ends switch between phases of growth and shortening , undergoing period of slow lengthening, brief period of rapid shortening (called catastrophe) and period of pause (rescue) [16,17].

This mechanism of microtubules assembly/disassembly has been observed both in *vitro* [18] and in living cells [19].

The other dynamic behavior, called "treadmilling"is characterized by unidirectional flux of tubulin subunits from plus to minus end of the microtubule and is generated by differences in the critical subunits concentrations at the opposite microtubules ends.

This intrinsic flux at steady state occurs in cells [20] as well as *in vitro* [19] and might be particularly important in mitosis.

Both dynamic instability and treadmilling behaviors, as compared with those of most polymers in nature are mechanistically linked to GTP hydrolysis.

The kinetic model of dynamic instability, in which individual ends alternate periods of growth and shrinkage, is based on the formation of a cap of GTP-bound subunits that stabilize growing ends. [21]

Shortly after polymerization GTP is hydrolyzed to GDP, thus retaining GDP- bound form in the growing polymer.

Due to its curved conformation the GDP-bound polymer makes weaker interactions with the other subunits of the lattice compared to the GTP-bound heterodimer causing mechanical stress to accumulate in the lattice.

When the cap is lost by GTP hydrolysis , protofilaments peel outward allowing microtubule depolymerization. The free energy of GTP hydrolysis drives the depolymerization process instead of polymerization, enabling polymers to undergo continuous turnover in cells. [14] (Figure 6)

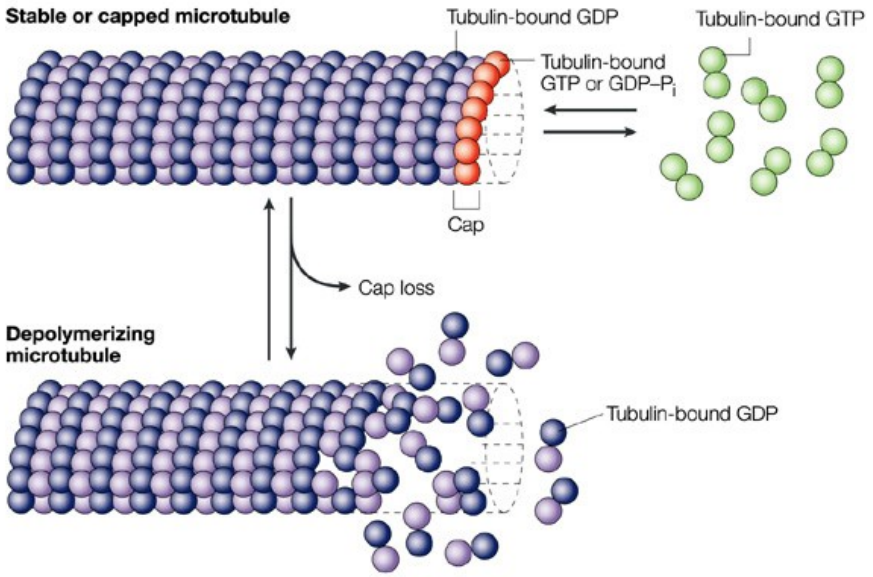

Figure 6. Microtubule polymerization dynamics and GTP cap.

For treadmilling, GTP hydrolysis was proposed to generate the inequality in the critical subunit concentrations at the two polymer ends at steady state, which was necessary to produce net flow of tubulin from one microtubule end to the other. [21]

Both treadmilling and dynamic instability can be produced as distinct phenomena when observing the behavior of microtubules *in vitro* using purified TB, and they have also been observed in living cells[19,20]

In living cells, microtubule's dynamics are regulated both spatially and temporally. In fact, microtubules interact with an impressive number of binding proteins, and cellular microtubule's dynamics are thus the result of the combined effect of stabilizing and destabilizing factors.

Microtubule assembly/disassembly is firstly controlled by a balance between MT stabilizing and destabilizing proteins that bind along the microtubules [22].

Stabilizing proteins include a large group of so-called microtubule associated proteins or MAPs [23] that stabilize MTs against disassembly.

MAPs are targets for protein kinases, including p34cdc2 kinase (cyclindependent kinase 1, CDK1), which control changes in MT dynamic properties at the G2 to M phase transition of the cell cycle. Phosphorylation of MAPs increases during mitosis and reduces their affinity for MTs, thereby reducing their ability to promote MT polymerization [24,25].

Major MAPs include MAP1, MAP2, MAP4 and tau. MAP4 is the most abundant and ubiquitous MAP in non neuronal cells that stabilizes MTs. [26] MAP4 phosphorylation by the cyclin B1/p34cdc2 complex decreases its MT stabilizing ability at mitosis [25].

The destabilizing factors are a growing family of proteins that include Oncoprotein 18 (Op18)/Stathmin, Xenopus kinesin central motor 1 (XKCM1), and katanin [22]. Op18/stathmin is a small protein (19 kDa), highly expressed in leukemic cells, that physically interacts with TB dimers and increases the catastrophe rate of MTs [27,28]. Phosphorylation of Op18/stathmin by p34cdc2 kinase increases the MT catastrophe rate at mitosis [29,30].

XKCM1 is a kinesin-related protein that promotes MT depolymerization during mitotic spindle assembly, and regulates MT dynamics during mitotic spindle assembly [31].

Other MT binding proteins called motor proteins are critical for MT function.

Motor proteins bind to MTs and use the energy derived from ATP hydrolysis to move steadily along it. They can carry membrane-enclosed organelles, such as mitochondria, Golgi stacks, or secretory vesicles, to their appropriate locations in the cell, and cause cytoskeletal filaments to slide against each other, a crucial process in cell division.

Two major classes of MT dependent motor proteins are collectively grouped as kinesins and dyneins, which in turn comprise a great number of proteins [32].

Most of the kinesin superfamily proteins (KIFs) have specific roles in mitotic spindle formation and chromosome separation during cell division as well as in transport, and walk toward the plus end of the MT. However, *C*-terminal motor domain-type KIFs (KIFCs), including KIFC3, travel towards the minus end of MTs.

Dyneins are a family of minus end-directed MT motor proteins, less diverse than kinesins, and play an important role for vesicle trafficking as well as for the appropriate localization of intracellular organelles. Kinesins and dyneins generally move in opposite directions along MTs, and thereby control bi-directional vesicle transport [32].

3.Tubulin targeting agents in cancer chemotherapy

Microtubules are critical for a number of cellular processes, the most recognized being the assembly of mitotic spindle during cell division. Moreover, in the cancer context, they also play a central role in intracellular trafficking by transport of crucial onco-protein, cell migration, and endothelial cell shape changes involved in angiogenesis.

Their crucial role in vital cellular functions and their highly dynamic behavior have made microtubules an excellent drug target for chemotherapy

A large number of chemically diverse compounds, many of which are derived from natural products, bind to soluble tubulin and/or directly to tubulin in microtubules. Most of these compounds show interesting antimitotic properties and inhibit cell proliferation by acting on the polymerization dynamics of mitotic spindle microtubules, the functions of which are extremely important in the proper formation of the mitotic spindle.

The specific effect of individual Microtubule Targeting Agent (MTAs) on stability and dynamics of microtubules are complex. MTAs are usually divided into two main groups. One group, known as Microtubule-Stabilizing Agents (MSAs) such as Taxol™, Taxotere™, eleutherobins, epothilones, laulimalide, and discodermolid, block disassembly of the GDP-bound form of tubulin thus stabilizing the microtubule lattice.

The second main group, known as Microtubule-Destabilizing Agents (MDAs) comprising *Vinca* alkaloids, cryptophycins, halichondrins, estramustine, and colchicine, bind to tubulin dimers and prevent their assembly into MTs and/or induce depolymerization at high concentration.

This classification is made based on the effects of the two main class of compounds at high concentrations where they show opposing effects on tubulin polymer mass.

In particular MDAs induce microtubules depolymerization with net reduction of polymer mass [33] whereas MSAs stabilize growing microtubules increasing polymer mass. [34,35]

However, at 10-100 fold lower concentrations both MDAs and MSAs powerfully suppress microtubules dynamics, dynamic instability and treadmilling, *in vitro* and in cells, therefore stabilizing microtubules without change in polymer mass.[36,37,38].

These observations could suggest that for both MDAs and MSAs the common mechanism responsible for their potent antimitotic ability to inhibit cell proliferation and kill tumor cell is likely to be the suppression of spindle microtubule dynamics rather than depolymerization or excessive polymerization of the microtubules, thus slowing or blocking mitosis at the transition from prometaphase/metaphase to anaphase and inducing apoptotic cell death. [39,40] .

The rapid dynamics of spindle microtubule, dynamic instability and treadmilling, are crucial for proper mitotic spindle make up and its functions, above all these rapid dynamics are required to ensure accurate chromosomes movement.

Suppression of spindle microtubules treadmilling and dynamic instability seems to be the reason that makes cellular mitosis so sensitive to MTAs.

Disruption of the spindle functions by MTAs blocks the cell cycle progression at M phase leading to the activation of the mitotic spindle assembly checkpoint.

The specific molecular mechanisms by which MTAs induce cell cycle arrest are complex. Mitotic checkpoint is activated by a number of defects of microtubules-kinetocore interactions including microtubule depolymerization, stabilization of microtubule dynamics [37,40], absence of tension on kinetochore microtubules [41,42], and the presence of kinetochores that are not attached to microtubules [43].

Moreover, another poorly understood aspect of the action of MTAs during mitosis is their effect on centrosomes. Antimitotic drugs may induce a number of defects such as abnormal centriole structure [44]; centrosomes fragmentation [45]; and/or triggering inappropriate centrosome duplication in p53-lacking cells [46]

The mitotic block induced by MTAs can persists for varying lengths of time, depending on the cell type, and most cells exit mitosis and undergo apoptosis. Even if the biochemical events leading to apoptosis are complex and still poorly understood, the evidences indicate that mitotic block of MTAs at concentrations that suppress microtubule dynamics [47] or alter microtubule mass, induces apoptosis [48,49].

A large number of MTAs have been reported to arrest cell cycle in mitosis and both MSAs and MDAs have proven successful in clinic in treating different type of cancers. [50,51].

A relevant weakness is their cytotoxicity on both tumor and normal cells and lack of selectivity due to the fact that the molecular targets of MTAs, microtubules, are present in all cells and are involved in many other cellular processes in addition to mitosis. However, certain properties acquired by the tumour cells make them sometimes more susceptible to be targeted.

In particular, a higher capacity to cell proliferation in some tumors and a high percentage of p53 mutations in tumour cells favors the action of at least some MTAs. [52,53].

Recently it has been observed that several drugs, especially MTAs, can act as Vascular Disrupting Agents (VDAs), targeting the tumor vascular network thus shutting down the existing vasculature and limiting the tumor supplies of oxygen and nutrients trough the blood [8].

VDAs selectively target mature tumor vasculature, which are tortuous immature and composed mainly of rapid proliferating endothelial cells characterized by an high permeability [54] thus particularly sensitive to MTAs compared to normal endothelial cells.

A number of their functions such as migration, proliferation, adhesion and cohesion are largely dependent on structural and functional integrity of their cytoskeleton. MTAs targeting microtubules, essential component of cytoskeleton, act as VDAs inducing change in morphology, loss of cohesion and/or apoptosis, which results into selective collapse of tumor vasculature and tumor necrosis. [55,56].

The use of conventional chemotherapeutic drugs in combination with VDAs could provide a synergistic strategy where the VDAs affect mainly the poorly perfused hypoxic core of the tumor which is poorly responsive to chemotherapy, while the cytotoxics affect the well-perfused peripheral rim [8]

MTAs bind to diverse sites on the tubulin dimer and at different positions within the microtubule and can be classified into three major categories based on their respective TB binding domains which include paclitaxel site binding agents, colchicine site binding agents, and vinca alkaloid site binding agents.

3.1 Paclitaxel site binding agents

Taxoids, a large group of about 300 known antimitotic drugs classified as MSAs, stabilize and promote assembly of microtubules and are cytotoxic to cells. Taxanes bind poorly with soluble tubulin itself, but instead bind directly with high affinity to tubulin along the length of microtubule.

The first marketed taxoid drug was paclitaxel (**1**), which was isolated from the bark of the Pacific yew tree *Taxus brevifolia*[58]. At the beginning its development for clinical use was impeded by the low yields of the drugs produced by the *Taxus brevifolia* tree. Later this issue was overcome with the semisynthetic process from the available 10-deacetylbaccatin III (**2**), an analogue of paclitaxel which is isolated from *Taxus baccata*[59], or the full synthesis of paclitaxel[60].

In 1992 Food and Drug Administation approved paclitaxel (Taxol^{TM}) for the treatment of drug-resistant ovarian cancer and in 1994 for the treatment of breast cancer . Today it is used also for the treatment of non-small-cell lung cancer, small-cell lung cancer, squamous cancer of the head and neck and various other cancer. [61].

Taxol appears to arrest cells in mitosis by stabilizing the highly dynamic spindle microtubules [62].The specific effects of taxol on microtubule polymerization dynamics are complex and vary with the stoichiometry of taxol binding to the microtubule [62].

At relatively high concentration (1-20 μM), both *in vitro* with bovine brain microtubules and in cells, taxol induces microtubule polymerization increasing polymer mass, massive assembly of microtubules ("bundling") and lead to an abnormal morphology of the spindle which block cell in mitosis [62-64], whereas at low concentrations (10-100 nM) taxol fully stabilizes spindle microtubules by suppressing their polymerization dynamics which results in abnormal spindle organization but without increasing microtubules polymerization and in the absence of significant microtubule bundling.

The suppression of spindle microtubules dynamics produces mitotic block than eventually apoptotic cell death [62-64].

The taxane binding site resides within the lumen of the microtubule. It is situated in a deep hydrophobic pocket in β-tubulin at the lateral interface between adjacent protofilaments. [57].

The structure of the TB/paclitaxel complex has been solved at 3.5 Å by electron crystallography, [10] showing that paclitaxel binds β-TB within the lumen of MT (Figure 7).

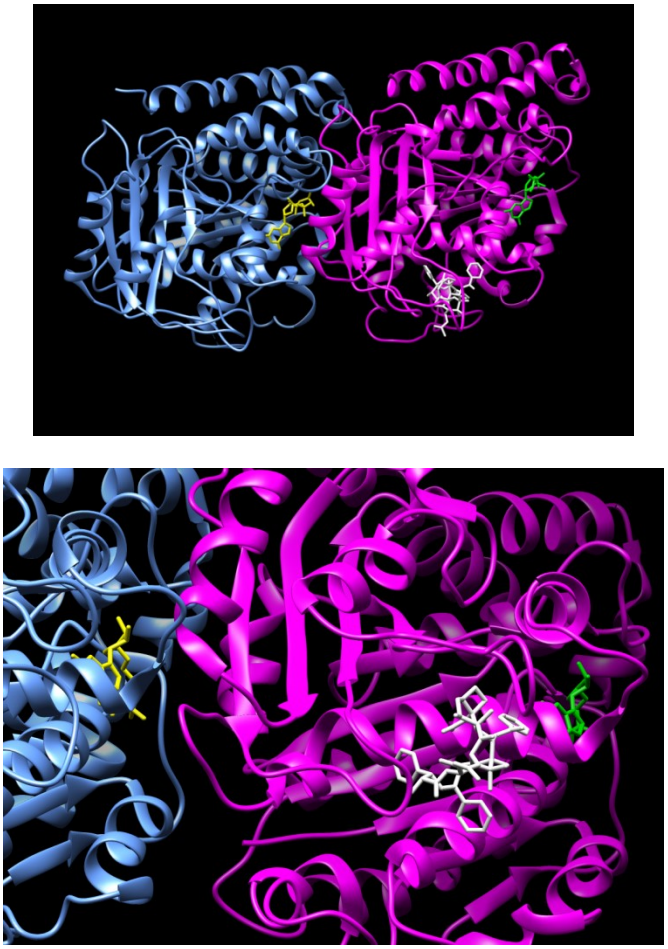

Figure 7. Ribbon diagram of the crystallography structure of αβ-tubulin/paclitaxel complex (α- tubulin in blue, β-tubulin in magenta, GDP in green, GTP in yellow, paclitaxel in white; PDB code: 1JFF

The chemistry of this diterpinoid is very complex comprising of an unusual oxetane ring at C4-C5 and an isoserine side chain at C13 position (figure 8).

Structural changes in the upper part of the molecule, C-6 to C-12 positions, appear to have no significant impact on taxol's activity although some therapeutically active paclitaxel analogues modified at C10 and C2 have been developed as advanced second generation toxoids. [65].

On the other hand, structural modification of the lower part of the molecule, comprising C14 and C1 to C5, exert great influence on taxol's activity. Most changes to the C and D rings, including opening of the oxetane ring, lead to loss of activity [66], although some examples of C ring opened compounds that retain significant activity have been developed [67].

Extensive structure activity relationship (SAR) studies have established that the A ring side chain at C13 with a C2'-OH, the C2 benzoyl group and an intact oxetane ring at C4-C5 are essential for both cytotoxicity and stabilization of MTs.[68,69].

The oxetane ring is a unique feature of paclitaxel and seems to serve as hydrogen-bond acceptor and also as a rigid "lock" on the taxoid skeleton [67].

The C4 acetyl group does not appear to play a significant role in the biological activity but may contribute to the defined conformation of the molecule. The C1-OH group makes a significant contribution to the overall bioactivity where the OH group at C7 is not essential for biological activity [69].

The very low yield, its poor water solubility and drug resistance have motivated researchers to design and develop new analogues of paclitaxel.

Docetaxel (**3**),[73] with minimal structural modifications at C13 side chain and C10 substitution showed more water solubility and more potency than paclitaxel, whereas baccatin, without C13 side chain, has no significant cytotoxicity, thus indicating the importance of the C-13 side chain for biological activity.

The appropriate modifications at C-3' on the isoserine side chain, at C-2 yielded second generation taxoids [70-72] showing high potency against drug resistant cancer cells and among these, compound **4** showed two orders of magnitude greater activity than those of paclitaxel and docetaxel [65].

A series of simplified compounds, typified by compound **5** have been synthesized, retaining only the key pharmacophore properties of paclitaxel, phenylisoserine and an oxetane ring, but none showed promising TB inhibitory activity, confirming the necessity of the diterpene ring [74].

Novel 7-deoxy-9-dihydropaclitaxel analogues, typified by compound **6**, have been synthesised and found to have potent selectivity against human liver cancer cells [75]

The paclitaxel ester of malic acid **7** has demonstrated improved solubility and enhanced *in vivo* antitumor activity against P388 murine leukemia indicating a higher therapeutic index than paclitaxel. [76].

Chemical structures of compounds discussed in this section are presented in Figure 8

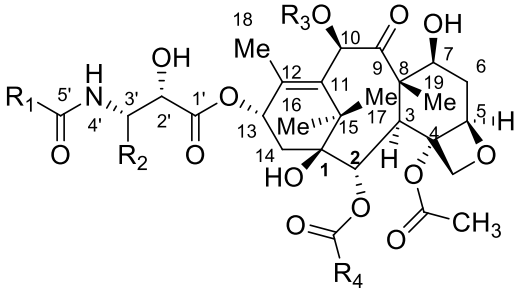

1 Paclitaxel(R_1 = R_2 = R_4 = Ph, R_3 = Ac)

3 Docetaxel (R_1 = R_4 = Ph, R_2 = *t*-BuO, R_3 = H)

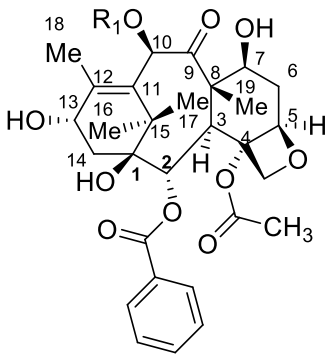

2 Baccatin III (R_1 = Ac)

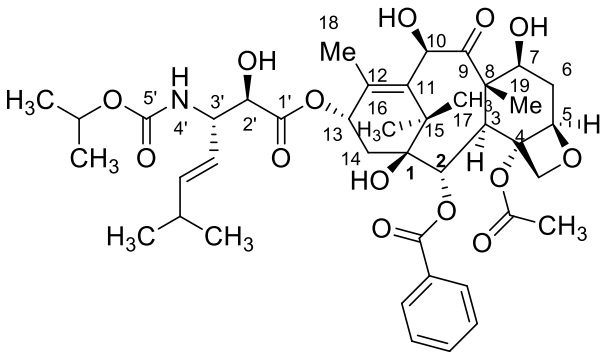

4

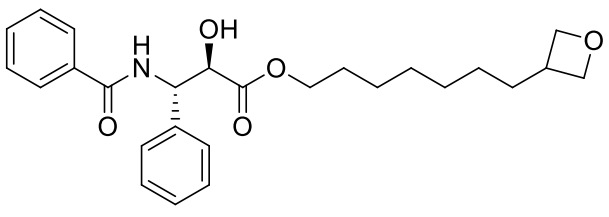

5

Figure 8. Paclitaxel site binding agents

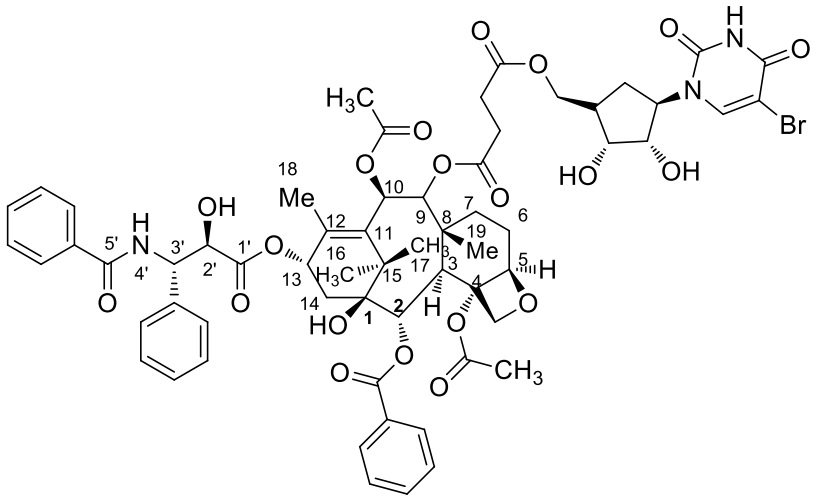

6

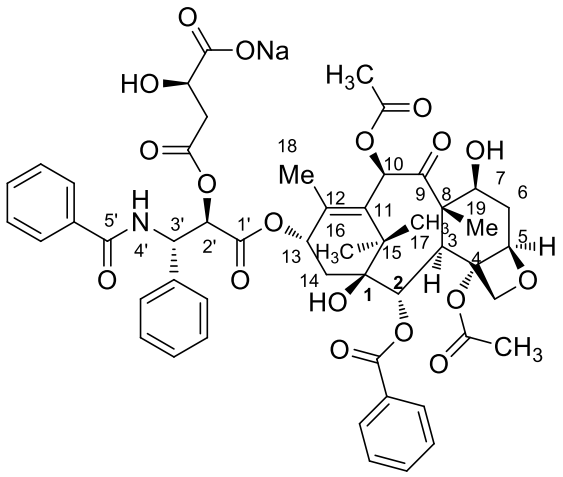

7

Figure 8. Paclitaxel site binding agents (*Continued*)

Vinca alkaloid site binding agents

Vinca alkaloids are a large group of antimitotic anticancer agents classified as MDAs that bind to tubulin at the Vinca domain which is located at the αβ interdimer interface (between two heterodimers) very close to GTP binding site.The binding at this site inhibits the assembly of tubulin, causing a 'wedge' between the two heterodimers.

Vincristine **8** and Vinblastine **9**, two naturally occurring member of this family, were isolated from the leaves of periwinkle plant *Catharanthus roseus* [77,78] and are among the most useful class of antimitotic anticancer agents for the treatment of leukemias, lymphomas and some solid tumours [79,80].

Vinblastine binds to tubulin at microtubule ends with high affinity (Kd, 1-2 μM) whereas it binds with considerably lower affinity (Kd, 0.25-0.3 mM) to tubulin sites located along the sides of the microtubule cylinder. The binding is reversible and independent of temperature [81-83].

The structure of vinblastine bound to the TB/stathmin-like domain/vinblastine complex was determined at 4.1 Å resolution by X-ray diffraction (Figure 11). [80].

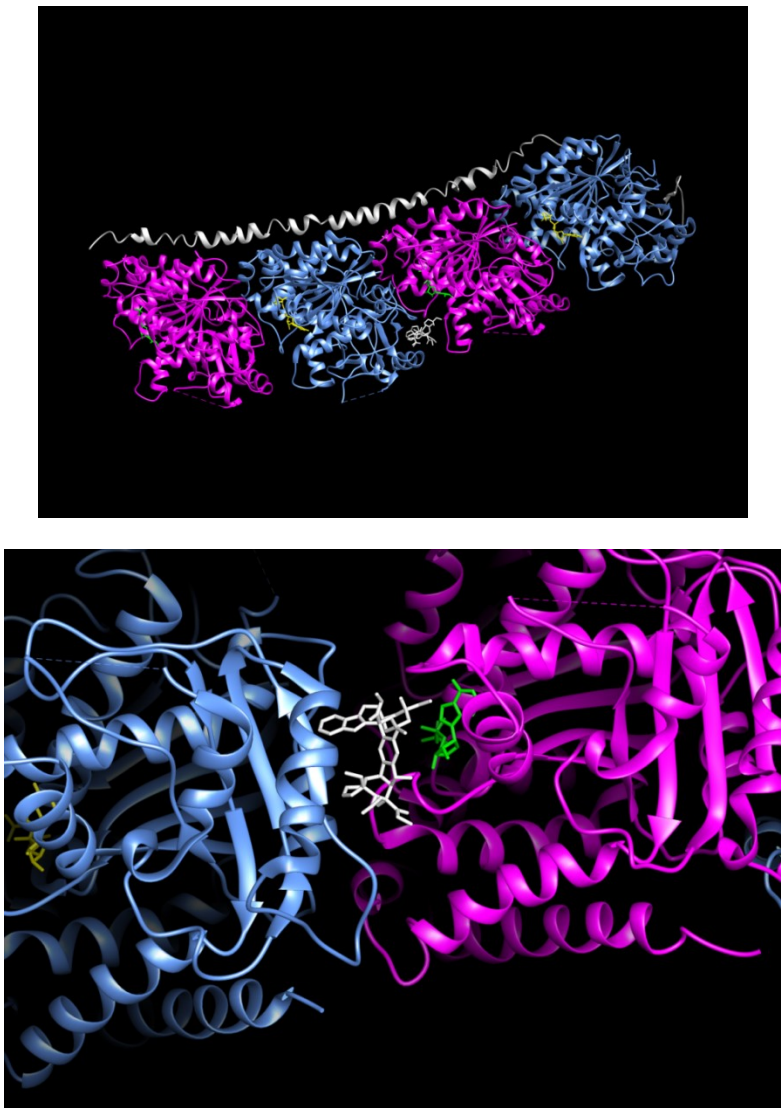

Figure 9 Ribbon diagram of the X-ray structure of tubulin(α1β1α2β2)/stathmin-like domain/vinblastine complex (α1-, α2-tubulin in blue, β1-, β2-tubulin in magenta, GDP in green, GTP in yellow, stathmin-like in gray, vinblastine in white; PDB code: 1Z2B

For many years, Vinblastine was thought to act primarily as a "microtubule depolymerizing agent" [84-85].

However, recent advances have elucidated its potent stabilizing effects on microtubule dynamics at low concentrations in the absence of microtubule depolymerization in a manner somewhat similar to that of taxol. [45].

At high concentration(10-100 nM in HeLa cells) [81]Vinblastine depolymerizes microtubules and destroys the mitotic spindle leaving the dividing cells blocked at the metaphase/anaphase transition.

Al low but clinically relevant concentrations (0.8 nM in HeLa cells) [81], Vinblastine does not depolymerize spindle microtubules, yet it powerfully blocks mitosis and cell die by apoptosis.

Studies on living cancer cells indicate that the mitotic block induced by low concentration of Vinblastin is due to suppression of spindle microtubule dynamics rather than depolymerization.[82].

The suppression of these dynamics prevents the mitotic spindle from assembling properly and reduces the tension at the kinetochores of the chromosomes resulting in the block of the cell at the metaphase/anaphase transition and cells eventually die by apoptosis.

The SAR, pharmacology and clinical uses of vinca alkaloids have been reviewed. [83]. Lots of efforts have been made in order to develop new congeners that are more effective, have less side effects and have a broad spectrum of antitumor activity.

The basic structure of vinca alkaloids is composed of a catharenthine moiety and vindoline nucleus. Most of the semisynthetic or totally synthetic vinca alkaloids drugs have been developed by the modification of C4, C23, C3' and C4' position of parent vinca alkaloids.[83] (Figure 10).

Vindesine **10**, the first semisynthetic vinca alkaloid, was developed by changing the C23 acetyl group in vinblastine to an amide[86].

Modifying the vindoline moiety with L-tryptophane at C23 led to the development of vintripole **11** [87].

Vinxaltin **12** is in phase II clinical trial for advanced breast cancer showing an excellent antitumor profile [87].

Another semisynthetic compound vinorelbine **13** showed promising activity against breast cancer [88] and is in clinical trial for the treatment of other types of tumors [89]. This drug exhibited superior antimitotic activity over others with lower reversible neurotoxicity.

Further modifications in vinorelbine led to the discovery of vinflunine **14** which showed significantly superior anticancer activity *in vivo* as compared to vinorelbine [90].

Chemical structures of compounds discussed in this section are presented in Figure 10.

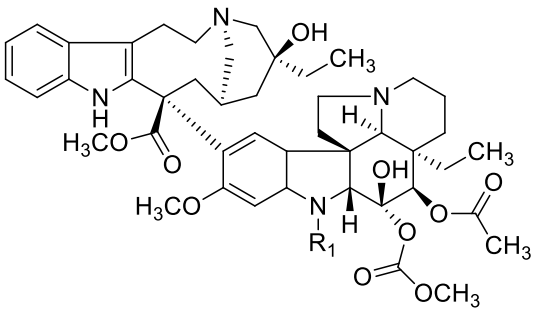

8 Vincristine (R_1 = CHO)
9 Vinblastine (R_1 = CH_3)

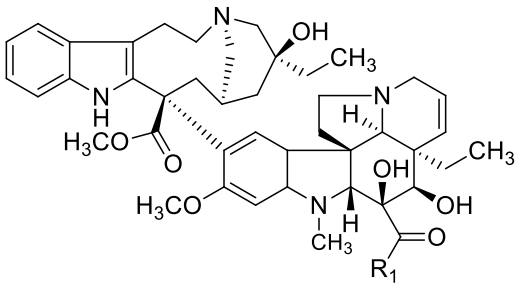

10 Vindesine (R_1 = NH_2)
11 Vintripole (R_1 = L-Trp-OC_2H_5)
12 Vinxaltin (R_1 = D-Vla(P)-$(OC_2H_5)_2$

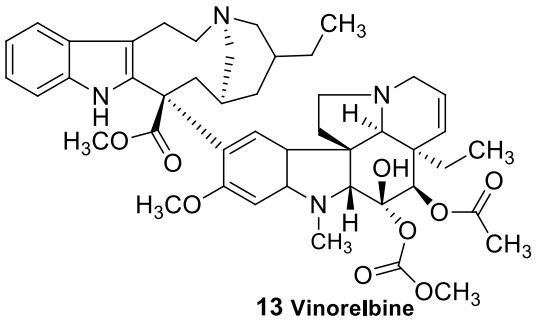

13 Vinorelbine

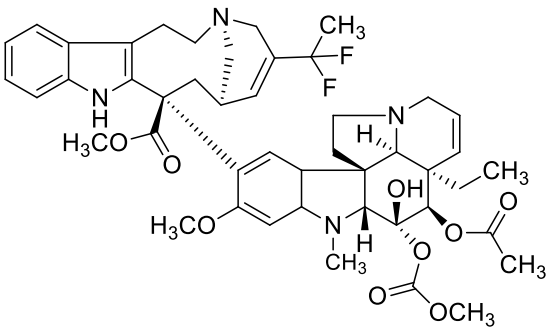

14 Vinflunine

Figure 10. Vinca alkaloid site binding agents

3.3 Cochicine site binding agents

Colchicine **15** is a well-known alkaloid that has played a central role in the discovery of tubulin.

The drug was first isolated from the leaves of meadow saffron (*Colchicum autumnale*) and is used in the treatment of gout, familial Mediterranean fever and liver cirrhosis [91].

Colchicine binds to soluble tubulin, induces a slow conformational change in the tubulin heterodimer forming a poorly reversible tubulin-colchicine complex which than co-polymerize into the microtubules ends in small number along with free tubulin molecules. Due to its conformation, the incorporation of the complex slows new tubulin addition thus suppressing microtubules dynamics. [92]

The colchicine site has been located in a deep pocket at the α-β interface of tubulin heterodimers [93] and the drug binding mode has been confirmed by the determination of a 3.58 Å X-ray structure of TB complexed with *N*-deacetyl-*N*-(2-mercaptoacetyl)colchicine (DAMA-colchicine), which is a close structural analogue of colchicine (Figure 11) [10].

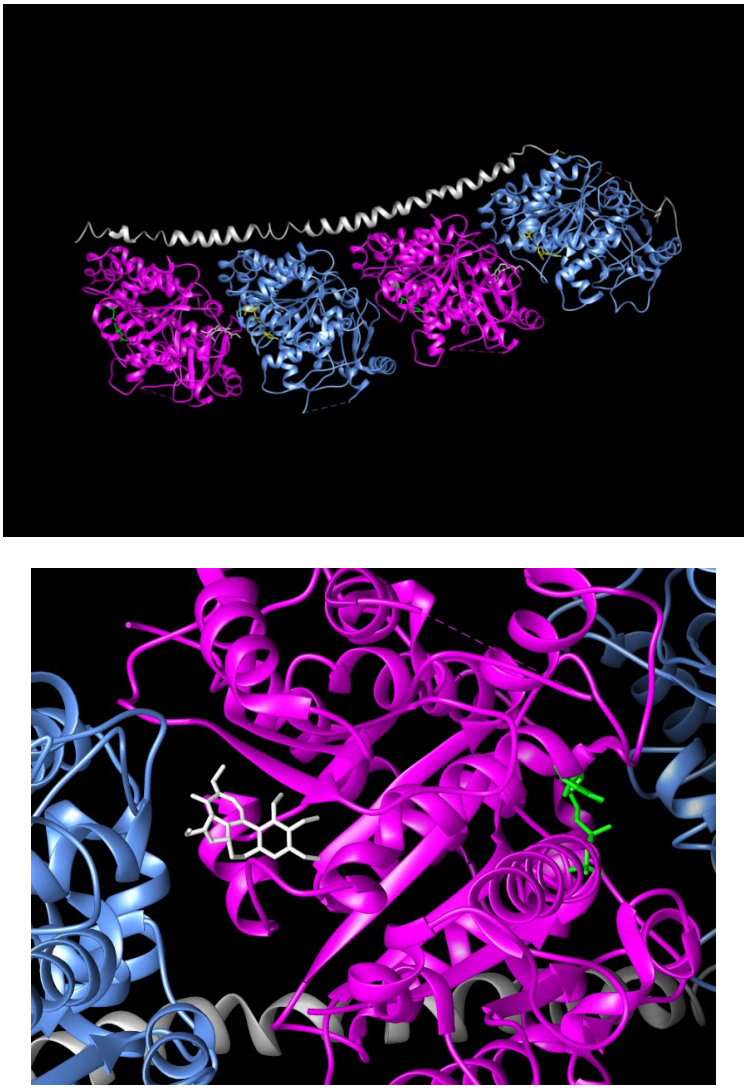

Figure 11. Ribbon diagram of the X-ray structure of tubulin(α1β1α2β2)/stathmin-like domain/DAMAcolchicine complex (α1-, α2-tubulin in blue, β1-, β2-tubulin in magenta, GDP in green, GTP in yellow, stathmin-like domain in gray, DAMA-colchicine in white; PDB code: 1SA0

Like other antimitotic drugs, the effects of colchicine on microtubule dynamics are dependent upon drug concentration. Relatively high colchicine concentrations inhibit microtubule polymerization and depolymerize preformed microtubules. At the lowest effective concentrations, colchicine inhibits microtubule dynamics with no reduction in polymer mass.

Colchicine slows or blocks mitosis at the metaphase/anaphase transition in a number of cell types. In HeLa cells, at high colchicine concentrations (30 nM), microtubule polymerization is inhibited and the mitotic spindle dissociates or is not formed, whereas at low concentrations (<20 nM), mitotic block does not involve significant microtubule depolymerization suggesting that blockage occurs as a result of suppression of microtubule dynamics [82].

The Structure Activity Relationship (SAR) of cochicinoid has been extensively studied [94]. It has been reported that the β-subunit of TB is involved in colchicine binding, with the A ring of colchicine lying between Cys-354 and Cys-239 while the C-ring interacts with the amino terminus of b-tubulin [95].

The seven membered B ring and the C7 side chain are not believed to be crucial for TB binding but may affect the conformation of colchinoids and their TB binding properties [96,97].

The trimethoxyphenyl group of the A ring of colchicine serves as a complex stabilizing anchor on TB in the inhibition of MTs assembly and is essential for its activity. The tropolonic C-ring can be replaced with a phenyl ring bearing a methoxy substituent [98].

It has also been reported that colchicine binds to a second, lower affinity site on tubulin in a reversible manner [99].

Although colchicine is one of the more potent antimitotic drugs, its use in therapy has been limited by its great toxicity. In order to overcome this limit, a great number of cochicine analogues have been prepared in past decades, including compounds isolated from natural sources, partially synthesized from colchicine, and de novo synthesized.

Some have been used clinically as antitumor agents, having less toxicity than colchicine. Colchicone (**16**), a non-nitrogen containing natural product isolated from *Colchicum richterii* and synthesised by Banwell *et al.* has been reported to show an inhibitory effect on TB polymerization [100].

Compound **17**, a bicyclic analogue of colchicine binds rapidly and reversibly to colchicine binding site of TB, inhibits MTs assemble and promotes apoptosis in human leukemic cells. This drug produces reversible effects on MT disassembly, G2/M phase arrest, more water solubility andhas lower toxicity than colchicine [101].

Among colchicine analogues, thiocolchicine (**18**) has shown more activity than the parent colchicine.

Podophyllotoxin (**19**) and its related analogues were isolated from *Podophyllum peltatum* and related species. Podophyllotoxin and its related analogues (**20, 21**) bind to tubulin at the colchicine site and competitively inhibit colchicine binding to tubulin although a recent computer modelling study suggested incomplete overlap of the colchicine and podophyllotoxin binding site(s) [102].

Etoposide (**22**) is a potent topoisomerase II (an enzyme involved in the folding and unfolding of DNA during cell replication) inhibitor but a weak TB inhibitor.

It has also been reported that their predominant function is inhibiting topoisomerase II rather than a microtubule interaction [103].

Etoposide is currently used in the treatment of small cell lung, testicular and malignant lymphoid cancers, among others [104]. It is also used in combination chemotherapy.

Teniposide (**23**) appears to be a less useful clinical agent although it is undergoing trials in combination therapy for the treatment of metastatic brain tumors [105].

Combretastatins are a class of natural stilbenoid phenols originally derived from the African willow tree (*Combretum caffrum*) and are powerful reversible inhibitors of tubulin polymerization [106].

Among these compounds, Combretastatin A-4 (CA-4) (**24)**, a cis-stilbene isolated for the first time by Petit et al. [107], is one of the most potent inhibitors of colchicine binding presently known [108]. CA-4 has been shown to possess a powerful cytotoxic activity against a panel of tumor cell line [108,109], including multi-drug resistant cells [110].

The Structure Activity Relationship of CA-4 has been extensively studied [106,111]. It has been shown that the *cis*-configuration of the double bond and the 3,4,5-trimethoxy group on ring A are fundamental for the optimal interaction with tubulin [106] whereas isosteric substitutions on ring B are well tolerated.

One of the main problem of this relatively chemically simple molecule is the isomerization of the active *cis* double bond to the inactive *trans* which leads to a dramatic loss of antiproliferative activity. It has been demonstrated that it is possible to overcome the problem of isomerization by introducing different heterocycles in place of the olefin group without substantial loss of potency [112].

In vivo, CA-4 displayed low or no antitumoral activity [113] mainly because of low water solubility, and to overcome this limit a disodium phosphate prodrug, CA-4P (**25)** was introduced [114]. CA-4P is under evaluation in phase III trials for the treatment of anaplastic thyroid cancer and in phase II trials for non-small cell lung cancer and platinum-resistant ovarian cancer [115,116].

Recently it has been shown that CA-4 can act as Vascular Disrupting Agent targeting the tumor vascular network and limiting the tumor supplies of oxygen and nutrients trough the blood. [111].

Chemical structures of compounds discussed in this section are presented in Figure 12

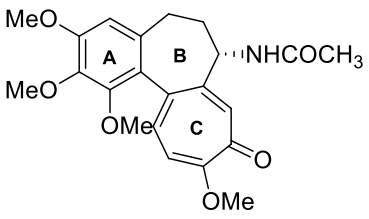

15 Colchicine

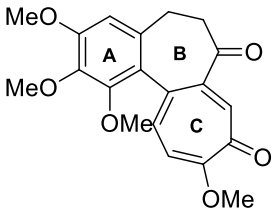

16 Colchicone

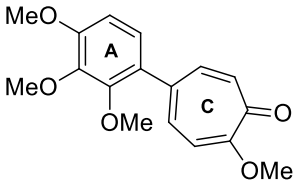

17

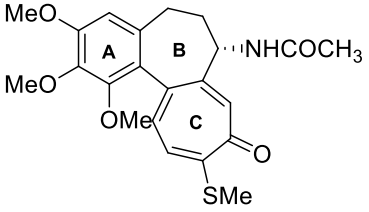

18 Thiocolchicine

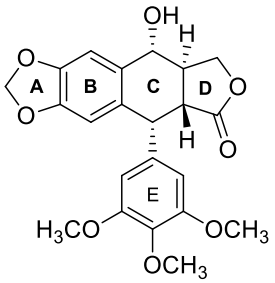

19 Podophyllotoxin

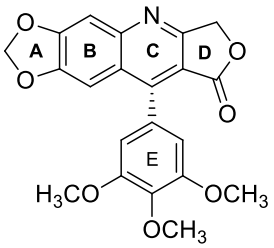

20

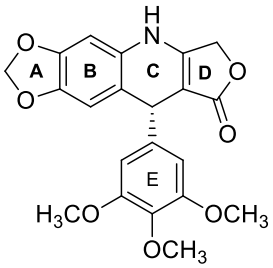

21

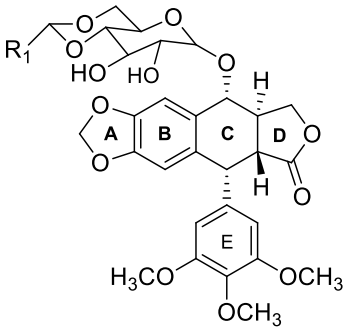

22 Etoposide (R_1 = CH_3)
23 Teniposide (R_1 = 2-Thienyl)

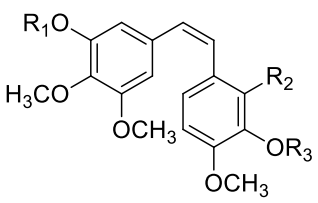

24 Combretastatin A-4 (R_1 = CH_3, R_2 = R_3 = H)
25 Combretastatin A-4P (R1 = CH3, R2 = H, R3 = P(=O)(ONa)2)

Figure 12. Colchicine site binding agents

4. 1-(3',4',5'-Trimethoxybenzoyl)-3-Arylamino-5-Amino-1,2,4-Triazoles:

Synthesis, Antimitotic and Antivascular Activity

Paclitaxel and vinca alkaloids are clinically important chemotherapeutic drugs, and are widely used for the treatment of a variety of tumors. However, side effects and drug resistance reduce their efficacy. Neurological and haematological side effects are the principal and often dose-limiting toxicities [117]. Drug resistance is another factor hampering the clinical applicability of microtubule targeting agents, involving the overexpression of drug efflux pumps, and alterations in tubulin/Microtubules.[118] These findings highlight the need for novel TB dynamic inhibitors. Furthermore, while drugs that act on the vinca and taxane sites have well-established roles in the treatment of human cancers, the therapeutic potential of the colchicine site in cancer treatment has yet to be realized.

Among the naturally occurring antimicrotubule agents, one of the most active is the *cis*-stilbene combretastatin A-4 (CA-4, **1a**, Chart 1), isolated from the African cape bushwillow *Combretum caffrum* [108]. CA-4 inhibits tubulin assembly by strongly binding to the colchicine site on β-tubulin. Its water soluble prodrug, CA-4 disodium phosphate (CA-4P, **1b**) [119], is in advanced clinical trials [115], and it was found to have potent activity in reducing tumor blood flow, thus acting as a vascular disrupting agent (VDA) [120].

Among the synthetic inhibitors of tubulin polymerization, we previously described a series of 2-arylamino-4-amino-5-(3',4',5'-trimethoxybenzoyl)thiazoles with general structure **2** that showed strong antiproliferative activity against a panel of five cancer cell lines [121].

These compounds also caused accumulation of HeLa cells in the G2/M phase of the cell cycle, as is typical for antimicrotubule agents. Derivatives **2a** (R_1=H) and **2b** (R_1=4'-Me) were the most active as inhibitors of tumor cell growth, with IC_{50} values of 6-23 and 15-86 nM, respectively, in the five cell lines.

Ring bioisosterism is widely used as a rational approach for the discovery of new anticancer agents, especially for finding agents with optimal pharmacological properties [106,122].

Continuing our search strategy for novel and potent antimicrotubule agents, we have underway a pharmacophore exploration and optimization effort based on compounds with general formula **2** (Chart 1)..

Here we describe replacing the thiazole nucleus with the more electron-rich 1,2,4-triazole bioisosteric ring [123,124], to afford a new series of 1-(3',4',5'-trimethoxybenzoyl)-3-arylamino-5-amino 1,2,4-triazole analogues with general structure **3** (Chart 1).

Our goal was to evaluate the steric and electronic effects of different substituents on the benzene portion of the arylamino moiety. Besides hydrogen (compound **3a**), the examined substituents included fluorine (**3b**) and electron donating alkyl and alkoxy groups (compounds **3c-h** and **3i-n**, respectively).

Since it is well known that the trimethoxyphenyl skeleton is the characteristic structural requirement to maximize activity in a large series of inhibitors of tubulin polymerization, such as colchicine, CA-4 and podophyllotoxin [125], all newly prepared compounds **3a-n**, retain the 3',4',5'-trimethoxybenzoyl group at the C-1 position of the 1,2,4-triazole ring.

The newly synthesized derivatives were evaluated for their antiproliferative activity in a panel of human cancer cell lines, for their antitubulin activity (including cell cycle and apoptotic effects) and their antivascular activity in HUVEC cells.

Finally, the antitumor activity of **3c**, the most potent member of the group in the *in vitro* studies, was evaluated *in vivo* in a syngeneic hepatocellular carcinoma in Balb/c mice in comparison with CA-4P.

Chart 1. Inhibitors of Tubulin Polymerization

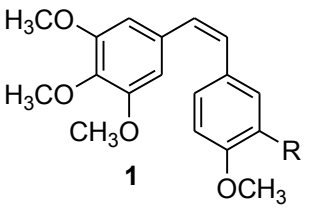

1

R=OH, Combretastatin A-4 (CA-4), **1a**
R=OPO_3Na_2, CA-4P, **1b**

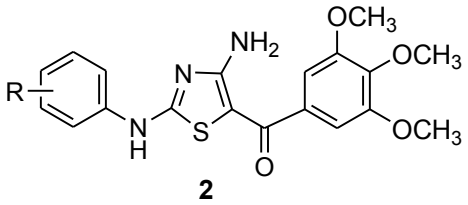

2

R=H, F, Cl, CH_3 and OCH_3
2a, R=H
2b, R=*p*-CH_3

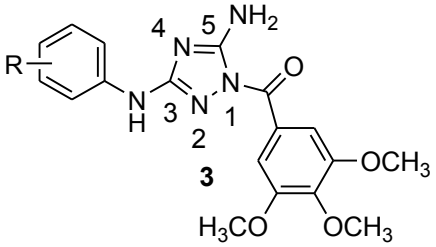

3

3a, R=H
3b, R=p-F
3c, R=p-CH_3
3d,R=m-CH_3
3e, R=m,p-$(CH_3)_2$
3f, R=p-C_2H_5
3g, R=p-$CH(CH_3)_2$
3h, R=p-$(CH_2)_3CH_3$
3i, R=p-OCH_3
3j, R=m-OCH_3
3k, R=m,p-$(OCH_3)_2$
3l, R=m,m',p-$(OCH_3)_3$
3m, R=p-OC_2H_5
3n, R=m,p-(OCH_2O)

4.1 Chemistry

Synthesis of compounds **3a-n** was accomplished using a three-step procedure described in Scheme 1.

The condensation of dimethyl cyanodithioimidocarbonate **4** [126] with the appropriate substituted aniline resulted in the formation of imidates **5a-n**, which were cyclized into the corresponding 5-amino-1*H*-[1,2,4]-triazole derivatives **6a-n** in the presence of hydrazine hydrate in refluxing THF [127].

Treatment of **6a-n** with an equimolar quantity of 3',4',5'-trimethoxybenzoyl chloride resulted in the formation of compounds **3a-n** as the major regioisomers. In the synthesis of compounds **3a-c**, **3g-h** and **3k-l**, the corresponding minor regioisomers **7a-c**, **7g-h** and **7k-l**, respectively, were also isolated in pure form and low yields (5-12%).

Scheme 1

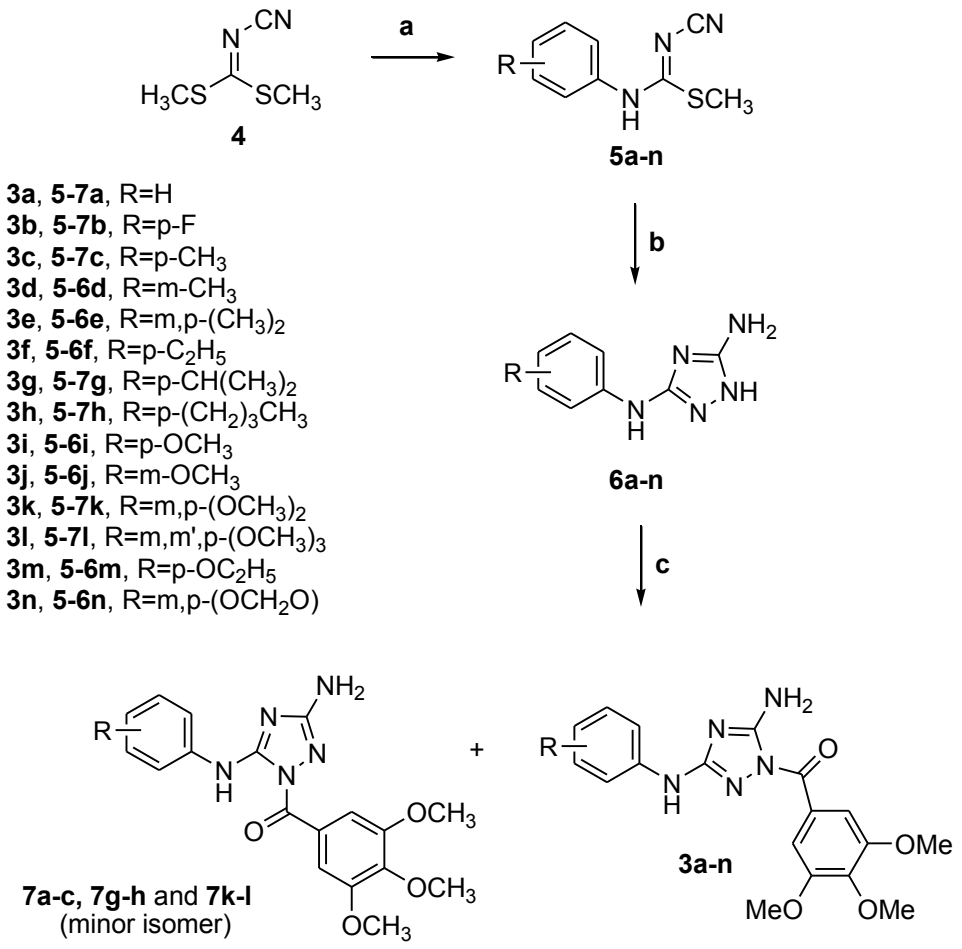

Reagents. **a**: $ArNH_2$, *i*-PrOH, reflux; **b**: $NH_2NH_2 \cdot H_2O$, THF, reflux; **c**: 3',4',5'-$(OMe)_3C_6H_2COCl$, pyridine, 0 °C.

X-ray crystallographic analysis of a representative compound (**3c**) was determined to confirm the regioselective aroylation at the less sterically hindered *N*-1 nitrogen of the 1,2,4-triazole ring. Single crystals of **3c** were grown by slow evaporation from *i*-PrOH-MeOH solution, and the ORTEP view of compound **3c** is shown in Figure 1. The molecule displays an intramolecular N4-H…O1 hydrogen bond having N4…O1 and H…O1 distances of 2.773(3) and 2.12(3) Å, respectively, and an N4-H…O1 angle of 128(2)°.

Figure 1. ORTEP view of compound 3c displaying the thermal ellipsoids at 30% probability

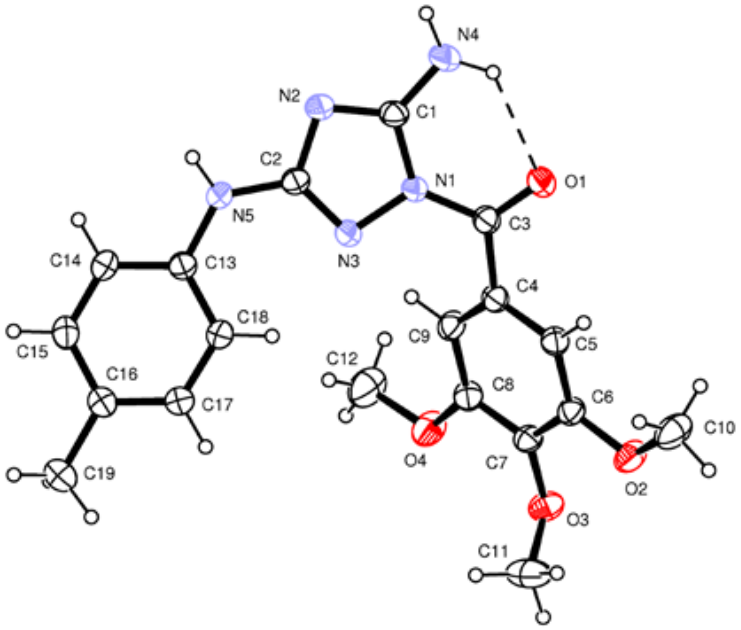

4.2 Biological Results and Discussion

***In vitro* antiproliferative activities.** Table 1 summarizes the antiproliferative effects of 1-(3',4',5'-trimethoxybenzoyl)-3-anilino-5-amino 1,2,4-triazoles **3a-n** against a panel of seven human cancer cell line, using CA-4 (**1**) as the reference compound. The 1-(3',4',5'-trimethoxybenzoyl)-3-amino-5-anilino 1,2,4-triazole isomers **7a-c**, **7g-h** and **7k-l** were also evaluated for their activities, but, since they were all inactive (IC_{50}>10 μM), the data are not shown in Table 1.

Three of the synthesized compounds, corresponding to the *p*-Me, *m,p*-di-Me and *p*-Et phenyl analogues **3c**, **3e** and **3f**, respectively, were significantly more active than the rest of derivatives, with IC_{50} values of 0.21-3.2, 0.4-4.0, and 0.21-6.0 nM, respectively, in the seven cell lines, as compared with 4-3100 nM for CA-4.

With average IC_{50} values of 1.0, 1.9 and 2.4 nM for **3c**, **3e** and **3f**, respectively, **3c** appears to be the most active compound in the series (for CA-4, the average value was 525 nM or, excluding the HT-29 cell line from the average, 96 nM). Thus, these three compounds are substantially more active than CA-4, and they are also more potent than their previously described isosteres **2a** and **2b**.

In addition to these highly potent three derivatives, the *m*-OMe and *m,p*-methylenedioxy phenyl derivatives **3j** and **3n**, respectively, were more active than CA-4 against HT-29, A549 and MCF-7 cells.

In short, the data shown in Table 1 indicate the importance of substituents and their relative position on the phenyl ring of the arylamino moiety at the C-3 position of the 1,2,4-triazole skeleton for activity and selectivity against different cancer cell lines.

Table 1. *In vitro* cell growth inhibitory effects of compounds **3a-n** and CA-4 (**1**)

Compd	IC_{50} [a](nM)						
	Jurkat	CCRF-CEM	SEM	HeLa	HT-29	A549	MCF-7
3a	1200±270	1000±90	1200±190	>10,000	6200±1200	>10,000	500±240
3b	1900±400	2200±400	2400±210	410±70	2000±700	3800±160	370±30
3c	0.81±0.03	0.21±0.04	0.51±0.10	3.2±1.3	0.82±0.10	0.51±0.22	1.0±0.61
3d	42±16	330±60	30±10	440±50	460±80	870±30	15±3.2
3e	2.0±0.11	0.81±0.10	0.40±0.11	2.0±0.82	3.0±0.91	1.0±0.82	4.0±0.21
3f	1.0±0.09	3.0±0.09	0.81±0.21	6.0±1.0	0.21±0.08	0.92±0.51	5.0±1.0
3g	520±40	1800±90	500±10	130±28	800±100	550±70	510±70
3h	>10,000	>10,000	>10,000	>10,000	>10,000	>10,000	5200±110
3i	51±10	1000±200	44±16	120±30	480±15	2400±100	260±80
3j	7.2±2.0	120±30	1.0±0.4	30±1.2	700±32	54±4.3	11±4.2
3k	>10,000	9000±330	>10,000	>10,000	>10,000	>10,000	>10,000
3l	>10,000	>10,000	>10,000	>10,000	>10,000	>10,000	>10,000
3m	2500±220	2000±100	1900±170	2100±800	3700±400	6200±540	34±18
3n	24±7.2	40±3.3	30±6	930±54	60±10	150±50	19±5.2
CA-4	5±0.6	12±2.5	5±0.1	4±0.1	3100±100	180±50	370±100

[a]IC_{50}= compound concentration required to inhibit tumor cell proliferation by 50%. Data are expressed as the mean ± SE from the dose-response curves of at least three independent experiments carried out in triplicat

The unsubstituted anilino derivative **3a** was weakly active (IC_{50}>0.5 μM), and the introduction of a weak electron-releasing fluorine atom at the *para*-position of the phenyl (compound **3b**) had the opposite effect, with slightly improved antiproliferative activity with respect to **3a** against HeLa, HT-29, A549 and MCF-7 cells, while the activity was reduced against Jurkat, CCRF-CEM and SEM cells.

We found that the small methyl group at the *para*-position of the phenyl ring, to furnish derivative **3c**, improved significantly antiproliferative activity relative to **3a**.

Moving the methyl group from the *para*- to the *meta*-position, to furnish isomer derivative **3d**, reduced antiproliferative activity from one to three orders of magnitude, with double digit nanomolar activity against Jurkat, SEM and MCF-7 cells. Since the *para*-toluidino moiety of **3c** was favorable for potency, it is important to point out that the introduction of an additional methyl group at the *meta*-position, resulting in the *meta*, *para*-dimethyl derivative **3e**, produced a 2- to 4-fold reduction in antiproliferative activity against five of the six cancer cell lines, while **3c** and **3e** were equipotent against SEM and HeLa cells.

The *para*-ethyl homologue **3f** was 2-15-fold less active than methyl counterpart **3c** against four of the seven cancer cell lines, with a minimal difference between the two compounds in the Jurkat and SEM cells, while **3f** was 4-fold more potent than **3c** against HT-29 cells. Replacing the *para*-ethyl group with branched (*i*-Pr) or larger (*n*-butyl) moieties (compounds **3g** and **3h**, respectively) was detrimental for activity in all cell lines, suggesting that an increase in steric bulk at this position caused a decrease in potency.

The number and position of methoxy substituents on the phenyl ring (compounds **3i-l**) had a major influence on antiproliferative activity. Replacement of the methyl moiety with a more electron-releasing methoxy group at the *para*-position of the phenyl ring (compound **3i**) decreased antiproliferative activity by 100-fold compared with **3c**, indicating that the methyl and methoxy groups are not bioequivalent at the *para*-position of the phenyl ring.

The contribution of methyl or methoxy groups on the phenyl ring to activity (**3c** *vs.* **3d** and **3i** *vs.* **3j**, respectively) was position dependent, with opposite effects. While for the methyl group, as previously observed, the *para*-derivative **3c** was considerably more potent than *meta*-isomer **3d**, an opposite effect was observed for the two methoxy isomers **3i** and **3j**, with the *meta*-isomer **3j** from 4- to 44-fold more potent than the *para*-isomer **3i** in six of the seven cancer cell lines, the exception being the HT-29 cells.

Either two or three methoxy substituents (derivatives **3k** and **3l**, respectively) caused substantial loss in antiproliferative activity relative to **3i** and **3j**, suggesting that steric factors account for the loss of activity observed with these two compounds.

With the exception of the MCF-7 cells, the *para*-ethoxy derivative **3m** was 2- to 50-fold less potent than its methoxy counterpart **3m**. The 3',4'-methylenedioxy derivative **3n**, with IC_{50} values in the double-digit nanomolar range in five of the seven cancer cell lines, showed an antiproliferative activity intermediate between those of *para*- and *meta*-methoxy analogues **3i** and **3j**, respectively.

Evaluation of cytotoxicity in human non-cancer cells. To obtain a preliminary indication of the cytotoxic potential of these derivatives for normal human cells, two of the most active compounds (**3c** and **3f**) were assayed *in vitro* against peripheral blood lymphocytes (PBL) from healthy donors (Table 2). Both compounds were practically ineffective in quiescent lymphocytes, with an IC_{50} of about 30 μM. In the presence of the mitogenic stimulus phytohematoagglutinin (PHA), the IC_{50} decreased to about 8 μM for both compounds, a value that is thousands of times higher than those observed against the lymphoblastic cell lines Jurkat and CCRF-CEM.

Furthermore, compound **3c** was also evaluated in human umbilical vein endothelial cells (HUVECs), and again the IC_{50} value was negligible compared with those found in the panel of cancer cell lines. Altogether these data suggest that these compounds may have cancer cell selective antiproliferative properties.

Table 2. Cytotoxicity of **3c** and **3f** in human non-cancer cells

Cell line	IC_{50} (μM) [a]	
	3c	**3f**
$PBL_{resting}$ [b]	31.2±8.7	34.0±11.7
PBL_{PHA} [c]	8.5±2.6	8.8±2.7
HUVEC	11.9±3.8	n.d.

[a] Compound concentration required to reduce cell growth inhibition by 50%.

[b] PBL not stimulated with PHA.

[c] PBL stimulated with PHA.

Values are the mean ± SEM for three separate experiments. n.d

Effect of compound 3c on drug-resistant cell lines

Drug resistance has become a serious problem in cancer chemotherapy [128,129]. One of the common mechanisms of resistance so far identified both in preclinical and clinical studies involves the overexpression of a cellular membrane protein called P-glycoprotein (P-gp) that mediates the efflux of various structurally unrelated drugs [128,129].

We evaluated sensitivity of compound **3c** in two multidrug-resistant cell lines, one derived from a colon carcinoma ($Lovo^{Doxo}$) [130], the other derived from a lymphoblastic leukemia ($CEM^{Vbl\text{-}100}$) [131]. Both these lines express high levels of the P-gp [130,131].

As shown in Table 3, compound **3c** was almost equally potent toward cells resistant to doxorubicin or vinblastine showing a resistance index (RI), which is the ratio between GI_{50} values of resistant cells and sensitive cells, of 1.2 and 5.7 respectively, while doxorubicin in $LoVo^{Doxo}$ and vinblastine in CEM^{Vbl100} showed a high RI of 118 and 193, respectively.

Altogether these results suggest that this compound might be useful in the treatment of drug refractory tumors

Table 3. In vitro cell growth inhibitory effects of compounds 3c on drug resistant cell lines

Compd	IC_{50} [a](nM)		
	LoVo	**LoVo^{Doxo}**	**Resistance ratio[b]**
3c	0.9±0.1	1.1± 0.5	1.2
Doxorubicin	95.6 ± 43.2	11296 ± 356	118
	CEM	**CEM ^{Vbl100}**	**Resistance ratio[b]**
3c	0.21 ± 0.4	1.2± 0.5	5.7
Vinblastine	1.0 ± 0.3	193 ± 39	193

[a]IC_{50}=compound concentration required to inhibit tumor cell proliferation by 50%. Data are presented as the mean ± SE from the dose-response curves of two independent experiments performed in triplicate.

[b]The values express the ratio between IC_{50} determined in resistant and non-resistant cell lines.

Inhibition of tubulin polymerization and colchicine binding. A subset of the compounds (**3c-g**, **3i-j** and **3n**) were evaluated for their *in vitro* inhibition of tubulin polymerization in comparison with CA-4. The same compounds were also examined for inhibitory effects on the binding of [^{3}H]colchicine to tubulin (Table 4).

In the assembly assay, with 10 μM tubulin, compound **3c** was highly potent, yielding an IC_{50} of 0.75 μM, almost twice as active as CA-4. Derivatives **3e** and **3f** had IC_{50} values of 1.2 and 1.4 μM, comparable to the value obtained with CA-4. Compounds **3d**, **3i-j** and **3n** were less active as inhibitors of tubulin polymerization, with IC_{50} values of 1.8, 3.7, 2.5 and 2.0 μM, respectively, while **3g** was, relatively speaking, almost inactive.

The order of inhibitory effects on tubulin assembly was **3c**>**3e**=CA-4>**3f**>**3d**>**3n**>**3j**>**3i**>>**3g**. This order of activity as inhibitors of tubulin assembly correlates well with their order of activity as antiproliferative agents against Jurkat, CCRF-CEM, SEM and HeLa cells.

In the competition assay, compound **3c** was again the most active derivative, inhibiting colchicine binding by 92%, versus 98% for CA-4. In the experiments summarized in Table 4, the concentration of tubulin was 1.0 μM, while that of both the inhibitors and [^{3}H]colchicine was 5.0 μM.

Inhibition of colchicine binding by compounds **3e** and **3f** was lower, with 83% and 80% inhibition occurring with these agents. With the exception of compounds **3j** and **3n**, a good correlation was observed between antiproliferative activities, inhibition tubulin polymerization and inhibition of colchicine binding.

Table 4. Inhibition of tubulin polymerization and colchicine binding by compounds 1a, 3c-g, 3i-j and 3n.

Compound	Tubulin assembly[a] IC_{50}±SD (μM)	Colchicine binding [b] % ±SD
3c	0.75±0.1	92±2
3d	1.8±0.0	67±1
3e	1.2±0.0	83±1
3f	1.4±0.0	80±2
3g	13±0.7	n.d
3i	3.7±0.4	48±2
3j	2.5±0.0	70±0.9
3n	2.0±0.0	51±0.3
1a	1.2±0.1	98±0.5

[a] Inhibition of tubulin polymerization. Tubulin was at 10 μM.

[b] Inhibition of [^{3}H]colchicine binding. Tubulin, colchicine and tested compound were at 1, 5 and 5 μM, respectively.

n.d: not determined

To further investigate if the new derivatives interfered with the microtubule network, we examined the effects of **3c** on HeLa cells by immunofluorescence microscopy.

Following a 24 h treatment with **3c** at 50, 100 and 250 nM, the microtubule network was substantially modified in comparison with the untreated cells.

Altogether these results are consistent with the conclusion that the antiproliferative activity of these compounds derived from an interaction with the colchicine site of tubulin, and this ultimately results in interference with microtubule assembly.

4.3 Molecular Modeling. To rationalize the experimental data observed for **3a-n**, we performed a series of molecular docking simulations of these compounds in the colchicine site of tubulin. The proposed binding mode for **3c** is very similar to the one presented by the co-crystallized DAMA-colchicine (Figure 2, panel A).

In particular, it is possible to observe how the trimethoxyphenyl ring is in proximity of Cys241, while the phenyl ring occupies a hydrophobic region deep in the binding site, establishing a series of interactions with Met259, Thr314 and Lys352. Indeed, this sub-pocket is relatively small and, while the methyl substituent on the phenyl ring of **3c** is able to fit in properly, larger groups, such as the isopropyl (**3g**) or the *n*-butyl (**3h**), cannot be accommodated into it. In these cases, the docking simulations are not able to generate a reasonable binding pose.

The docking results are in accordance with the experimental data, and they provide a possible structural justification of the SARs observed (Figure 2, panel B). Finally, it is interesting to note that the **3c** binding conformation generated in the docking simulation is very similar to the conformation of the structure obtained experimentally by X-ray crystallography (Figure 2, panel C).

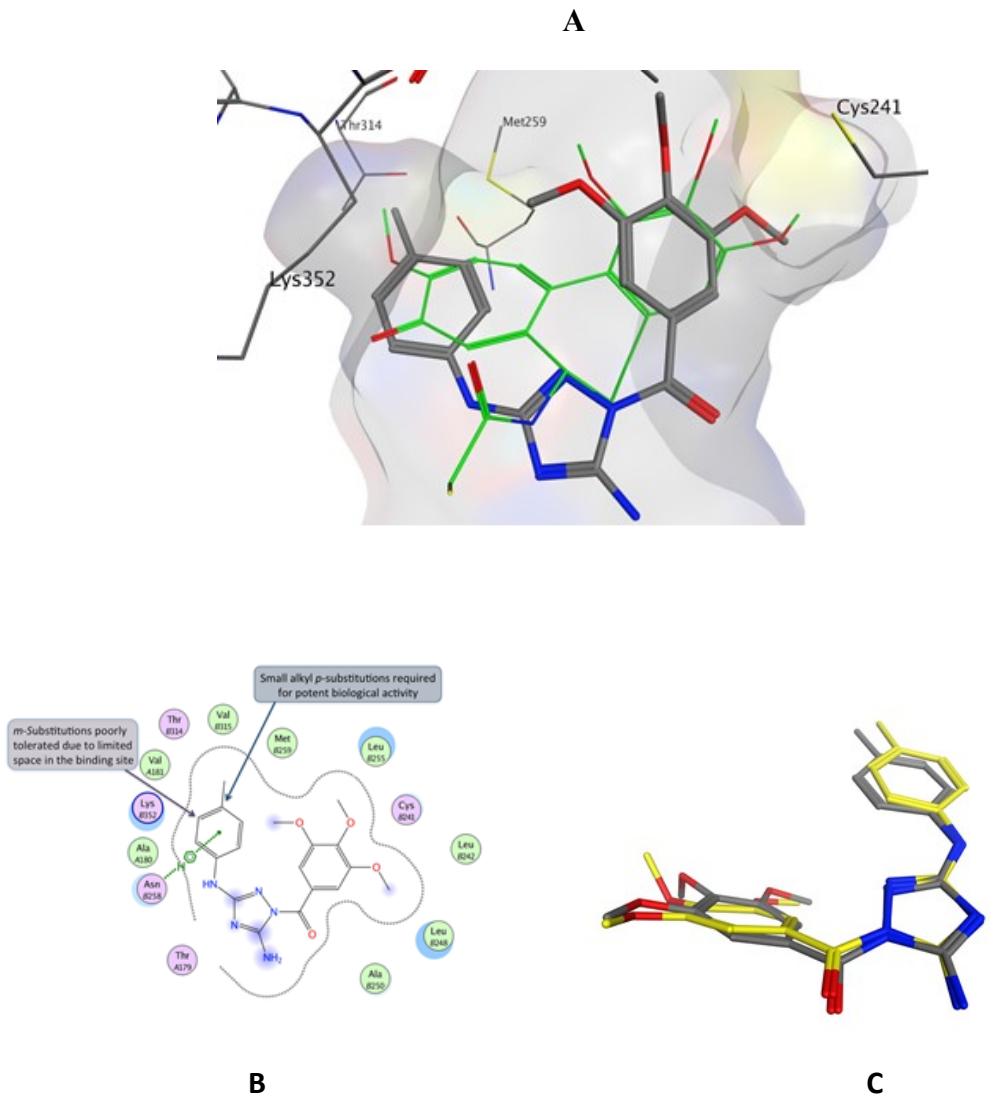

Figure 2. Panel A. Proposed binding for 3c (in grey) in the colchicine site. Co-Crystallized DAMA-colchicine is shown in green. Panel B. Representation of the binding mode of 3c in the colchicine site, with a summary of the SARs observed for the reported series of compounds. Panel C. Superposition of the conformation obtained from the docking simulations (in grey) and the crystal structure (in yellow) of 3c

4.4 Analysis of 3-arylamino 1,2,4-triazole derivatives for effects on the cell cycle. The effects of a 24 h treatment with different concentrations of **3c** on cell cycle progression in HeLa and Jurkat cells were determined by flow cytometry (Figure 3, panels A, B).

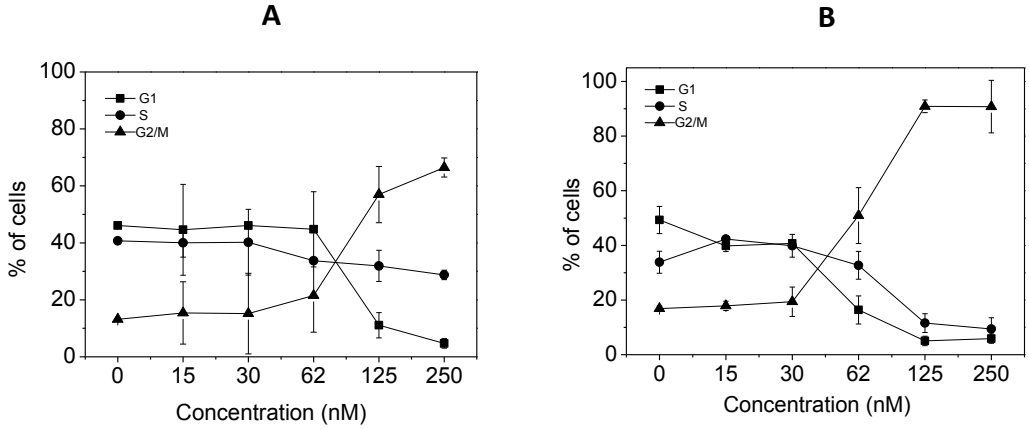

Figure 3. Percentage of cells in each phase of the cell cycle in HeLa (Panel A) and Jurkat cells (Panel B) treated with **3c** at the indicated concentrations for 24 h. Cells were fixed and labeled with PI and analyzed by flow cytometry as described in the experimental section. Data are represented as mean ± SEM of three independent experiments

The compound caused a significant G2/M arrest in a concentration-dependent manner in the cell lines tested, with a rise in G2/M cells occurring at a concentration as low as 60 nM, while, at higher concentrations, more than 70% of the cells were arrested in G2/M. The cell cycle arrest in the G2/M phase was accompanied by a corresponding reduction in cells in the other phases of the cell cycle. In particular, the G1 phase decreased in both cell lines whereas S phase reduction was mainly evident in Jurkat cells.

We next studied the association between **3c**-induced G2/M arrest and alterations in expression of proteins that regulate cell division.

As shown in Figure 4 in HeLa cells, a 24 h treatment with **3c** at concentrations lower than 100 nM caused no significant variation in cyclin B expression, which, in association with cdc2 controls both entry into and exit from mitosis [132,133], while at 100 and 250 nM we observed a clear increase in the cyclin B1 band.

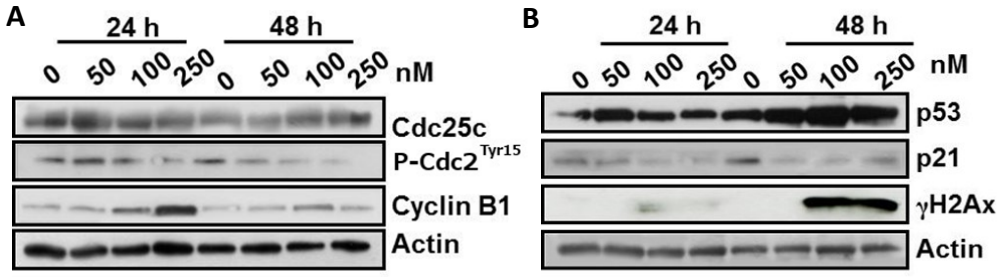

Figure 4. Effects of **3c** on G2/M regulatory proteins (Panel A) and on p53, p21 and γH2AX expression (panel B). HeLa cells were treated for 24 or 48 h with the indicated concentration of **3c**. The cells were harvested and lysed for the detection of cyclin B1, p-cdc2^{Tyr15} and cdc25C (panel A) or p53, p21 and γH2AX expression (panel B) by western blot analysis. To confirm equal protein loading, each membrane was stripped and reprobed with anti-β-actin antibody

After a 48 h treatment, cyclin B1 expression decreased. More importantly, p-cdc2^{Tyr15} expression decreased after either 24 or 48 h of treatment. However, no major changes in the expression of phosphatase cdc25c were observed.

These results indicate that arrest at G2/M induced by **3c** is caused by an immediate block of cyclin B1 activity, followed by its accumulation, leading to a persistent and marked decrease of p-cdc2 ^{Tyr15} more detectable at the highest concentrations (100-250 nM) examined.

In addition to the analysis of proteins that control cell cycle checkpoints, we also examined the expression of the tumor suppressor p53 after treatment of Hela cells with **3c**. It is well known that prolonged mitotic arrest induces DNA damage and, consequently, p53 up-regulation [134,135].

As shown in Figure 4 (panel B), we detected in a concentration-dependent manner an increase in p53 expression that is particularly evident after 48 h of treatment. At the same time, we also observed a marked increase in the expression of phosphorylated histone γH2A.X, which is an early sensitive indicator of DNA damage [136].

Interestingly, the expression of the cyclin-dependent kinase inhibitor p21, which was previously demonstrated to have an anti-apoptotic role [137], decreased both after 24 and 48 h of treatment

Compound 3c induces apoptosis. To characterize the mode of cell death induced by **3c,** a biparametric cytofluorimetric analysis was performed using propidium iodide (PI), which stains DNA and enters only dead cells, and fluorescent immunolabeling of the protein annexin-V, which binds to phosphatidylserine (PS) in a highly selective manner [138].

Dual staining for annexin-V and with PI permits discrimination between live cells (annexin-V$^-$/PI$^-$), early apoptotic cells (annexin-V$^+$/PI$^-$), late apoptotic cells (annexin-V$^+$/PI$^+$) and necrotic cells (annexin-V$^-$/PI$^+$). As shown in Figure 5, both HeLa (panel A) and Jurkat cells (panel B) treated with the two compounds for 24 h showed an accumulation of annexin-V positive cells that further increased after 48 h in comparison with the untreated cells. Analogous results were also obtained for compound **3e**

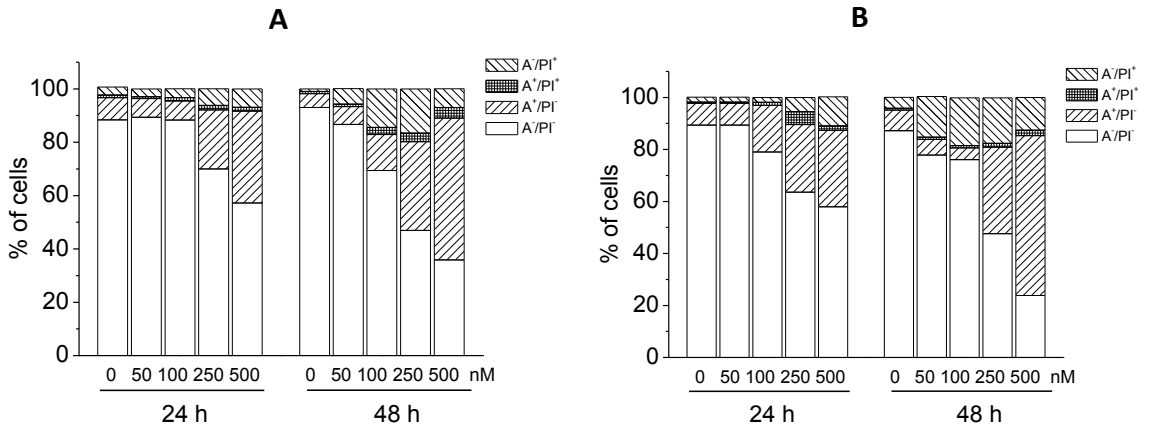

Figure 5. Flow cytometric analysis of apoptotic cells after treatment of HeLa cells (Panel A) or Jurkat cells (Panel B) with 3c at the indicated concentrations after incubation for 24 or 48 h. The cells were harvested and labeled with annexin-V-FITC and PI and analyzed by flow cytometry. Data are represented as mean ± SEM of three independent experiments

Compound 3c induces caspase-dependent apoptosis. We then analyzed by western blot which proteins are involved on the triggered apoptotic pathway upon treatment with **3c**. HeLa cells were treated with different concentrations of **3c** for 24 or 48 h (Figure 6).

Interestingly, **3c** induced activation of the initiator caspase-9 in a time and concentration-dependent manner. We observed also an activation of the effector caspase-3 and cleavage of its substrate PARP (Figure 6, panel A). Furthermore, the anti-apoptotic protein Bcl-2 was decreased by treatment with **3c** in a time dependent manner, while the expression of a pro-apoptotic protein, Bax was slightly increased only at 250 nM and at 48 h.

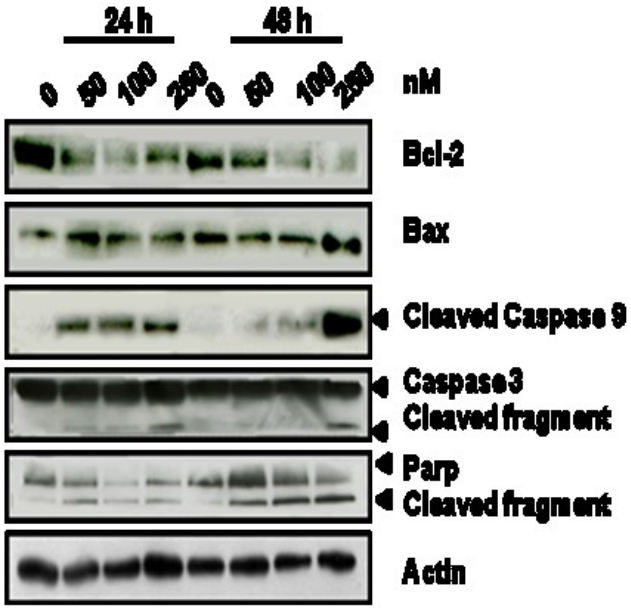

Figure 6. (A). Western blot analysis of caspase-3, cleaved caspase-9, PARP Bcl-2 and Bax after treatment of HeLa cells with 3c at the indicated concentrations and for the indicated times., To confirm equal protein loading, each membrane was stripped and reprobed with anti-β-actin antibody

4.5 Derivative 3c has antivascular effects *in vitro*. Tumor growth requires an oxygen supply, so the tumor microenvironment stimulates the development of additional blood vessels [139].

Recent antitumor strategies are based on the use of chemotherapeutics with anti-angiogenic or anti-vascular drugs, in order to increase the efficacy of the treatment [140]. Many tubulin binding agents show antivascular effects against tumor endothelium [141], including CA-4, and for that reason we evaluated **3c** for effects on endothelial cells *in vitro*.

We used human umbilical vein endothelial cells (HUVECs) as a model for angiogenesis/vasculogenesis processes *in vitro*. Endothelial cell migration to the tumor site is one of the described mechanisms of angiogenesis [142]. Inhibiting this mechanism could be a strategy to arrest the development of tumor vasculature.

We evaluated cell motility by scratching a HUVEC monolayer and monitoring the ability of cells to reclose the wound. As shown in Figure 7, (panel A), **3c** is very efficient in arresting cell motility. The effect is statistically significant after a 24 h incubation, at all the tested concentrations (5, 10, 25 nM), while, after 6 h, **3c** significantly inhibited cell motility at 10 and 25 nM, with a dose-response relationship observed (Figure 7, panel B).

To support the antivascular activity of **3c** we evaluated the ability of the compound to disrupt the "tubule-like" structures, formed by HUVECs seeded on Matrigel.

Matrigel is an extracellular matrix, rich in pro-angiogenic factors that stimulate single endothelial cells to assume an extended shape. The overall effect results in a reticulum similar to a capillary network.

As shown in Figure 7, panel C, after a 1 h incubation, 25 nM **3c** visibly disrupted the network of HUVECs, as compared with the control. After 3 h, all the tested concentrations were effective in altering the tubule-like structures.

An image analysis [143] was performed to obtain a quantitative measurement of the total length of the tubules, the area and the number of meshes, the percent of area covered by HUVECs, and the number of branching points (Figure 7, panel D) after a 3 h treatment.

The results indicate that the effects on endothelial cells induced by **3c** are similar to those observed after CA-4 treatment, in the same experimental conditions, carried out by our group [144].

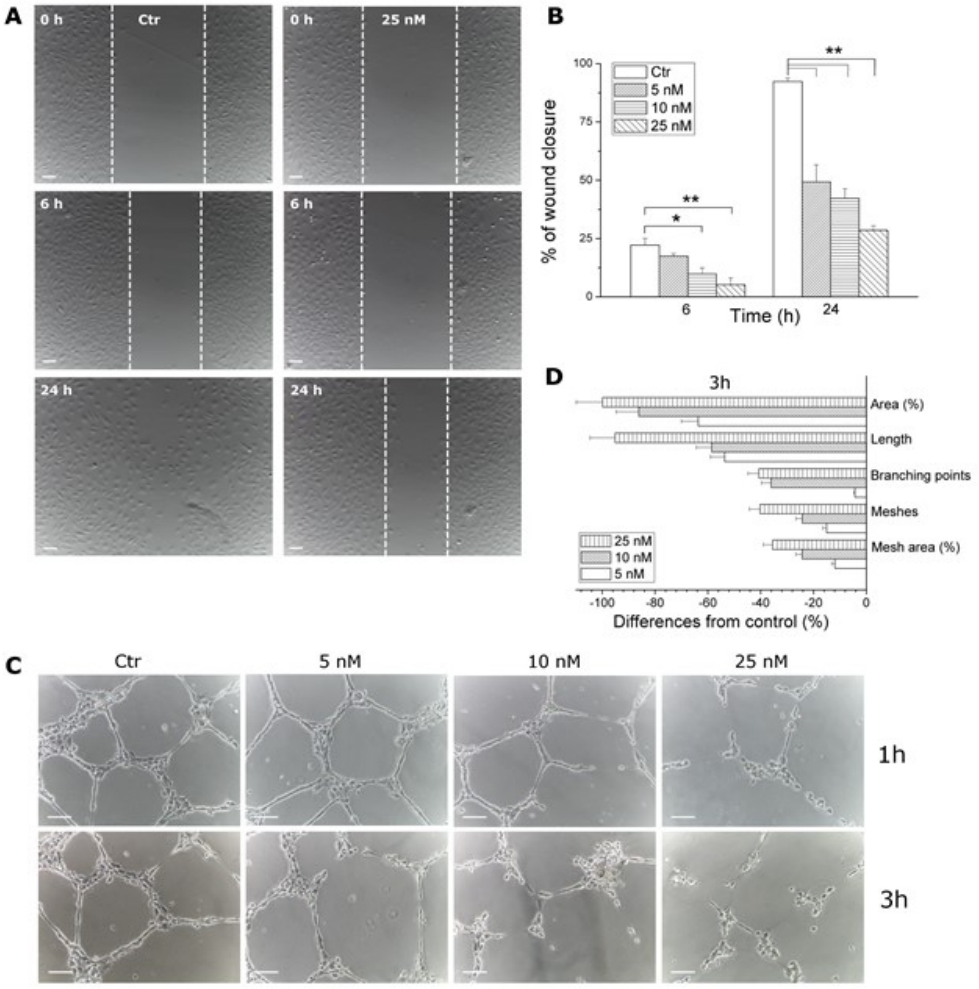

Figure 7. Compound 3c has antivascular activity *in vitro*. Panel A. Confluent HUVECs in a monolayer were wounded, and cells treated with different concentrations of 3c and at different times were photographed, 7x magnification; bar=100 μm. The dotted lines define the areas lacking cells. Panel B. The graph shows the quantitative effect of 3c. Migration was quantified by measuring the gap closure at the indicated times as shown in panel A. Data are represented as mean ± S.E.M. of three independent experiments. *p<0.05, **p<0.01 vs control. Panel C. Inhibition of endothelial cell capillary-like tubule formation by 3c. Tubule formation on Matrigel was carried out as described in the Experimental section. Representative pictures (10x magnification; bar=100 μm) of preformed capillary-like tubules treated with increasing concentrations of 3c for 1 or 3 h. Panel D. Quantitative analysis of the effects of 3c on the dimensional and topological parameters of the preformed capillary-like tubule networks, after a 3 h treatment. Data were represented as mean ± S.E.M. of three independent experiments. *p<0.05, **p<0.01 *vs*. control

4.6 Evaluation of antitumor activity of compound 3c *in vivo*. To evaluate the *in vivo* antitumor activity of **3c**, a syngeneic hepatocellular carcinoma model in mice was used [145]. Tumors were established by subcutaneous injection of BNL 1ME A.7R.1 cells into the backs of Balb/c mice. In preliminary experiments *in vitro,* we determined that both compound **3c** and CA-4, used as a reference compound, showed similar, potent cytotoxic activity (**3c** IC_{50}=3.4±1.1 nM; CA-4 IC_{50}=1.1±0.5 nM) against BNL 1ME A.7R.1 cells. Once the allografts reached a measurable size (about 100 mm^3), twenty mice were randomly assigned to one of four groups. In two of the groups, compound **3c** was injected intraperitoneally at doses of 5 and 10 mg/kg, respectively. In a third group, CA-4P was injected at 5 mg/kg, while the fourth group was used as a control.

As depicted in Figure 8 (panel A), compound **3c** caused a significant reduction in tumor growth, as compared with administration of vehicle, at 10 but not 5 mg/kg. The effect of 5 mg/kg of CA-4P was not as great as that of 10 mg/kg of **3c**, but the CA-4P effect was still significant relative to the control.

During the treatment period, only a small decrease in body weight occurred in the **3c**-treated animals (Figure 8, Panel B).

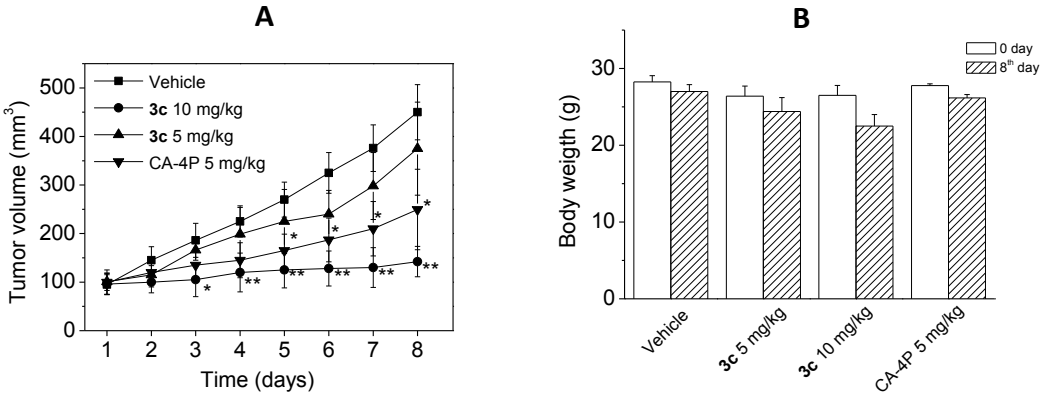

Figure 8. Inhibition of mouse allograft tumor growth *in vivo* by compound 3c. (A). Male mice were injected subcutaneously in their dorsal region with 10^7 BNL 1MEA.7R.1 cells, a syngeneic hepatocellular carcinoma cell line. Tumor-bearing mice were administered the vehicle, as control, or the indicated doses of 3c or CA-4P as reference compound at the concentration of 5 mg/kg. Daily injections were given intraperitoneally starting on day 1. The figure shows the average measured tumor volumes (A) and body weights of the mice (B) recorded at the beginning and at the end of the treatments. Data are presented as mean ± SEM of tumor volume and body weight at each time point for 5 animals per group. *p<0.05, **p<0.01 *vs*. control.

4.7 Conclusions

The bioisosteric equivalence between thiazole and 1,2,4-triazole prompted us to synthesize a series of 1-(3',4',5'-trimethoxybenzoyl)-3-arylamino-5-amino 1,2,4-triazole derivatives with general formula **3**, in which the 1,2,4-triazole ring replaced the thiazole system of previously published analogues with general structure **2**. The substitution pattern on the phenyl of the arylamino moiety had variable effects.

Compound **3c**, bearing a *p*-toluidino moiety at the C-3 position of 1,2,4-triazole ring, its *p*-ethyl homologue **3f** and the *m*,*p*-dimethyl analogue **3e** exhibited the greatest antiproliferative activity among the tested compounds, with IC_{50} values of 0.21-3.2, 0.21-6.0 and 0.4-4.0 nM, respectively. These results were superior or comparable with those of the reference compound CA-4 against all cancer cell lines. The *para*-position tolerates small substituents, such as methyl (**3c**) or ethyl (**3f**) groups, while the inactivity of *i*-Pr or *n*-Bu derivatives **3g** and **3h**, respectively, indicates that bulky substituents were detrimental for activity. Placing the methyl group in the *meta*-position (**3d**) led to a dramatic drop in potency as compared with the *para*-isomer **3c**, even though we observed excellent activity with the *meta*, *para*-dimethyl derivative **3e**. Compound **3c** was the most potent

inhibitor of tubulin polymerization and of colchicine binding (IC_{50}=0.75 μM for assembly, 92% inhibition of the binding of 5 μM colchicine), and the antiproliferative activity of **3c**, in terms of $IC_{50's}$, ranged from 0.21 to 3.2 nM in the seven cell tumor lines examined, values lower than that of previously published isosteric analogues [122].

In addition, in preliminary experiment **3c** had low toxicity in non tumoral cells and is active also in drug-resistant cell lines. Although **3c** was almost twice as active as CA-4 as an inhibitor of tubulin polymerization, these two compounds showed similar activity as inhibitors of colchicine binding. Moreover, in a detailed series of biological assays, we clearly demonstrated that **3c** induced caspase-dependent apoptosis and late DNA damage and p53 induction.

Compound **3c**, in addition to its ability to inhibit tubulin polymerization, efficiently targeted endothelial cells, acting as a VDA. More importantly, *in vivo* experiments showed that this compound was able to significantly reduce the growth of a syngeneic tumor model in mice, indicating that it is a very promising anticancer compound that warrants further evaluation for its potential clinical use.

4.7 Experimental Section

Chemistry. Materials and Methods. ^{1}H and ^{13}C NMR data were obtained with a Varian VXR 200 spectrometer and a Varian Mercury Plus 400 spectrometer, respectively. Peak positions are given in parts per million (δ) downfield, and *J* values are given in hertz. Positive-ion electrospray ionization (ESI) mass spectra were recorded on a double-focusing Finnigan MAT 95 instrument with BE geometry. Melting points (mp) were determined on a Buchi-Tottoli apparatus and are uncorrected. The purity of tested compounds was determined by combustion elemental analyses conducted by the Microanalytical Laboratory of the Chemistry Department of the University of Ferrara with a Yanagimoto MT-5 CHN recorder elemental analyzer. All tested compounds yielded data consistent with a purity of at least 95% as compared with the theoretical values. All reactions were carried out under an inert atmosphere of dry nitrogen, unless otherwise indicated. TLC was carried out using glass plates coated with silica gel 60 F_{254} by Merck, and compounds were visualized by UV detection or with aqueous $KMnO_4$. Flash column chromatography was performed using 230-400 mesh silica gel and the indicated solvent system. Organic solutions were dried over anhydrous Na_2SO_4. Solvents and reagents that are commercially available were purchased from Aldrich (Sigma-Aldrich) or Alfa Aesar (Johnson Matthey Company) and were used without further purification unless otherwise noted.

General procedure A for the synthesis of compounds 5a-n. To a solution of the appropriate aniline derivative (3 mmol, 1 equiv.) in isopropanol (10 mL) was added dimethyl cyanodithioimidocarbonate **4** (439 mg, 3 mmol), and the mixture was refluxed for 16 h. After this time, the solvent was removed under reduced pressure, the resulting residue was suspended in ethyl ether (10 mL) and filtered to furnish the final compound **5a-n** used for the next reaction without any purification.

(*Z*)-Methyl *N′*-cyano-*N*-phenylcarbamimidothioate (**5a**). Synthesized according to method **A**, derivative **5a** was obtained as a white solid (yield 71%); mp 192-193 °C. ^{1}H-NMR ($CDCl_3$) δ: 2.46 (s, 3H), 7.38 (m, 5H), 7.92 (bs, 1H). MS (ESI): $[M+1]^+$=192.3.

(*Z*)-Methyl *N′*-cyano-*N*-(4-fluorophenyl)carbamimidothioate (5b). Synthesized according to method **A**, compound **5b** was obtained as a grey solid (yield 78%); mp 216-218 °C. ^{1}H-NMR ($CDCl_3$) δ: 2.45 (s, 3H), 7.12 (t, *J*=8.0 Hz, 2H), 7.29 (m, 2H), 7.94 (bs, 1H). MS (ESI): $[M+1]^+$=210.3.

(*Z*)-Methyl *N′*-cyano-*N*-(*p*-tolyl)carbamimidothioate (5c). Synthesized according to method **A**, derivative **5c** was isolated as a white solid (yield 67%); mp 152-154 °C. ^{1}H-NMR ($CDCl_3$) δ: 2.38 (s, 3H), 2.43 (s, 3H), 7.14 (dd, *J*=9.0 and 2.6 Hz, 2H), 7.19 (dd, *J*=9.0 and 2.6 Hz, 2H), 7.97 (bs, 1H). MS (ESI): $[M+1]^+$=206.1.

(*Z*)-Methyl *N′*-cyano-*N*-(3-methylphenyl)carbamimidothioate (**5d**). Synthesized according to method **A**, derivative **5d** was obtained as a white solid (yield 52%); mp 148-150 °C. ^{1}H-NMR ($CDCl_3$) δ: 2.39 (s, 3H), 2.44 (s, 3H), 6.81 (m, 1H), 6.93 (s, 1H), 7.03 (m, 2H), 7.82 (bs, 1H). MS (ESI): $[M+1]^+$=206.2.

(*Z*)-Methyl *N′*-cyano-*N*-(3,4-dimethylphenyl)carbamimidothioate (**5e**). Synthesized according to method **A**, derivative **5e** was obtained as a white solid (yield 87%); mp 138-140 °C. ^{1}H-NMR ($CDCl_3$) δ: 2.27 (s, 6H), 2.43 (s, 3H), 7.05 (m, 2H), 7.14 (d, *J*=7.8 Hz, 1H), 7.84 (bs, 1H). MS (ESI): $[M+1]^+$=220.2.

(*Z*)-Methyl *N′*-cyano-*N*-(4-ethylphenyl)carbamimidothioate (**5f**). Synthesized according to method **A**, compound **5f** was obtained as a white solid (yield 68%); mp 159-161 °C. ^{1}H-NMR ($CDCl_3$) δ: 1.25 (t, *J*=7.6 Hz, 3H), 2.43 (s, 3H), 2.62 (q, *J*=7.6 Hz, 2H), 7.17 (dd, *J*=9.0 and 2.8 Hz, 2H), 7.24 (dd, *J*=9.0 and 2.8 Hz, 2H), 7.90 (bs, 1H). MS (ESI): $[M+1]^+$=220.4.

(*Z*)-Methyl *N′*-cyano-*N*-(4-isopropylphenyl)carbamimidothioate (5g). Synthesized according to method **A**, derivative **5g** was obtained as a white solid (yield 64%); mp 129-131 °C. ^{1}H-NMR ($CDCl_3$) δ: 1.26 (d, *J*=7.0 Hz, 6H), 2.44 (s, 3H), 2.93 (m, 1H), 6.89 (dd, *J*=8.4 and 2.4 Hz, 2H), 7.22 (dd, *J*=8.4 and 2.4 Hz, 2H), 7.93 (bs, 1H). MS (ESI): $[M+1]^+$=234.4.

(*Z*)-Methyl *N*-(4-*n*-butylphenyl)-*N′*-cyanocarbamimidothioate (**5h**). Synthesized according to method **A**, derivative **5h** was obtained as a white solid (yield 63%); mp 149-151 °C. ^{1}H-NMR ($CDCl_3$) δ: 0.93 (t, *J*=7.4 Hz, 3H), 1.33 (m, 2H), 1.59 (m, 2H), 2.43 (s, 3H), 2.63 (t, *J*=7.8 Hz, 2H), 7.17 (dd, *J*=8.8 and 2.4 Hz, 2H), 7.24 (dd, *J*=8.8 and 2.4 Hz, 2H), 7.93 (bs, 1H). MS (ESI): $[M+1]^+$=248.4.

(*Z*)-Methyl *N′*-cyano-*N*-(4-methoxyphenyl)carbamimidothioate (**5i**). Synthesized according to method **A**, compound **5i** was obtained as a purple solid (yield 91%); mp 193-195 °C. ^{1}H-NMR ($CDCl_3$) δ: 2.41 (s, 3H), 3.83 (s, 3H), 6.89 (d, *J*=8.8 Hz, 2H), 7.18 (d, *J*=8.8 Hz, 2H), 7.97 (bs, 1H). MS (ESI): $[M+1]^+$=222.1.

(*Z*)-Methyl *N′*-cyano-*N*-(3-methoxyphenyl)carbamimidothioate (**5j**). Synthesized according to method **A**, compound **5j** was obtained as a grey solid (yield 67%); mp 161-163 °C. ^{1}H-NMR (d_6-DMSO) δ: 2.69 (s, 3H), 3.75 (s, 3H), 6.82 (ddd, *J*=7.4, 2.4 and 1.2 Hz, 1H), 7.00 (m, 2H), 7.03 (m, 1H), 10.1 (bs, 1H). MS (ESI): $[M+1]^+$=222.1.

(*Z*)-Methyl *N′*-cyano-*N*-(3,4-dimethoxyphenyl)carbamimidothioate (5k). Synthesized according to method **A**, derivative **5k** was obtained as a purple solid (yield 69%); mp 178-180 °C. ^{1}H-NMR ($CDCl_3$) δ: 2.42 (s, 3H), 3.89 (s, 3H), 3.90 (s, 3H), 6.86 (m, 3H), 7.95 (bs, 1H). MS (ESI): $[M+1]^+$=252.3.

(*Z*)-Methyl *N′*-cyano-*N*-(3,4,5-trimethoxyphenyl)carbamimidothioate (**5l**). Synthesized according to method **A**, compound **5l** was obtained as a grey solid (yield 68%); mp 150-151 °C. ^{1}H-NMR ($CDCl_3$) δ: 2.45 (s, 3H), 3.81 (s, 3H), 3.86 (s, 6H), 6.54 (s, 2H), 7.96 (bs, 1H). MS (ESI): $[M+1]^+$=282.3.

(*Z*)-Methyl *N′*-cyano-*N*-(4-ethoxyphenyl)carbamimidothioate (**5m**). Synthesized according to method **A**, derivative **5m** was obtained as a grey solid (yield 82%); mp 165-167 °C. ^{1}H-NMR ($CDCl_3$) δ: 1.43 (t, *J*=7.2 Hz, 3H), 2.41 (s, 3H), 4.02 (q, *J*=7.2 Hz, 2H), 6.88 (dd, *J*=7.0 and 2.2 Hz, 2H), 7.17 (dd, *J*=7.0 and 2.2 Hz, 2H), 7.89 (bs, 1H). MS (ESI): $[M+1]^+$=236.2.

(*Z*)-Methyl *N*-benzo[*d*][1,3]dioxol-5-yl-*N′*-cyanocarbamimidothioate (**5n**). Synthesized according to method **A**, derivative **5n** was obtained as a white solid (yield 73%); mp 191-193 °C. ^{1}H-NMR ($CDCl_3$) δ: 2.42 (s, 3H), 6.04 (s, 2H), 6.79 (m, 3H), 7.81 (bs, 1H). MS (ESI): $[M+1]^+$=236.2.

General procedure B for the synthesis of compounds 6a-n. To a stirred suspension of derivative **5a-n** (2 mmol,) in dry THF (10 mL) was added hydrazine monohydrate (0.1 mL, 2 mmol, 1 equiv.), and the reaction mixture was heated under reflux for 6 h. After this time, the suspension was evaporated *in vacuo* to dryness, and the residue was suspended with ethyl ether (10 mL) and stirred for 10 min. The resultant solid was collected by filtration and then used for the next reaction without any purification.

***N*^{3}-Phenyl-1*H*-1,2,4-triazole-3,5-diamine** (**6a**). Synthesized according to general procedure **B**, derivative **6a** was obtained as a white solid (yield 74%); mp 160-161 °C. ^{1}H-NMR (d_6-DMSO) δ: 5.83 (bs, 2H), 6.71 (t, *J*=7.8 Hz, 1H), 7.14 (t, *J*=7.8 Hz, 2H), 7.46 (d, *J*=8.4 Hz, 2H), 8.57 (bs, 1H), 11.1 (bs, 1H). MS (ESI): $[M+1]^+$=176.1.

***N*^{3}-(4-Fluorophenyl)-1*H*-1,2,4-triazole-3,5-diamine (6b).** Synthesized according to general procedure **B**, derivative **6b** was obtained as a white solid (yield 83%); mp 216-218 °C. ^{1}H-NMR (d_6-DMSO) δ: 5.84 (bs, 2H), 6.98 (t, *J*=8.8 Hz, 2H), 7.48 (m, 2H), 8.61 (bs, 1H), 11.1 (bs, 1H). MS (ESI): $[M+1]^+$=194.2.

***N*^{3}-(*p*-Tolyl)-1*H*-1,2,4-triazole-3,5-diamine (6c).** Synthesized according to general procedure **B**, compound **6c** was obtained as a white solid (yield 92%); mp 185-187 °C. ^{1}H-NMR (d_6-DMSO) δ: 2.19 (s, 3H), 5.81 (bs, 2H), 6.93 (d, *J*=8.6 Hz, 2H), 7.36 (dd, *J*=8.6 Hz, 2H), 8.42 (bs, 1H), 11.0 (bs, 1H). MS (ESI): $[M+1]^+$=190.2.

***N*^{3}-(*m*-Tolyl)-1*H*-1,2,4-triazole-3,5-diamine** (**6d**). Synthesized according to general procedure **B**, compound **6d** was obtained as a white solid (yield >95%); mp 112-114 °C. ^{1}H-NMR (d_6-DMSO) δ: 2.21 (s, 3H), 5.81 (bs, 2H), 6.51 (d, *J*=7.2 Hz, 1H), 7.02 (t, *J*=7.2 Hz, 1H), 7.24 (d, *J*=7.2 Hz, 1H), 7.33 (s, 1H), 8.49 (bs, 1H), 11.1 (bs, 1H). MS (ESI): $[M+1]^+$=220.2.

***N*^{3}-(3,4-Dimethylphenyl)-1*H*-1,2,4-triazole-3,5-diamine** (**6e**). Synthesized according to general procedure **B**, derivative **6e** was obtained as a white solid (yield >95%); mp 180-182 °C. ^{1}H-NMR (d_6-DMSO) δ: 2.10 (s, 3H), 2.13 (s, 3H), 5.77 (bs, 2H), 6.86 (d, *J*=8.2 Hz, 1H), 7.18 (d, *J*=8.2 Hz, 1H), 7.26 (s, 1H), 8.35 (bs, 1H), 11.0 (bs, 1H). MS (ESI): $[M+1]^+$=204.3.

***N*^{3}-(4-Ethylphenyl)-1*H*-1,2,4-triazole-3,5-diamine (6f)**. Synthesized according to general procedure **B**, compound **6f** was obtained as a white solid (yield 92%); mp 187-189 °C. ^{1}H-NMR (d_6-DMSO) δ: 1.13 (t, *J*=7.6 Hz, 3H), 2.47 (q, *J*=7.6 Hz, 2H), 5.80 (bs, 2H), 6.96 (d, *J*=8.4 Hz, 2H), 7.37 (d, *J*=8.4 Hz, 2H), 8.42 (bs, 1H), 11.0 (bs, 1H). MS (ESI): $[M+1]^+$=204.3.

***N*^{3}-(4-Isopropylphenyl)-1*H*-1,2,4-triazole-3,5-diamine (6g).** Synthesized according to general procedure **B**, compound **6g** was obtained as a white solid (yield 60%); mp 156-158 °C. ^{1}H-NMR (d_6-DMSO) δ: 1.17 (d, *J*=6.8 Hz, 6H), 2.76 (m, 1H), 5.77 (bs, 2H), 6.99 (d, *J*=8.6 Hz, 2H), 7.37 (d, *J*=8.6 Hz, 2H), 8.44 (bs, 1H), 11.0 (bs, 1H). MS (ESI): $[M+1]^+$=218.2.

***N*^{3}-(4-*n*-Butylphenyl)-1*H*-1,2,4-triazole-3,5-diamine** (**6h**). Synthesized according to general procedure **B**, derivative **6h** was obtained as a white solid (yield 66%); mp 177-179 °C. ^{1}H-NMR (d_6-DMSO) δ: 0.88 (t, *J*=7.0 Hz, 3H), 1.26 (m, 2H), 1.48 (m, 2H), 2.41 (t, *J*=7.6 Hz, 2H), 5.80 (bs, 2H), 6.94 (d, *J*=8.2 Hz, 2H), 7.36 (dd, *J*=8.2 Hz, 2H), 8.43 (bs, 1H), 11.1 (bs, 1H). MS (ESI): $[M+1]^+$=232.3.

***N*^{3}-(4-Methoxyphenyl)-1*H*-1,2,4-triazole-3,5-diamine** (**6i**). Synthesized according to general procedure **B**, derivative **6i** was obtained as a grey solid (yield 88%); mp 200-201 °C. ^{1}H-NMR (d_6-DMSO) δ: 3.67 (s, 3H), 5.76 (bs, 2H), 6.74 (dd, *J*=7.0 and 2.2 Hz, 2H), 7.39 (dd, *J*=7.0 and 2.2 Hz, 2H), 8.32 (bs, 1H), 11.0 (bs, 1H). MS (ESI): $[M+1]^+$=206.3.

***N*^{3}-(3-Methoxyphenyl)-1*H*-1,2,4-triazole-3,5-diamine** (**6j**). Synthesized according to general procedure **B**, derivative **6j** was obtained as a red solid (yield >95%); mp 117-119 °C. ^{1}H-NMR (d_6-DMSO) δ: 3.76 (s, 3H), 5.78 (bs, 2H), 6.88 (dd, *J*=7.4 and 2.4 Hz, 1H), 7.02 (m, 2H), 7.05 (m, 1H), 8.47 (bs, 1H), 11.1 (bs, 1H). MS (ESI): $[M+1]^+$= 206.2.

***N*^{3}-(3,4-Dimethoxyphenyl)-1*H*-1,2,4-triazole-3,5-diamine** (**6k**). Synthesized according to general procedure **B**, derivative **6k** was obtained as a purple solid (yield 72%); mp 158-160 °C. ^{1}H-NMR (d_6-DMSO) δ: 3.66 (s, 3H), 3.75 (s, 3H), 5.75 (bs, 2H), 6.74 (d, *J*=8.8 Hz, 1H), 6.98 (m, 1H), 7.23 (d, *J*=2.4 Hz, 1H), 8.32 (bs, 1H), 11.2 (bs, 1H). MS (ESI): $[M+1]^+$=236.2.

***N*^{3}-(3,4,5-Trimethoxyphenyl)-1*H*-1,2,4-triazole-3,5-diamine** (**6l**). Synthesized according to general procedure **B**, derivative **6l** was obtained as a white solid (yield 68%); mp 241-243 °C. ^{1}H-NMR (d_6-DMSO) δ: 3.56 (s, 3H), 3.70 (s, 6H), 5.84 (bs, 2H), 6.90 (s, 2H), 8.43 (bs, 1H), 11.1 (bs, 1H). MS (ESI): $[M+1]^+$=266.3.

***N*^{3}-(4-Ethoxyphenyl)-1*H*-1,2,4-triazole-3,5-diamine** (**6m**). Synthesized according to general procedure **B**, derivative **6m** was obtained as a purple solid (yield 94%); mp 200-201 °C. ^{1}H-NMR (d_6-DMSO) δ: 1.28 (t, *J*=7.0 Hz, 3H), 3.93 (q, *J*=7.0 Hz, 2H), 5.76 (bs, 2H), 6.72 (dd, *J*=7.0 and 2.0 Hz, 2H), 7.38 (dd, *J*=7.0 and 2.0 Hz, 2H), 8.31 (bs, 1H), 11.0 (bs, 1H). MS (ESI): $[M+1]^+$=220.2.

***N*^{3}-(Benzo[d][1,3]dioxol-5-yl)-1*H*-1,2,4-triazole-3,5-diamine** (**6n**). Synthesized according to general procedure **B**, compound **6n** was obtained as a brown solid (yield 73%); mp 206-208 °C. ^{1}H-NMR (d_6-DMSO) δ: 5.80 (bs, 2H), 5.88 (s, 2H), 6.69 (d, *J*=8.2 Hz, 1H), 6.87 (dd, *J*=8.2 and 2.2 Hz, 1H), 7.26 (d, *J*=2.2 Hz, 1H), 8.45 (bs, 1H), 11.1 (bs, 1H). MS (ESI): $[M+1]^+$=220.2.

General procedure C for the synthesis of compounds 3a-n and 7a-n. To a stirred solution of the appropriate 1,2,4-triazole **6a-n** (1 mmol) in dry pyridine (10 mL) cooled at -5 °C was added 3',4',5'-trimethoxybenzoylchloride (230 mg, 1.1 mol, 1.1 equv.) in small portions. The reaction mixture was kept for 30 min at -5 °C and then overnight at room temperature. Pyridine was then removed by evaporation under reduced pressure. To the residue was added CH_2Cl_2, and the organic phase was washed with saturated aq. $NaHCO_3$, water and brine and dried over Na_2SO_4. The reaction mixture was filtered, and the solvent was removed *in vacuo*. The crude residue was purified by column chromatography on silica gel using a mixture of CH_2Cl_2-methanol (9.5:0.5) as eluent to separate the two regioisomeric 3',4',5'-trimethoxybenzoyl triazoles **3a-n** and **7a-n**, with the former compounds **3a-n** characterized by the lower R_f.

(3-(Phenylamino)-5-amino-1*H*-1,2,4-triazol-1-yl)(3,4,5-trimethoxyphenyl) methanone (**3a**). Synthesized according to method **C**, derivative **3a** was obtained as a yellow solid (yield 56%); mp 181-183 °C. ^{1}H-NMR (d_6-DMSO) δ: 3.79 (s, 3H), 3.86 (s, 6H), 6.86 (t, *J*=7.2 Hz, 1H), 7.22 (t, *J*=8.4 Hz, 2H), 7.56 (d, *J*=7.6 Hz, 2H), 7.68 (s, 2H), 7.93 (bs, 2H), 9.35 (s, 1H). ^{13}C-NMR (d_6-DMSO) δ: 55.96 (2C), 60.23, 108.66 (2C), 116.57 (2C), 120.37, 127.17, 128.57 (2C), 140.89, 141.37, 152.07 (2C), 157.58, 158.19, 165.37. MS (ESI): $[M]^+$=369.8.

(3-(4-Fluorophenylamino)-5-amino-1*H*-1,2,4-triazol-1-yl)(3,4,5-trimethoxyphenyl) methanone (**3b**). Synthesized according to method **C**, compound **3b** was obtained as a yellow solid (yield 60%); mp 218-220 °C. ^{1}H-NMR (d_6-DMSO) δ: 3.79 (s, 3H), 3.86 (s, 6H), 7.07 (t, *J*=8.8 Hz, 2H), 7.56 (dd, *J*=8.8 and 3.4 Hz, 2H), 7.61 (s, 2H), 7.83 (bs, 2H), 9.38 (s, 1H). ^{13}C-NMR (d_6-DMSO) δ: 55.98 (2C), 60.22, 108.58 (2C), 114.99, 115.21, 117.81, 117.88, 127.15, 137.40, 141.35, 152.08 (2C), 155.17, 157.60, 158.19, 165.41. MS (ESI): $[M]^+$=387.7.

(3-(4-Tolylamino)-5-amino-1*H*-1,2,4-triazol-1-yl)(3,4,5-trimethoxyphenyl) methanone (**3c**). Synthesized according to method **C**, compound **3c** was obtained as a yellow solid (yield 55%); mp 235-237 °C. ^{1}H-NMR (d_6-DMSO) δ: 2.22 (s, 3H), 3.79 (s, 3H), 3.88 (s, 6H), 6.97 (d, *J*=8.6 Hz, 2H), 7.44 (d, *J*=8.6 Hz, 2H), 7.68 (s, 2H), 7.81 (bs, 2H), 9.22 (s, 1H). ^{13}C-NMR (d_6-DMSO) δ: 20.26, 95.96 (2C), 60.22, 108.63 (2C), 116.68 (2C), 120.36, 127.20, 128.87 (2C), 138.41, 141.32, 152.15 (2C), 157.56, 158.26, 165.33. MS (ESI): $[M]^+$=383.5.

(3-(3-Tolylamino)-5-amino-1*H*-1,2,4-triazol-1-yl)(3,4,5-trimethoxyphenyl) methanone (**3d**). Synthesized according to method **C**, derivative **3d** was obtained as a yellow solid (yield 61%); mp 165-167 °C. ^{1}H-NMR (d_6-DMSO) δ: 2.30 (s, 3H), 3.78 (s, 3H), 3.85 (s, 6H), 6.65 (d, *J*=7.4 Hz, 1H), 7.08 (t, *J*=7.8 Hz, 1H), 7.34 (s, 1H), 7.39 (d, *J*=7.8 Hz, 1H), 7.61 (s, 2H), 7.80 (bs, 2H), 9.26 (s, 1H). ^{13}C-NMR (d_6-DMSO) δ: 21.26, 55.99 (2C), 60.22, 108.52 (2C), 113.77, 117.16, 120.98,

127.40, 128.38, 137.70, 140.87, 141.20, 152.05 (2C), 157.40, 158.14, 165.63. MS (ESI): $[M]^+$=383.5.

(3-(3,4-Dimethylphenylamino)-5-amino-1*H*-1,2,4-triazol-1-yl)(3,4,5-trimethoxyphenyl) methanone (3e). Synthesized according to method **C**, compound **3e** was obtained as a yellow solid (yield 48%); mp 169-171 °C. ^{1}H-NMR (d_6-DMSO) δ: 2.12 (s, 6H), 3.80 (s, 3H), 3.85 (s, 6H), 6.93 (d, *J*=8.0 Hz, 1H), 7.31 (s, 1H), 7.35 (d, *J*=8.0 Hz, 1H), 7.61 (s, 2H), 7.78 (bs, 2H), 9.14 (s, 1H). ^{13}C-NMR (d_6-DMSO) δ: 18.61, 19.75, 55.98 (2C), 60.22, 108.51 (2C), 114.01, 117.93, 127.45, 127.69, 129.42, 136.11, 138.74, 141.17, 152.03 (2C), 157.38, 158.21, 165.57. MS (ESI): $[M]^+$=397.7.

(3-(4-Ethylphenylamino)-5-amino-1*H*-1,2,4-triazol-1-yl)(3,4,5-trimethoxyphenyl) methanone (3f). Synthesized according to method **C**, compound **3f** was obtained as a yellow solid (yield 54%); mp 194-196 °C. ^{1}H-NMR (d_6-DMSO) δ: 1.14 (t, *J*=8.4 Hz, 3H), 3.51 (d, *J*=8.4 Hz, 2H), 3.78 (s, 3H), 3.97 (s, 6H). 7.02 (d, *J*=8.6 Hz, 2H), 7.46 (d, *J*=8.6 Hz, 2H), 7.68 (s, 2H), 7.81 (bs, 2H), 8.22 (s, 1H). ^{13}C-NMR (d_6-DMSO) δ: 16.35, 31.15, 56.41 (2C), 61.68, 109.07 (2C), 127.14 (2C), 127.66, 128.22 (2C), 135.97, 139.08, 141.76, 152.50 (2C), 156.03, 158.74, 165.78. MS (ESI): $[M]^+$=397.5.

(3-(4-Isopropylphenylamino)-5-amino-1*H*-1,2,4-triazol-1-yl)(3,4,5-trimethoxyphenyl) methanone (3g). Synthesized according to method **C**, derivative **3g** was obtained as a yellow solid (yield 52%); mp 197-199 °C. ^{1}H-NMR (d_6-DMSO) δ: 1.14 (d, *J*=6.8 Hz, 6H), 2.80 (m, 1H), 3.77 (s, 3H), 3.87 (s, 6H), 7.06 (d, J=8.2 Hz, 2H), 7.46 (d, *J*=8.2 Hz, 2H), 7.68 (s, 2H), 7.81 (bs, 2H), 9.21 (s, 1H). ^{13}C-NMR (d_6-DMSO) δ: 24.06 (2C), 32.65, 55.95 (2C), 60.23, 108.65 (2C), 116.75 (2C), 120.39 (2C), 124.28, 126.24, 138.70, 140.25, 152.05 (2C), 157.58, 158.32, 165.32. MS (ESI): $[M]^+$=411.7.

(3-(4-Butylphenylamino)-5-amino-1*H*-1,2,4-triazol-1-yl)(3,4,5-trimethoxyphenyl) methanone (3h). Synthesized according to method **C**, compound **3h** was obtained as a yellow solid (yield 54%); mp 134-136 °C. ^{1}H-NMR (d_6-DMSO) δ: 0.88 (t, *J*=7.2 Hz, 3H), 1.29 (m, 2H), 1.50 (m, 2H), 2.44 (t, *J*=7.6 Hz, 2H), 3.80 (s, 3H), 3.87 (s, 6H), 7.00 (d, J=8.6 Hz, 2H), 7.45 (d, J=8.6 Hz, 2H), 7.68 (s, 2H), 7.81 (bs, 2H), 9.22 (s, 1H). ^{13}C-NMR (d_6-DMSO) δ: 13.78, 21.66, 33.36, 34.09, 55.94 (2C), 60.23, 108.64 (2C), 116.67 (2C), 120.38, 127.21, 128.30 (2C), 134.05, 138.61, 152.05 (2C), 157.57, 158.29, 165.33. MS (ESI): $[M]^+$=425.8.

(3-(4-Methoxyphenylamino)-5-amino-1*H*-1,2,4-triazol-1-yl)(3,4,5-trimethoxyphenyl) methanone (3i). Synthesized according to method **C**, compound **3i** was obtained as a yellow solid (yield 64%); mp 196-197 °C. ^{1}H-NMR (d_6-DMSO) δ: 3.67 (s, 3H), 3.77 (s, 3H), 3.84 (s, 6H), 6.77 (d, *J*=8.8 Hz, 2H), 7.46 (d, *J*=8.8 Hz, 2H), 7.66 (s, 2H), 7.79 (bs, 2H), 9.11 (s, 1H). ^{13}C-NMR (d_6-DMSO) δ: 55.07, 55.85 (2C), 60.13, 108.53 (2C), 113.76 (2C), 127.81 (2C), 127.11, 134.24, 141.21, 151.95 (2C), 153.19, 157.48, 158.29, 165.16. MS (ESI): $[M]^+$=399.8.

(3-(3-Methoxyphenylamino)-5-amino-1*H*-1,2,4-triazol-1-yl)(3,4,5-trimethoxyphenyl) methanone (3j). Synthesized according to method **C**, compound **3j** was obtained as a yellow solid (yield 42%); mp 178-180 °C. ^{1}H-NMR (d_6-DMSO) δ: 3.65 (s, 3H), 3.78 (s, 3H), 3.86 (s, 6H), 6.44 (m, 1H), 7.12 (m, 2H), 7.26 (s, 1H), 7.61 (s, 2H), 7.81 (bs, 2H), 9.32 (s, 1H). ^{13}C-NMR (d_6-DMSO) δ: 54.76, 55.94 (2C), 60.19, 102.99, 105.19, 108.45 (2C), 109.37, 127.36, 129.29, 141.22, 142.01, 152.07 (2C), 157.45, 158.12, 159.78, 165.63. MS (ESI): $[M]^+$=399.6.

(3-(3,4-Dimethoxyphenylamino)-5-amino-1*H*-1,2,4-triazol-1-yl)(3,4,5-trimethoxyphenyl) methanone (3k). Synthesized according to method **C**, derivative **3k** was obtained as a yellow solid (yield 51%); mp 170-171 °C. ^{1}H-NMR (d_6-DMSO) δ: 3.67 (s, 3H), 3.73 (s, 3H), 3.77 (s, 3H), 3.83 (s, 6H), 6.77 (d, *J*=8.6 Hz, 1H), 7.08 (dd, *J*=8.6 and 2.2 Hz, 1H), 7.22 (d, *J*=2.2 Hz, 1H), 7.56 (s, 2H), 7.78 (bs, 2H), 9.09 (s, 1H). ^{13}C-NMR (d_6-DMSO) δ: 55.16 (2C), 56.00 (2C), 60.20, 102.58,

108.25, 108.33 (2C), 112.61, 127.61, 134.95, 141.06, 142.85, 148.90, 152.02 (2C), 157.35, 158.28, 165.71. MS (ESI): $[M]^+$=429.8.

(3-(3,4,5-Trimethoxyphenylamino)-5-amino-1*H*-1,2,4-triazol-1-yl)(3,4,5-trimethoxyphenyl) methanone (3l). Synthesized according to method **C**, derivative **3l** was obtained as a yellow solid (yield 48%); mp 172-174 °C. ^{1}H-NMR (d_6-DMSO) δ: 3.56 (s, 3H), 3.58 (s, 3H), 3.75 (s, 6H), 3.79 (s, 6H), 6.91 (s, 2H), 7.41 (s, 2H), 7.75 (bs, 2H), 9.16 (s, 1H). ^{13}C-NMR (d_6-DMSO) δ: 55.44 (2C), 56.08 (2C), 60.17 (2C), 94.92 (2C), 108.04 (2C), 128.01, 131.38, 137.16, 140.87, 151.98 (2C), 152.84 (2C), 157.09, 158.09, 166.29. MS (ESI): $[M]^+$=459.8.

(3-(4-Ethoxyphenylamino)-5-amino-1*H*-1,2,4-triazol-1-yl)(3,4,5-trimethoxyphenyl) methanone (**3m**). Synthesized according to method **C**, compound **3c** was obtained as a yellow solid (yield 54%); mp 176-178 °C. ^{1}H-NMR (d_6-DMSO) δ: 1.29 (t, J=6.8 Hz, 3H), 3.79 (s, 3H), 3.86 (s, 6H), 3.93 (q, *J*=6.8 Hz, 2H), 6.77 (d, *J*=9.0 H, 2H), 7.46 (d, *J*=9.0 H, 2H), 7.68 (s, 2H), 7.80 (bs, 2H), 9.11 (s, 1H). ^{13}C-NMR (d_6-DMSO) δ: 14.73, 55.95 (2C), 60.22, 63.09, 108.62 (2C), 114.44 (2C), 127.86 (2C), 127.22, 134.27, 141.29, 152.05 (2C), 152.51, 157.57, 158.38, 165.25. MS (ESI): $[M]^+$=413.8.

(5-Amino-3-(benzo[*d*][1,3]dioxol-5-ylamino)-1*H*-1,2,4-triazol-1-yl)(3,4,5-trimethoxyphenyl) methanone (3n). Synthesized according to method **C**, compound **3n** was obtained as a yellow solid (yield 46%); mp 200-201 °C. ^{1}H-NMR (d_6-DMSO) δ: 3.78 (s, 3H), 3.86 (s, 6H), 5.93 (s, 2H), 6.76 (d, *J*=8.4 Hz, 1H), 6.92 (dd, *J*=8.4 and 2.2 Hz, 1H), 7.33 (d, *J*=2.2 Hz, 1H), 7.65 (s, 2H), 7.81 (bs, 2H), 9.23 (s, 1H). ^{13}C-NMR (d_6-DMSO) δ: 55.97 (2C), 60.22, 99.01, 100.67, 108.12, 108.51 (2C), 108.93, 127.25, 135.73, 140.71, 141.28, 147.23, 152.06 (2C), 157.53, 158.26, 165.34. MS (ESI): $[M]^+$=413.8.

X-ray structure determination. X-ray diffraction data for compound **3c** were collected at room temperature, 295 K, on a Nonius Kappa CCD diffractometer with graphite monochromated Mo Kα radiation (λ = 0.7107 Å). The structure was solved by direct methods (SIR97) [146] and refined (SHELXL-97) [147] by full matrix least squares with anisotropic non-hydrogen atoms. The hydrogen atoms were included on calculated positions, riding on their carrier atoms, except for those bound to nitrogen. The latter were refined isotropically.

Crystal data: $C_{19}H_{21}N_5O_4$; orthorhombic, space group *Pbca*, *a* = 7.6945(1), *b* = 18.7364(4), *c* = 26.0711(5) Å, *V* = 3758.6(1) Å^3, *Z* = 8, Dc = 1.355 g cm^{-3}. Intensity data collected with θ ≤ 26°; 3677 independent reflections measured; 2412 observed [I >2σ(I)]. Final R index = 0.0471 (observed reflections), Rw = 0.1395 (all reflections), S = 1.022. Complete crystallographic data have been deposited with the Cambridge Crystallographic Data Centre as supplementary publication number CCDC N. 984800. Copies of that data can be obtained, free of charge, via www.ccdc.cam.ac.uk./conts/retrieving.html or on application to CCDC, 12 Union Road, Cambridge CB2 1EZ, U.K. [fax: +44(0)-1223-336033, e-mail: deposit@ccdc.cam.ac.uk].

Cell growth conditions and antiproliferative assay. Human T-leukemia (CCRF-CEM and Jurkat) and human B-leukemia (SEM) cells were grown in RPMI-1640 medium (Gibco, Milano, Italy). Breast adenocarcinoma (MCF-7), human cervix carcinoma (HeLa), and human colon adenocarcinoma (HT-29) cells were grown in DMEM medium (Gibco, Milano, Italy), all supplemented with 115 units/mL penicillin G (Gibco, Milano, Italy), 115 μg/mL streptomycin (Invitrogen, Milano, Italy), and 10% fetal bovine serum (Invitrogen, Milano, Italy). CEM$^{Vbl\text{-}100}$ cells are a multidrug-resistant line selected against vinblastine [131]. LoVo^{Doxo} cells are a doxorubicin resistant subclone of LoVo cells [132] and were grown in complete Ham's F12 medium supplemented with doxorubicin (0.1 μg/mL). LoVo^{Doxo} and CEM$^{Vbl\text{-}100}$ were a kind gift of Dr. G. Arancia (Istituto Superiore di Sanità, Rome, Italy). Stock solutions (10 mM) of the different compounds were obtained by dissolving them in DMSO. Individual wells of a 96-well tissue culture microtiter plate were inoculated with 100 μL of complete medium containing 8 × 10^3 cells. The plates were incubated at 37 °C in a humidified 5% CO_2 incubator for 18 h prior to the experiments. After medium removal, 100 μL of fresh medium containing the test compound at

different concentrations was added to each well in triplicate and incubated at 37 °C for 72 h. The percentage of DMSO in the medium never exceeded 0.25%. This was also the maximum DMSO concentration in all cell-based assays described below. Cell viability was assayed by the (3-(4, 5-dimethylthiazol-2-yl)-2,5-diphenyltetrazolium bromide test as previously described [148]. The IC_{50} was defined as the compound concentration required to inhibit cell proliferation by 50%, in comparison with cells treated with the maximum amount of DMSO (0.25%) and considered as 100% viability.

Peripheral blood lymphocytes (PBL) from healthy donors were obtained by separation on Lymphoprep (Fresenius KABI Norge AS) gradient. After extensive washing, cells were resuspended (1.0 x 10^6 cells/mL) in RPMI-1640 with 10% fetal bovine serum and incubated overnight. For cytotoxicity evaluations in proliferating PBL cultures, non-adherent cells were resuspended at 5 x 10^5 cells/mL in growth medium, containing 2.5 μg/mL PHA (Irvine Scientific). Different concentrations of the test compounds were added, and viability was determined 72 h later by the MTT test. For cytotoxicity evaluations in resting PBL cultures, non-adherent cells were resuspended (5 x 10^5 cells/mL) and treated for 72 h with the test compounds, as described above.

Effects on tubulin polymerization and on colchicine binding to tubulin. To evaluate the effect of the compounds on tubulin assembly *in vitro* [149a], varying concentrations of compounds were preincubated with 10 μM bovine brain tubulin in 0.8 M monosodium glutamate (pH adjusted to 6.6 with HCl in a 2.0 M stock solution) at 30 ˚C and then cooled to 0 ˚C. After addition of 0.4 mM GTP, the mixtures were transferred to 0 °C cuvettes in a recording spectrophotometer and warmed to 30 °C. Tubulin assembly was followed turbidimetrically at 350 nm. The IC_{50} was defined as the compound concentration that inhibited the extent of assembly by 50% after a 20 min incubation. The capacity of the test compounds to inhibit colchicine binding to tubulin was measured as described [149b], except that the reaction mixtures contained 1 μM tubulin, 5 μM [^{3}H]colchicine and 5 μM test compound.

Molecular modeling. All molecular modeling studies were performed on a MacPro dual 2.66GHz Xeon running Ubuntu 12.04. The tubulin structure was downloaded from the PDB data bank (http://www.rcsb.org/ - PDB code: 1SA0) [10]. Hydrogen atoms were added to the protein, using the Protonate 3D routine of the Molecular Operating Environment (MOE) [150]. Ligand structures were built with MOE and minimized using the MMFF94x forcefield until a RMSD gradient of 0.05 kcal mol^{-1} $Å^{-1}$ was reached. The docking simulations were performed using PLANTS [151].

Flow cytometric analysis of cell cycle distribution. 5×10^5 HeLa or Jurkat cells were treated with different concentrations of the test compounds for 24 h. After the incubation period, the cells were collected, centrifuged, and fixed with ice-cold ethanol (70%). The cells were then treated with lysis buffer containing RNase A and 0.1% Triton X-100 and then stained with PI. Samples were analyzed on a Cytomic FC500 flow cytometer (Beckman Coulter). DNA histograms were analyzed using MultiCycle for Windows (Phoenix Flow Systems).

Apoptosis assay. Cell death was determined by flow cytometry of cells double stained with annexin V/FITC and PI. The Coulter Cytomics FC500 (Beckman Coulter) was used to measure the surface exposure of PS on apoptotic cells according to the manufacturer's instructions (Annexin-V Fluos, Roche Diagnostics).

Western blot analysis. HeLa cells were incubated in the presence of **3c** and after different times were collected, centrifuged, and washed two times with ice cold phosphate buffered saline (PBS). The pellet was then resuspended in lysis buffer. After the cells were lysed on ice for 30 min, lysates were centrifuged at 15000 x g at 4 °C for 10 min. The protein concentration in the supernatant was determined using the BCA protein assay reagents (Pierce, Italy). Equal amounts of protein (10 μg) were resolved using sodium dodecyl sulfate-polyacrylamide gel electrophoresis (SDS-PAGE) (7.5−15% acrylamide gels) and transferred to PVDF Hybond-P membrane (GE Healthcare). Membranes were blocked with a bovine serum albumin (BSA) solution (BSA 5% in Tween PBS 1X), the membranes being gently rotated overnight at 4 °C. Membranes were then incubated with

primary antibodies against Bcl-2, Bax, PARP, cleaved caspase-9, cdc25c (Cell Signaling), caspase-3 (Alexis), H2AX (Cell Signaling), p53 (Cell Signaling), cyclin B (Cell Signaling), p-cdc2^{Tyr15} (Cell Signaling), p21 (Cell Signaling), or β-actin (Sigma-Aldrich) for 2 h at room temperature. Membranes were next incubated with peroxidase labeled secondary antibodies for 60 min. All membranes were visualized using ECL Select (GE Healthcare) and exposed to Hyperfilm MP (GE Healthcare). To ensure equal protein loading, each membrane was stripped and reprobed with anti-β-actin antibody.

Antivascular activity. HUVECs were prepared from human umbilical cord veins, as previously described [144]. The adherent cells were maintained in M200 medium supplemented with LSGS (Low Serum Growth Supplement), containing FBS, hydrocortisone, hEGF, bFGF, heparin, gentamycin/amphotericin (Life Technologies, Monza, Italy). Once confluent, the cells were detached by trypsin–EDTA solution and used in experiments from the first to sixth passages.

The motility assay for HUVECs was based on "scratch" wounding of a confluent monolayer [152]. Briefly, HUVECs ($1x10^5$) were seeded onto 0.1% collagen type I (BD Biosciences, Italy)-coated six well plates in complete medium until a confluent monolayer was formed. The cells were wounded using a pipette tip, and wells were washed with PBS to remove the detached cells. Then, the cells were treated with the test compounds, and at different times from the scratch, the cells were photographed under a light microscope. At all indicated time points, the wound width was measured in four areas and compared with the initial width.

Matrigel matrix (Basement Membrane Matrix, BD Biosciences, Italy) was kept at 4 °C for 3 h, when 230 µL of Matrigel solution was added to each well of a 24-well plate. After gelling at 37°C for 30 min, gels were overlaid with 500 µL of medium containing 6×10^4 HUVECs. The cells were incubated over Matrigel for 6 h to allow capillary tubes to form. Different concentrations of test compound were added in the cultures and incubated for different times, and the disappearance of existing vasculature was monitored and photographed (five fields for each well: the four quadrants and the center) at a 10x magnification. Phase contrast images were recorded using a digital camera and saved as TIFF files. Image analysis was carried out using the ImageJ image analysis software, and the following dimensional parameters (percent area covered by HUVECs and total length of HUVECs network per field) and topological parameters (number of meshes and branching points per fields) were estimated [143]. Values were expressed as percent change from control cultures grown with complete medium.

Antitumor activity *in vivo.* The *in vivo* cytotoxic activity of compound **3c** was investigated using a syngeneic murine hepatocellular carcinoma cell line (BNL 1ME A.7R.1) in Balb/c mice [145]. Male mice, 8 weeks old, were purchased from Harlan (S. Pietro al Natisone Udine, Italy), and tumors were induced by a subcutaneous injection in their dorsal region of 10^7 cells in 200 µL of sterile PBS. Animals were randomly divided into four groups, and, starting on the second day, the first group was daily dosed intraperitoneally (i.p.) with 7 µL/kg of free vehicle (0.9% NaCl containing 5% polyethylene glycol 400 and 0.5% Tween 80). Groups two and three were treated with compound **3c** at the doses of 5 and 10 mg/kg body weight, respectively. The fourth group received the reference compound CA-4P at the dose of 5 mg/kg body weight. Both compound **3c** and CA-4P were dissolved in free vehicle. Tumor sizes were measured daily for 7 days using a pair of calipers. In particular, the tumor volume (V) was calculated by the rotational ellipsoid formula: $V = A \times B2/2$, where A is the longer diameter (axial) and B is the shorter diameter (rotational). All experimental procedures followed guidelines recommended by the Institutional Animal Care and Use Committee of Padova University.

Statistical Analysis. Unless indicated otherwise, the results are presented as the mean ± SEM. The differences between different treatments were analyzed using the two-sided Student's t test. P values lower than 0.05 were considered significant.

5. Synthesis, in Vitro and in Vivo Anticancer and Antiangiogenic Activity of

Novel 3-Arylamino Benzofuran Derivatives Targeting the Colchicine Site on Tubulin

In our efforts to discover novel potent anticancer agents, inspired by the great antiproliferative activity of Combretastatin A-4 (CA-4, **1**, Chart 1), against a variety of cancer cells, including multidrug resistant cancer cell lines [153], and by the promising results in clinical trials showed by water-soluble disodium phosphate ester derivative of **1a** (named CA-4P, **1b**) [120], a new series of compounds characterized by the presence of a 2-methoxy/ethoxycarbonyl group, combined with either no substituent or a methoxy group at each of the four possible positions of the benzene portion of the 3-(3',4',5'-trimethoxyanilino)benzo[*b*]furan skeleton, were evaluated for antiproliferative activity against cancer cells in culture, and, for selected, highly active compounds, inhibition of tubulin polymerization, cell cycle effects and *in vivo* potency

Previous studies have yielded series of chemically diverse small molecules based on the benzo[*b*]furan scaffold, and the most active of these compounds act as antimitotic agents [154-156].

The 3-(3',4',5'-trimethoxybenzoyl)-6-methoxybenzo[*b*]furan molecular skeleton was the core structure of a series of antitubulin agents with general structure **2** identified by Pinney and co-workers as potent inhibitors of both tubulin polymerization and cell proliferation of the MCF-7 and MDA-MB-231 cancer cell lines [157-159]. While at the C-2 position there was a wide tolerance to structural variation with hydrophobic and hydrophilic substituents, at the C-3 position the carbon linker with the 3',4',5'-trimethoxyphenyl substituent was more effective as a carbonyl group than as a carbinol or a simple methylene group [157]. Previous studies have shown that the concomitant presence of a C-6 methoxy substituent significantly contributed to maximal activity, presumably as a mimic of the 4-methoxy group in the B-ring of CA-4 [158]. The introduction of a hydroxyl at the C-7 position was well tolerated and afforded compounds with similar potency for R_2=H, while a 10-fold increase in activity was observed for R_2=OH. Among the synthesized compounds, the C-2 methoxycarbonyl analogue **2a** showed potent activity in inhibiting the growth of the MDA-MB-231 human breast cancer cell line (IC_{50}: 1-10 nM). Moreover, **2a** had no significant selectivity against activated over quiescent human umbilical vein endothelial cells (HUVECs) (IC_{50}: 1-10 nM) [160].

These findings prompted us to analyze this class of compounds in more detail. Specifically, we were intrigued by the idea of studying the biological effects of replacing the carbonyl group at the C-3 position of compound **2a** by an anilinic nitrogen (NH) moiety with hydrogen-bond accepting and donating capability, to furnish a new series of 2-methoxy/ethoxycarbonyl-3-(3',4',5'-trimethoxyanilino)benzo[*b*]furan derivatives with general structure **3**.

By the synthesis of this series of compounds, we focused on the effects on antiproliferative activity obtained by the insertion of an electron-donating methoxy substituent at the C-4, C-5, C-6 or C-7 positions, combined with the methoxy/ethoxycarbonyl substitution at the C-2 position of the benzo[*b*]furan nucleus.

In this new class of compounds, the anilinic hydrogen at the C-3 position was also potentially able to generate an internal hydrogen bond with the sp_2-oxygen of the alkoxycarbonyl moiety.

Chart 1. Chemical structures of CA-4 (**1a**), CA-4P (**1b**), 2-substituted-3-(3,4,5-trimethoxybenzoyl)-6-methoxybenzo[*b*]furans **2**, 2-alkoxycarbonyl-3-(3,4,5-trimethoxyanilino)benzo[*b*]furan derivatives **3a-l**.

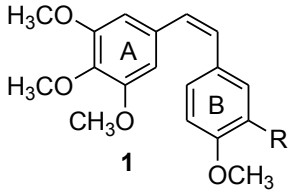

1

R=OH, Combretastatin A-4 (CA-4), **1a**
R=OPO_3Na_2, CA-4P, **1b**

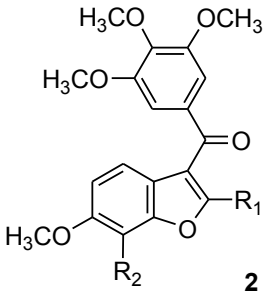

2

R_1=H, Br, CN, CO_2CH_3, alkyl, alkylamine, aryl, heteroaryl
R_2=H or OH
2a, R_1=CO_2CH_3, R_2=OH

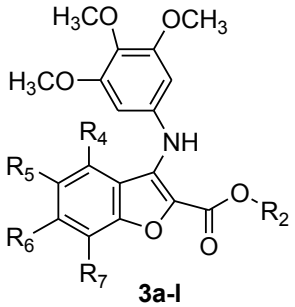

3a-l

3a, R_2=CH_3, R_{4-7}=H,
3b, R_5=C_2H_5, R_{4-7}=H,
3c, R_2=CH_3, R_4=OCH_3, R_{5-7}=H
3d, R_2=C_2H_5, R_4=OCH_3, R_{5-7}=H
3e, R_2=CH_3, R_5=OCH_3, $R_{4,6-7}$=H
3f, R_2=C_2H_5, R_5=OCH_3, $R_{4,6-7}$=H
3g, R_2=CH_3, R_6=OCH_3, $R_{4-5,7}$=H
3h, R_2=C_2H_5, R_6=OCH_3, $R_{4-5,7}$=H
3i, R_2=CH_3, R_7=OCH_3, R_{4-6}=H
3j, R_2=C_2H_5, R_7=OCH_3, R_{4-6}=H
3k, R_2=CH_3, R_7=OC_2H_5, R_{4-6}=H
3l, R_2=C_2H_5, R_7=OC_2H_5, R_{4-6}=H

5.1 Chemistry

Compounds **3a-l** were synthesized by a two-step procedure described in Scheme 1. The condensation of 2-hydroxy benzonitrile derivatives **4a-f** [156] with methyl or ethylbromoacetate and K_2CO_3 in DMF furnished by a tandem "one-pot" cyclization procedure the 2-methoxy/ethoxycarbonyl-3-amino benzo[*b*]furan derivatives **5a-l** in good yields. Finally, the novel derivatives **3a-l** were prepared using the C-N Buchwald-Hartwig palladium catalyzed cross-coupling protocol, by reaction of deactivated 3-amino benzo[*b*]furan analogues **5a-l** with 1-bromo-3,4,5-trimethoxybenzene, in the presence of $Pd(OAc)_2$, *rac*-BINAP and Cs_2CO_3 (as catalyst, ligand and base, respectively) in toluene at 100 °C.

Scheme 1

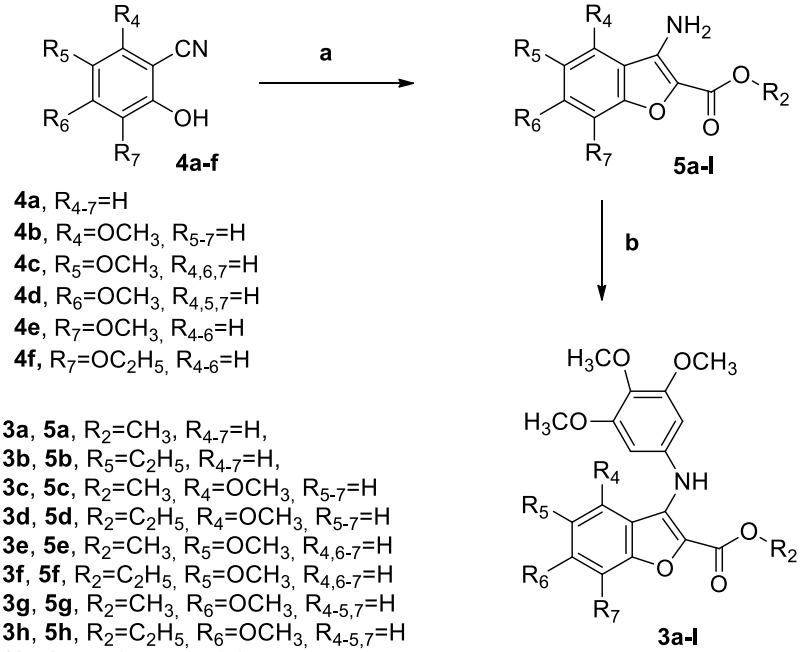

4a, R_{4-7}=H
4b, R_4=OCH_3, R_{5-7}=H
4c, R_5=OCH_3, $R_{4,6,7}$=H
4d, R_6=OCH_3, $R_{4,5,7}$=H
4e, R_7=OCH_3, R_{4-6}=H
4f, R_7=OC_2H_5, R_{4-6}=H

3a, **5a**, R_2=CH_3, R_{4-7}=H,
3b, **5b**, R_5=C_2H_5, R_{4-7}=H,
3c, **5c**, R_2=CH_3, R_4=OCH_3, R_{5-7}=H
3d, **5d**, R_2=C_2H_5, R_4=OCH_3, R_{5-7}=H
3e, **5e**, R_2=CH_3, R_5=OCH_3, $R_{4,6-7}$=H
3f, **5f**, R_2=C_2H_5, R_5=OCH_3, $R_{4,6-7}$=H
3g, **5g**, R_2=CH_3, R_6=OCH_3, $R_{4-5,7}$=H
3h, **5h**, R_2=C_2H_5, R_6=OCH_3, $R_{4-5,7}$=H
3i, **5i**, R_2=CH_3, R_7=OCH_3, R_{4-6}=H
3j, **5j**, R_2=C_2H_5, R_7=OCH_3, R_{4-6}=H
3k, **5k**, R_2=CH_3, R_7=OC_2H_5, R_{4-6}=H
3l, **5l**, R_2=C_2H_5, R_7=OC_2H_5, R_{4-6}=H

Reagents. a: $BrCH_2CO_2CH_3$ or $BrCH_2CO_2C_2H_5$, K_2CO_3, DMF, 60 °C for 4 h then reflux for 8 h: **b**: 1-Bromo-3,4,5-trimethoxybenzene, $Pd(OAc)_2$, BINAP, Cs_2CO_3, PhMe, 100 °C, 16 h.

5.2 Biological Results and Discussion

***In vitro* antiproliferative activities.** In Table 1 are summarized the *in vitr*o antiproliferative activities of 2-methoxy/ethoxycarbonyl-3-(3',4',5'-trimethoxyanilino)benzo[*b*]furan derivatives **3a-l** against a panel of seven human cancer cell lines, using **1a** as reference compound. The results presented in Table 1 indicate that inhibition of cell growth was highly dependent upon the presence and position of the methoxy substituent on the benzene portion of the benzo[*b*]furan system. In both series of 2-alkoxycabonyl derivatives, the greatest activity occurred when the methoxy group was located at the C-6 position (**3g** and **3h**), the least when it was located at the C-4 (IC_{50}>10 μM) position. In fact, the IC50's obtained in the 7 cell lines with the C-6 substituted compounds ranged from 0.3 to 27 (average, 7.8) nM with **3g** and from 13 to 100 (average, 34) nM with **3h**. The superiority of the methoxycarbonyl substituent over the ethoxycarbonyl substituent was observed in all of the cell lines except the MCF-7 cells, which were equally sensitive to both compounds.

Table 1. In vitro cell growth inhibitory effects of compounds **3a-l** and CA-4 (**1**)

Compd	IC_{50} [a] (nM)						
	HeLa	A549	HT-29	Jurkat	RS 4;11	MCF-7	HL-60
3a	260±50	5280±800	930±35	4100±200	430±97	7800±900	4400±200
3b	1330±580	5470±700	1600±120	180±38	300±80	6600±310	2500±130
3c	>10,000	>10,000	>10,000	>10,000	>10,000	>10,000	>10,000
3d	>10,000	>10,000	>10,000	>10,000	>10,000	>10,000	>10,000
3e	250±88	1570±430	240±60	210±20	39±9	7900±1300	470±30
3f	1260±510	8900±1460	1400±540	2300±700	190±15	2900±400	3400±120
3g	2±0.1	9±1.4	3±0.9	8±0.6	0.3±0.1	27±2	5±1
3h	13±8	36±11	17±8	22±6	100±10	25±3	24±7
3i	130±60	1270±400	290±30	30±5	1±0.1	520±40	320±17
3j	270±80	1100±300	110±50	290±50	230±10	2100±90	590±50
3k	2530±280	8900±1300	3200±210	3700±450	400±100	>10,000	4200±200
3l	3280±370	7250±237	5300±290	9100±820	3000±400	>10,000	5500±540
CA-4	4±1	180±30	3100±100	5±0.6	0.8±0.2	370±100	1±0.2

[a]IC_{50}= compound concentration required to inhibit tumor cell proliferation by 50%. Data are expressed as the mean ± SE from the dose-response curves of at least three independent experiments.

Overall, compounds **3i** (average IC_{50}, 370 nM) and **3j** (average IC_{50}, 670 nM), with the C-7 methoxy substituent, were more active than **3e** (average IC_{50}, 1,500 nM) and **3f** (average IC_{50}, 2,900 nM), with the C-5 methoxy substituent. For these latter two pairs of compounds, an occasional cell line was highly sensitive: RS 4;11 cells had IC_{50} values of 39 nM with **3e** and 1 nM with **3i**, and Jurkat cells had an IC_{50} value of 30 nM with **3i**. Average IC_{50} values for the compounds bearing no methoxy substituent were 3,300 and 2,600 nM for compounds **3a** and **3b**, respectively. Thus, even the C-5 methoxy substituent improved overall compound activity. Finally, we also prepared both the methoxy- and ethoxycarbonyl compounds with a C-7 ethoxy substituent (**3k** and **3l**, respectively). With all cell lines, the C-7-ethoxy compound was significantly less active than its cognate C-7-methoxy compound.

The most potent compound identified in this study was the 2-methoxycarbonyl-3-(3',4',5'-trimethoxyanilino)-6-methoxybenzo[*b*]furan derivative **3g**, which was more active than the reference compound CA-4 in five of the seven cancer cell lines, while the two compounds had similar activity against Jurkat and HL-60 cells. The antiproliferative data obtained with **3g** may indicate that an anilinic nitrogen with a hydrogen as a proton bonding donor at the C-3 position of the benzo[*b*]furan skeleton can be a good surrogate for the carbonyl group in compounds with general structure **2**.

In comparing the two series of 2-alkoxycarbonyl derivatives with the methoxy group at the same position of the benzo[*b*]furan nucleus, the 2-methoxycarbonyl derivative generally had greater activity than its ethoxycarbonyl counterpart (i.e., **3e** *vs.* **3f**, **3g** *vs.* **3h**, **3i** *vs.* **3j**, **3k** *vs.* **3l**).

Evaluation of antiproliferative activity in non-cancer cells. We investigated the effects of the two most active compounds (**3g** and **3h**) on non-cancer cells. We examined human peripheral blood lymphocytes (PBLs) and HUVECs isolated from healthy donors.

As shown in Table 2, in both unstimulated and mitogen- activated lymphocytes, the two compounds had little toxicity as compared to tumor cells. Somewhat greater toxicity was noted in HUVECs incubated with the two compounds, although also in this case the IC_{50} values were substantially higher than those obtained with the tumor cells. Moreover, in contrast to what was found with the tumor cells, **3h** was more active than **3g** in the non-cancer cells. These results suggest that **3g** and **3h** may have a preferential selectivity toward cancer cells.

Table 2. Cytotoxicity of **3c** and **3f** in human non-cancer cells

Cell line	IC_{50} (μM) [a]	
	3g	**3h**
$PBL_{resting}$ [b]	>10	>10
PBL_{PHA} [c]	>10	6.3±1.0
HUVEC	0.75±0.4	0.22±0.1

[a] Compound concentration required to reduce cell growth by 50%.

[b] PBL not stimulated with PHA.

[c] PBL stimulated with PHA.

Values are the mean ± SEM for three separate experiments

Inhibition of tubulin polymerization and colchicine binding. Compounds **3e** and **3g-j** and the reference compound CA-4 were evaluated for inhibitory effects on tubulin polymerization and on the binding of [^{3}H]colchicine to tubulin for an indication whether their antiproliferative effects might be caused by an interaction with microtubules (Table 3) [161-163]. The most potent of the compounds examined was **3g**, with an assembly IC_{50} of 1.1 μM, the same value obtained with CA-4, while **3h** was slightly less active than CA-4. This is in agreement with **3g** being the compound with the greatest antiproliferative activity. Compounds **3e**, **3i** and **3j** were 6-7-fold less active than CA-4, with IC_{50} values of 7.5, 7.6 and 6.4 μM, respectively, which was consistent with their lower antiproliferative activity.

Colchicine binding studies were performed on the only derivatives (**3g** and **3h**) with tubulin assembly IC_{50} values lower than 5 μM. In reaction mixtures containing 1.0 μM tubulin and 5.0 μM [^{3}H]colchicine, compound **3g** potently inhibited the binding to [^{3}H]colchicine to tubulin, with 83% inhibition occurring when **3g** and radiolabeled drug were at 5.0 μM in the reaction mixture. Compound **3g** was less potent than **1a**, which in these experiments inhibited colchicine binding by 99%. Derivative **3h** was slightly less potent than **3g**, with 74% inhibition occurring with the compound at 5.0 μM.

For the most active compounds **3g** and **3h**, a good correlation was observed between antiproliferative activities and inhibition of tubulin polymerization and colchicine binding. These results suggest that these two derivatives act as microtubule-depolymerizing agents through an interaction with tubulin at the colchicine site or a site that overlaps the colchicine site.

Table 3. Inhibition of tubulin polymerization and colchicine binding by compounds 3e, 3g-j and CA-4

Compound	**Tubulin assembly[a]** **IC_{50}±SD (μM)**	**Colchicine binding[b]** **% inhibition±SD**
3e	7.5±0.5	n.d.
3g	1.1±0.1	83±0.5
3h	1.5±0.2	74±4.1
3i	7.6±1.0	n.d.
3j	6.4±0.9	n.d.
CA-4 (1a)	1.1±0.1	99±0.1

[a] Inhibition of tubulin polymerization. Tubulin was at 10 μM.

[b] Inhibition of [^{3}H]colchicine binding. Tubulin, colchicine and tested compound were at 1, 5 and 5 μM, respectively.

n.d.: not determined

5.3 Molecular modeling. In order to investigate the possible binding mode of these novel compounds, a series of molecular docking studies were performed in the colchicine site of tubulin. In the binding mode for compound **3g** presented in Figure 1, the trimethoxyphenyl ring of the compound is in proximity to Cys241. Furthermore, there is a potential hydrogen bond between the ester moiety and Ala250, an interaction observed with other colchicine site agents [164].

These results could provide an explanation for the difference in biological activity observed for the compounds bearing a substituent in position 4, 5 or 7 of the benzo[*b*[furan (e.g. **3c**, **3e** and **3i)** versus **3g** with its 6-methoxy group. Our models indicate that the colchicine-binding pocket cannot readily accommodate the compounds with the 4-, 5- or 7-methoxy substituents.

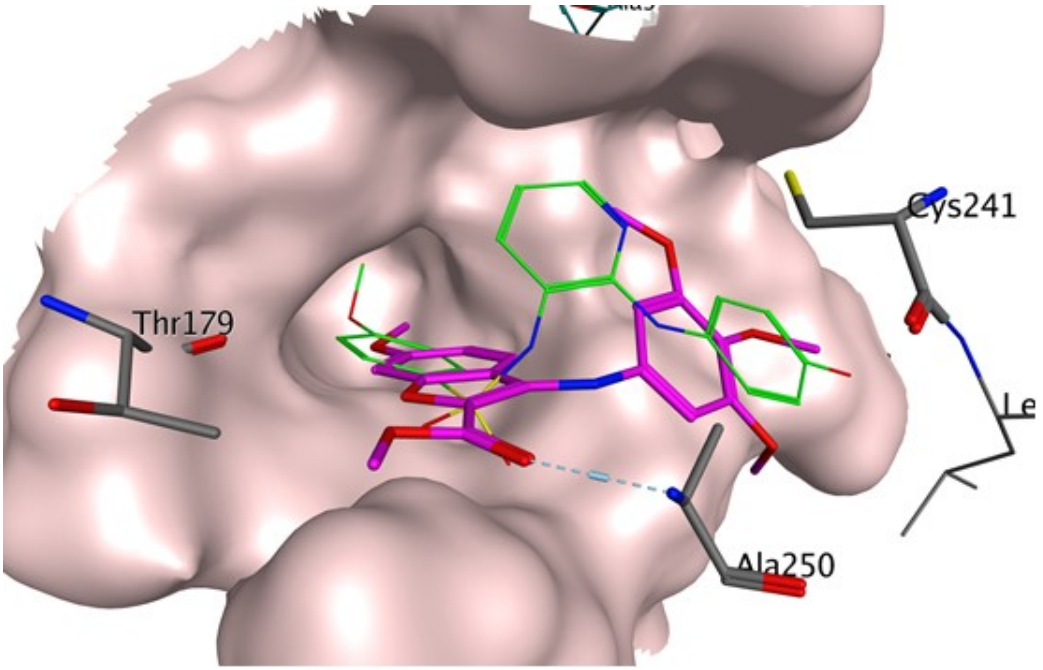

Figure 1. Proposed binding of 3g (represented in magenta) in the colchicine site of tubulin (PDB:3HKC). The co-crystallized ligand *N*-[2-[(4-Hydroxyphenyl)amino]-3-pyridinyl]-4-methoxybenzenesulfonamide (ABT751) is represented in green

5.4 Analysis of cell cycle effects. The effects of a 24 h treatment with different concentrations of **3g** or **3h** on cell cycle progression was determined by flow cytometry in Jurkat and HeLa cells (Figure 2, Panels A and B). The two compounds caused a significant G2/M arrest in a concentration-dependent manner in the cell lines tested, with a rise in G2/M cells occurring at a concentration as low as 60 nM, while at higher concentrations more than 70% of the cells were arrested in G2/M. The cell cycle arrest in G2/M phase was accompanied by a comparable reduction in the proportion of cells in both the G1 and S phases of the cell cycle.

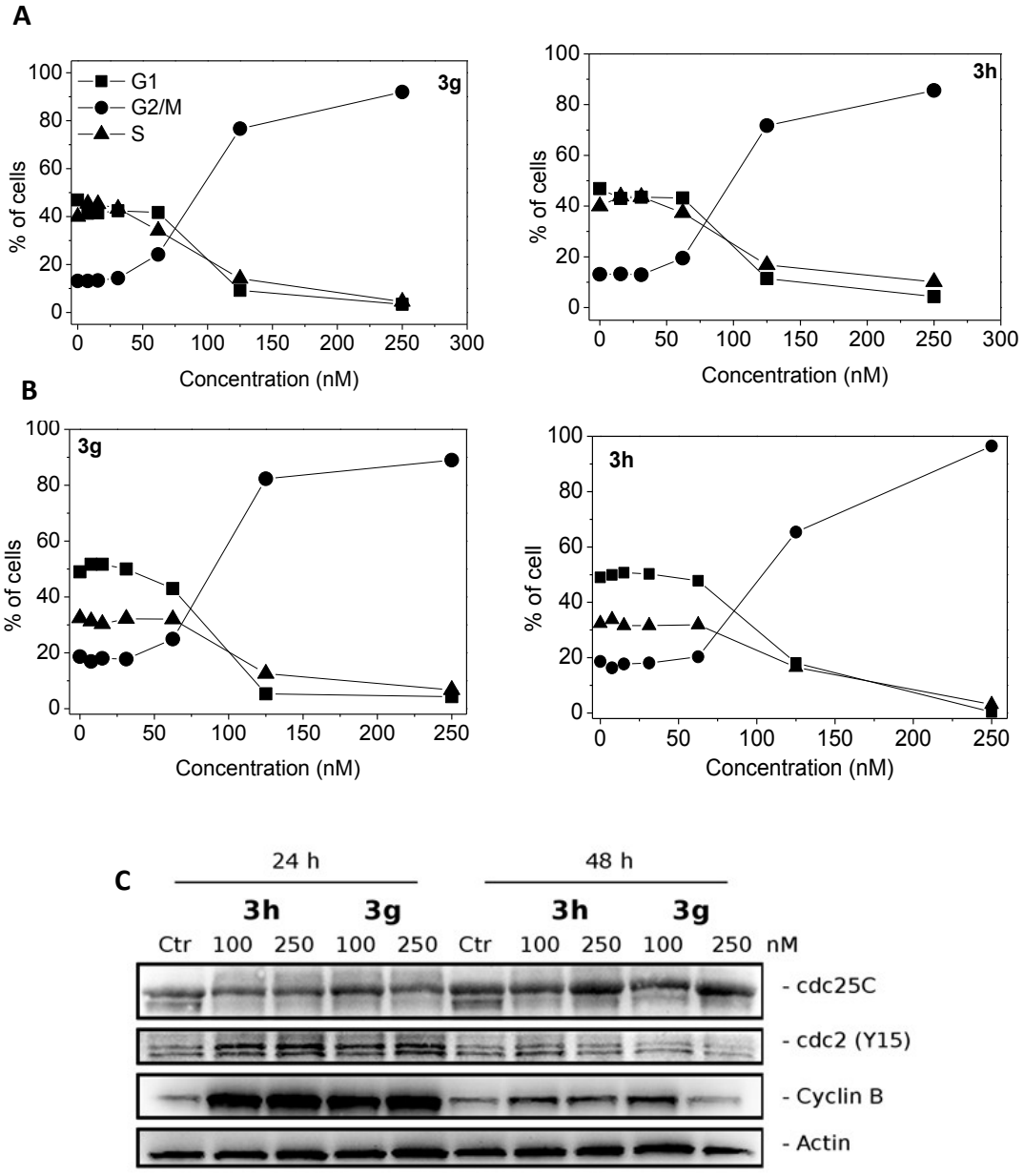

Figure 2. Percentage of cells in each phase of the cell cycle in Jurkat (Panel A) and HeLa (Panel B) cells treated with 3g or 3h at the indicated concentrations for 24 h. Cells were fixed and labeled with PI and analyzed by flow cytometry as described in the Experimental section. Panel C. Western blot analysis of some G2/M regulatory proteins after treatment with 3g or 3h. HeLa cells were treated for 24 or 48 h with the indicated concentration of compound. The cells were harvested and lysed for the detection of cyclin B, p-cdc2^{Y15} and cdc25c expression. To confirm equal protein loading, each membrane was stripped and reprobed with anti-β-actin antibody**.**

We next studied the association between the induced G2/M arrest by the two compounds and alterations in expression of various proteins that regulate cell division. As shown in Figure 2 (Panel C) in HeLa cells, a 24 h treatment with either compound at 100 nM or 250 nM caused a significant increase in cyclin B expression, which, in association with cdc2, controls both entry into and exit from mitosis [165,166]. After a 48 h treatment, cyclin B expression decreased. More importantly, p-cdc2^{Tyr15} expression increased after a 24 h treatment, while at 48 h a slight decrease was observed. However, no major changes in the expression of phosphatase cdc25c were observed.

These results indicate that arrest at G2/M induced by the compounds is caused by an increase of cyclin B activity, followed by its accumulation, leading to a decrease of p-cdc2 ^{Tyr15}. The decline in the level of p-cdc2^{Tyr15} at 48 h was more marked at the highest concentration (250 nM) examined.

5.5 Compounds 3g and 3h induce apoptosis through the mitochondrial pathway. The mode of cell death induced by **3g** and **3h** was investigated with the annexin-V assay [167]. As depicted in Figure 3 (Panels A and B), HeLa cells treated with **3g** or **3h** for 24 or 48 h showed an accumulation of annexin-V positive cells in comparison with the control, in a concentration and time-dependent manner, and this is indicative of the occurrence of apoptosis.

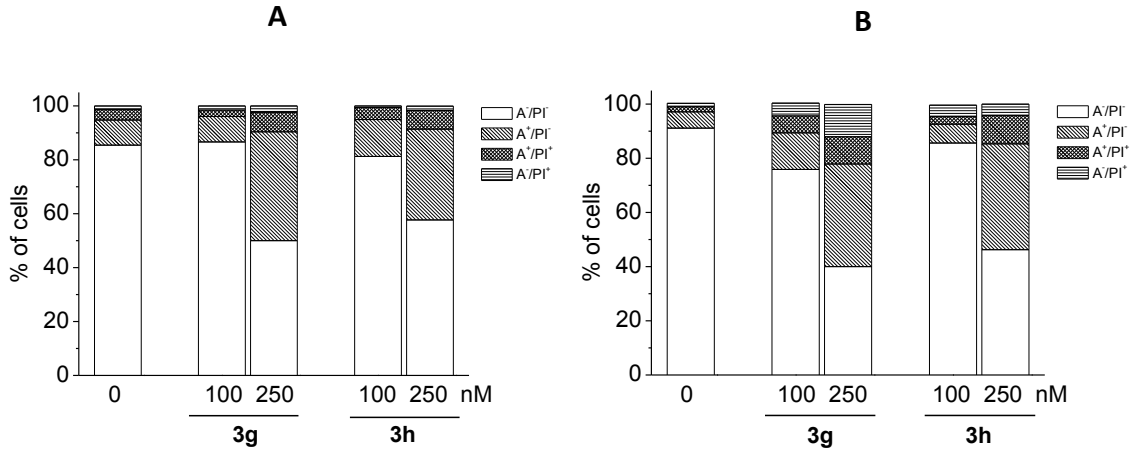

Figure 3. Flow cytometric analysis of apoptotic cells after treatment of HeLa cells with **3g** or **3h** at the indicated concentrations after incubation for 24 (Panel A) or 48 h (Panel B). The cells were harvested and labeled with annexin-V-FITC and PI and analyzed by flow cytometry

Since many antimitotic compounds induce apoptosis through the mitochondrial pathway [133,168-170] we determined whether **3g** and **3h** induced an alteration of the mitochondrial transmembrane potential ($\Delta\psi_{mt}$). $\Delta\psi_{mt}$ was monitored by flow cytometry using the dye 5,5',6,6'-tetrachloro-1,1',3,3'-tetraethylbenzimidazolcarbocyanine (JC-1). As shown in Figure 4 (Panel A) in HeLa cells, both **3g** and **3h** induced a time and concentration–dependent increase in the proportion of cells with depolarized mitochondria.

Mitochondrial membrane depolarization is associated with mitochondrial production of reactive oxygen species (ROS) [171].

Therefore, we investigated whether ROS production increased after treatment with the test compounds. We measured the production of ROS by flow cytometry utilizing 2,7-dichlorodihydrofluorescein diacetate (H_2-DCFDA).

As shown in Figure 4 (Panel B), both **3g** and **3h** induced the production of significant amounts of ROS in comparison with control cells, in agreement with the dissipation of $\Delta\psi_{mt}$. Altogether, these results indicate that these compounds induced apoptosis through the mitochondrial pathway.

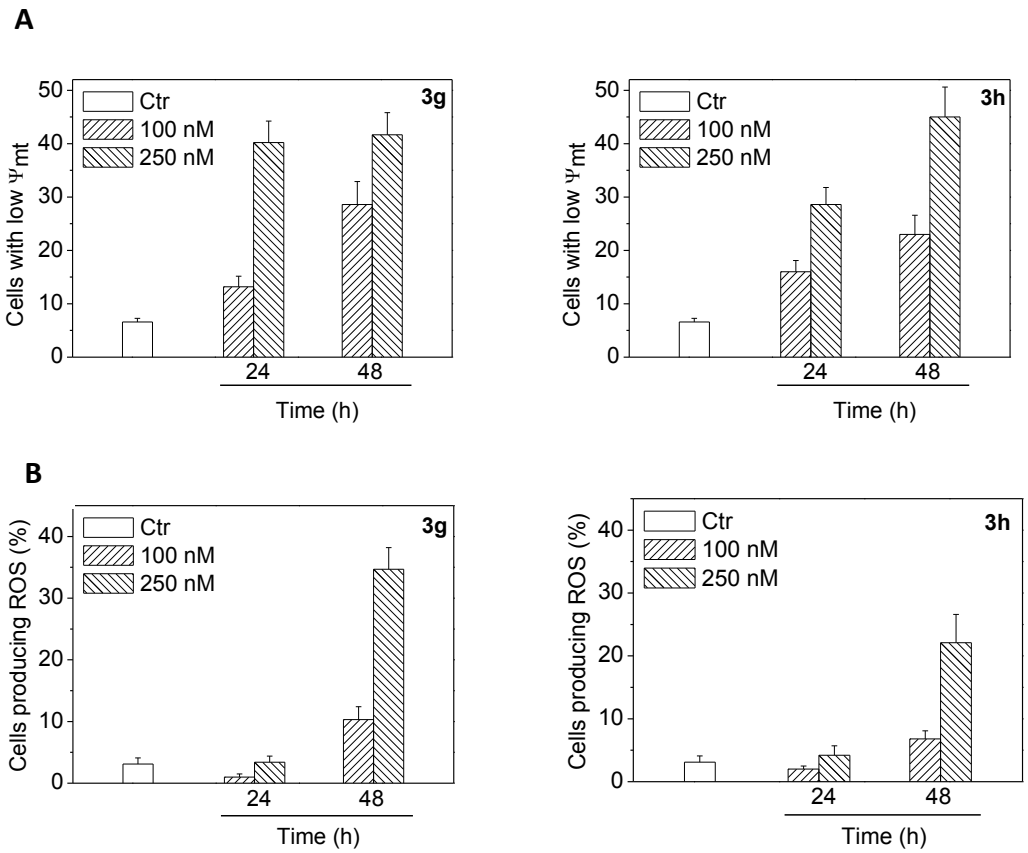

Figure 4. A) Assessment of mitochondrial membrane potential ($\Delta\psi_{mt}$) after treatment of HeLa cells with compounds 3g or 3h. Cells were treated with the indicated concentration of compounds for 24 or 48 h and then stained with the fluorescent probe JC-1. Data are presented as mean ± S.E.M. of three independent experiments. B) Mitochondrial production of ROS in HeLa cells following treatment with compound 3g or compound 3h. After 24 or 48 h incubations, cells were stained with H_2-DCFDA and analyzed by flow cytometry. Data are presented as mean ± S.E.M. of three independent experiments.

5.6 Compounds 3g and 3h induce activation of caspases and down-regulation of the anti-apoptotic proteins Bcl-2 and Mcl-1. To determine whether compounds **3g** and **3h** induced caspase-dependent cell death, we performed an immunoblot analysis of the activation of caspase-9 and caspase-3, two caspases involved in the apoptotic mitochondrial pathway. Exposure of HeLa cells to either compound resulted in the activation of caspase-9 and caspase-3 in a time and concentration dependent manner, as shown in Figure 5. Moreover, we also observed the cleavage of poly(ADP-ribose) polymerase (PARP), which is one of the main cleavage targets of caspase-3, both *in vitro* and *in vivo*[172].

Many recent studies have shown that regulation of the Bcl-2 family of proteins shares the signaling pathways induced by antimicrotubule compounds [133,168]. Several pro-apoptotic family proteins (e.g., Bax, Bid, Bim and Bak) promote the release of cytochrome *c*, whereas anti-apoptotic members (Bcl-2, Bcl-XL and Mcl-1) are capable of antagonizing the pro-apoptotic proteins and preventing the loss of mitochondrial membrane potential. In agreement with these observations, we found that Bcl-2 after a 48 h treatment with either compound was reduced, while the expression of Mcl-1, which is another anti-apoptotic member of the Bcl-2 family, was also strongly down regulated. This change was observed after 48 h treatments at both 100 and 250 nM. However, at 24 h we observed an increase in the expression of Mcl-1 with **3g** but not with **3h**.

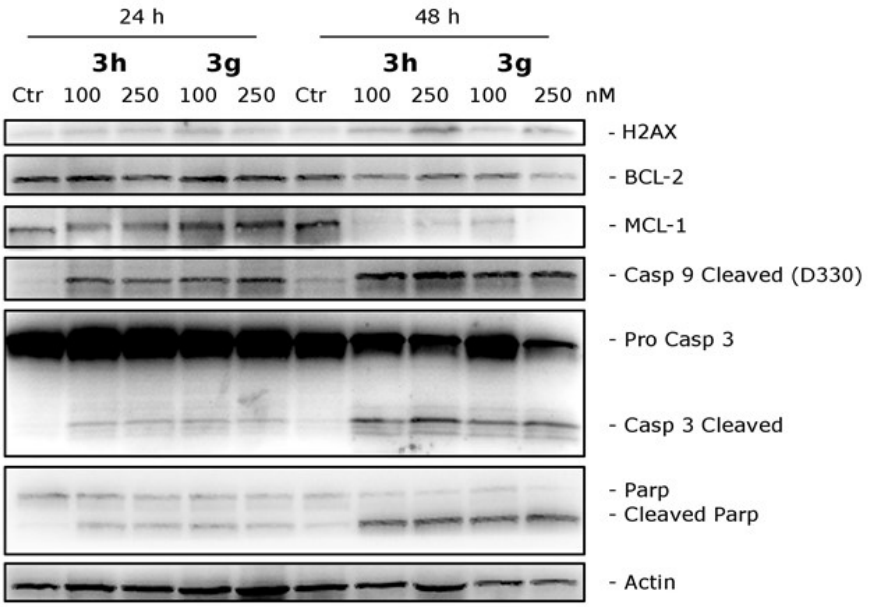

Figure 5. Western blot analysis of H2AX, Bcl-2 Mcl-1, caspase-3, cleaved caspase-9 and PARP after treatment of HeLa cells with **3g** or **3h** at the indicated concentrations for the indicated times. To confirm equal protein loading, each membrane was stripped and reprobed with anti-β-actin antibody

Altogether, our findings indicate that **3g** and **3h** are able to down regulate the expression of antiapoptotic proteins in line with recent reports that suggest that sensitivity to antimitotic drugs is regulated by Mcl-1 levels [173].

5.7Evaluation of antitumor activity of compound 3g *in vivo*. To determine the *in vivo* antitumor activity of **3g**, a syngeneic hepatocellular carcinoma model in mice was used [145]. In preliminary experiments *in vitro*, we had determined that both compound **3g** and CA-4, used as reference compound, showed potent cytotoxic activity (**3g**, IC_{50}=1.2±0.6 nM; CA-4, IC_{50}=0.9±0.5 nM) against BNL 1ME A.7R.1 cells.

Tumors were established by subcutaneous injection of BNL 1ME A.7R.1 cells into the backs of Balb/c mice. Once the tumor reached a measurable size (about 100 mm^3), twenty mice were randomly assigned to one of four groups. In two of the groups, compound **3g** was injected intraperitoneally at doses of 5 and 10 mg/kg, respectively. In a third group, CA-4P was injected at 5 mg/kg, while the fourth group was used as a control. As shown in Figure 6 (Panel A), compound **3g** caused a significant reduction in tumor growth (44.5%), as compared with administration of vehicle, at the dose of 10 mg/kg but not at 5 mg/kg. At the lower dose the growth inhibition shown in the figure did not reach statistical significance. The effect of 5 mg/kg of CA-4P was not substantially different from that of 10 mg/kg of **3g**, and the CA-4P effect was significant relative to the control. During the treatment period, only a small decrease in body weight occurred in the animals treated with **3g** at the higher concentration (Figure 6, Panel B).

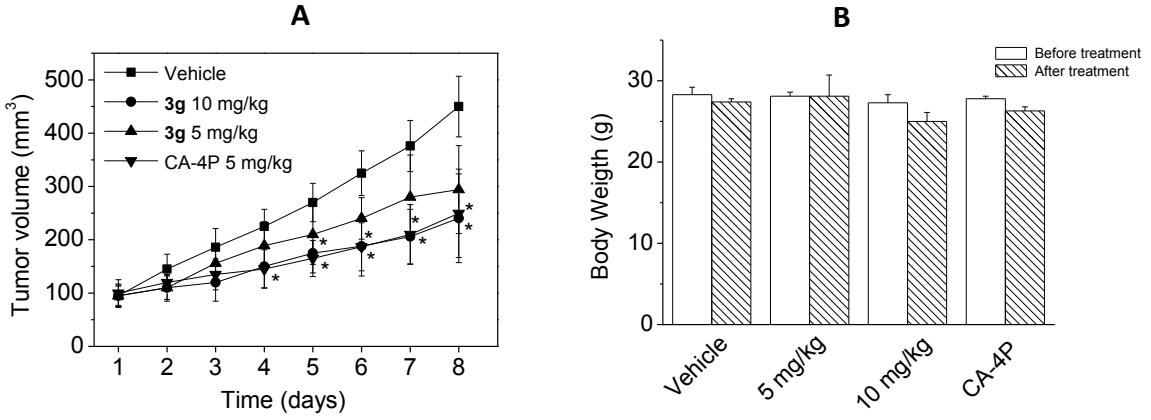

Figure 6. Inhibition of mouse allograft growth *in vivo* by compound 3g. (A). Male mice were injected subcutaneously at their dorsal region with 10^7 BNL 1MEA.7R.1 cells, a syngenic hepatocellular carcinoma cell line. Tumor-bearing mice were administered the vehicle, as control, or 3g at the doses of 5 mg/kg or 10 mg/kg or CA-4P (5 mg/kg) as reference compound. Injections were given intraperitoneally daily starting on day 1. The figure shows the average measured tumor volumes (A) and body weights of the mice (B) recorded at the beginning and at the end of the treatments. Data are presented as mean ± SEM of tumor volume and body weight at each time point for 5 animals per group. *$p<0.01$, *vs*. control

5.8 Derivative 3g has antivascular effects *in vitro* and *in vivo*. Recent antitumor strategies have included the use of chemotherapeutics with antiangiogenic or antivascular drugs to increase the efficacy of the treatment. Many tubulin binding agents show antivascular effects against tumor endothelium, including CA-4, and for that reason we evaluated **3g** for its effects on endothelial cells *in vitro*. We used HUVECs as a model to study angiogenesis *in vitro*.

Endothelial cell migration to the tumor site is an important mechanism of angiogenesis [142], and the inhibition of this process is a valuable strategy to arrest the development of tumor vasculature. With this aim, we evaluated endothelial cell motility by scratching a HUVEC monolayer and monitoring the ability of cells to reclose the wound.

As shown in Figure 7 (Panels A and B), **3g** was very efficient in arresting cell motility. The effect was statistically significant with only a 6 h incubation at 25 nM and became highly significant for all the tested concentrations after 24 h, even with only 5 nM **3g**.

To further evaluate the antivascular activity of **3g**, we analyzed the ability of the compound to disrupt the "tubule-like" structures formed by HUVECs seeded on Matrigel. Matrigel is an extracellular matrix rich in pro-angiogenic factors that stimulate single endothelial cells to assume an extended shape and produce a reticulum similar to a capillary network.

As shown in Figure 7 (Panels C-E), after a 1 h (Panels C and D) or 3 h (Panel E) incubation, the compound clearly disrupted the network of HUVECs, as compared with the control. After 3 h, all the tested concentrations were effective in altering the tubule-like structures (Figure 7, Panel C).

Image analysis [143] was performed to obtain a quantitative measurement of the total length of the tubules, the area and the number of meshes, the percent of area covered by HUVECs, and the number of branching points after both a 1 h (Figure 7, Panel D) and 3 h (Figure 7, Panel E) treatment. It is important to stress that **3g** exerted its antivascular effects *in vitro* at concentrations that did not affect HUVEC proliferation (see Table 2).

The antivascular activity of **3g** was also investigated *in vivo*. First, we used the chick embryo chorioallantoic membrane (CAM), which is a highly vascularized structure, as a model. Through alginate beads applied on the CAM, **3g** (1-100 pmol/egg) was slowly distributed within the membrane, starting from day 11 post egg fertilization, in the presence or absence of fibroblast growth factor (FGF) (100 ng/egg), a vascular growth factor. As shown in Figure 8 (Panel A), **3g** alone, at the highest concentration (100 pmol/egg) used, did not induce blood vessels to increase in number. On the other hand, treatment with FGF gave rise to an extensive production of blood vessels, and this increase was strongly reduced by **3g** treatment, even at the lowest tested concentration (1 pmol/egg).

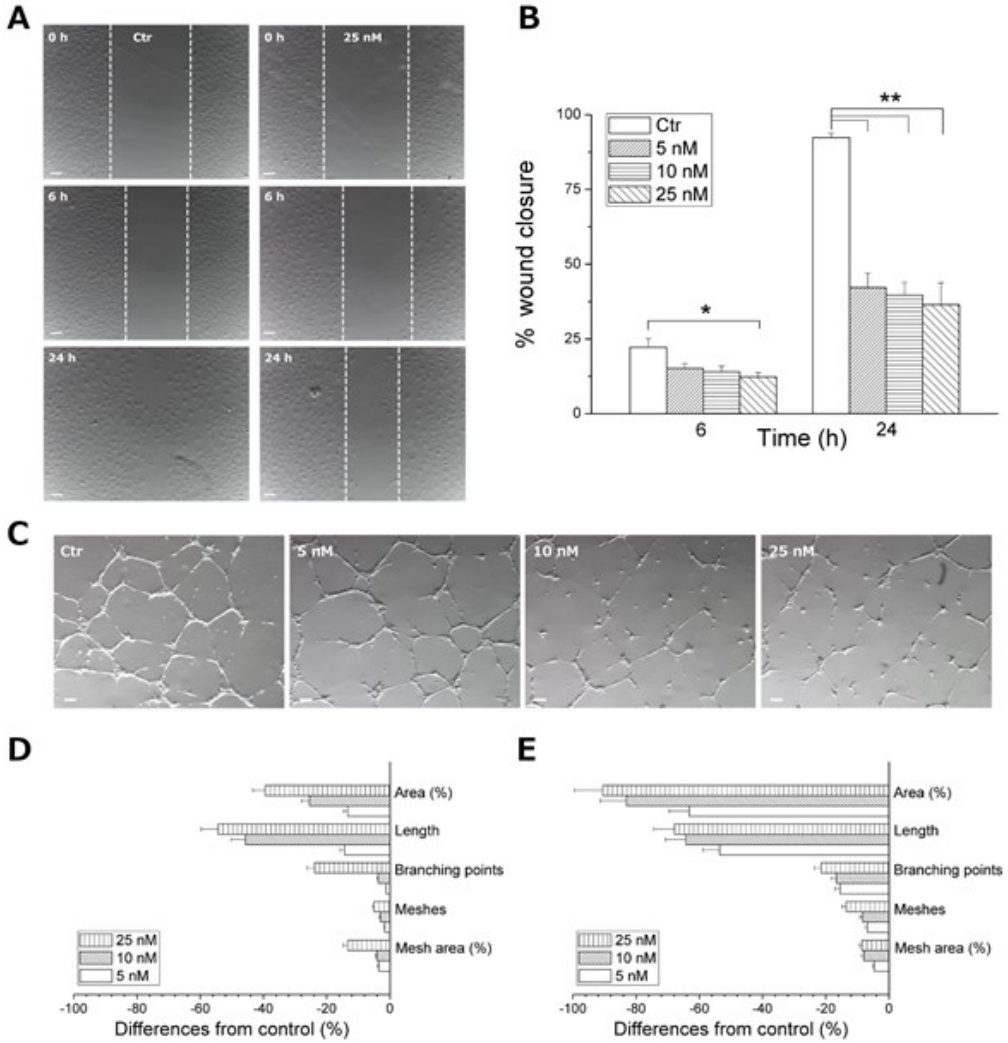

Figure 7. Compound 3g has antivascular activity *in vitro*. Panel A. Confluent HUVECs in a monolayer were wounded, and cells were treated with different concentrations of 3g and photographed at various times, 7x magnification; bar=100 μm. The dotted lines define the areas lacking cells. Panel B. The graph shows the quantitative effect of 3g. Migration was quantified by measuring the gap closure at the indicated times. Data are represented as mean ± S.E.M. of three independent experiments. *$p<0.05$, **$p<0.01$ vs control. Panel C. Inhibition of endothelial cell capillary-like tubule formation by 3g. Representative pictures (10x magnification; bar=100 μm) of preformed capillary-like tubules treated with increasing concentration of 3g for 1 h or 3 h. Panels D and E. Quantitative analysis of the effects of 3g on the dimensional and topological parameters of the preformed capillary-like tubule networks, after a 1 h (panel D) or a 3 h treatment (panel E). Data are represented as mean ± S.E.M. of three independent experiments

3g was further evaluated in a murine tumor model. BL6-B16 mouse melanoma cells, injected subcutaneously in syngeneic C57/BL6 mice, proliferate and generate tumor masses. After a 24 h treatment with **3g** at 30 mg/kg i.p., the tumor was excised and the blood vessels stained with an antibody against the endothelial marker CD31 and counted. As shown in Figure 8 (Panel B), the number and, especially, the size of the vessels were reduced. This reduction in number was about 20% and was statistically significant (Panel C, $P < 0.05$). Altogether our results indicate that **3g** is endowed with vascular disrupting properties both in *vitro* and *in vivo*. In addition, we also observed that the effects on endothelial cells induced by **3g** were similar to those observed after CA-4 treatment under the same experimental conditions, as described previously [144].

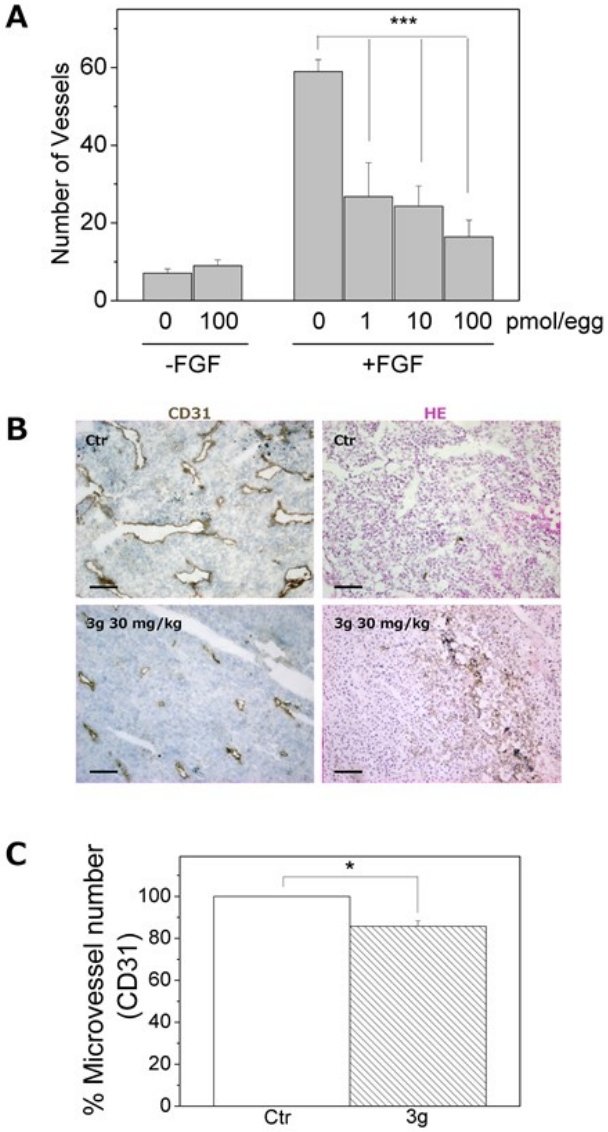

Figure 8. *In vivo* effects of 3g on angiogenesis. A. The CAM assay. Alginate sponges embedded with FGF, a stimulator of blood vessel formation, in the presence of the indicated concentrations of 3g, were implanted on the top of the growing CAM on day 11 of development. On day 14, newly formed blood vessels converging toward the implants were counted microscopically. Data represent mean ±SEM of at least six eggs for each group. ***p<0.001 vs control. B and C. Efficacy i*n vivo* of 3g in a syngeneic mouse model. B. BL6-B16 murine melanoma cells were injected in the right flank of C57BL/6 mice as described in the Experimental Section. Tumor tissues were embedded in OCT-compound and frozen for immunohistochemistry. CD31 immunohistochemistry and hematoxylin-eosin (HE) staining of tumor after i.p. treatment with 30 mg/kg of 3g (100x magnification). C. Quantitative analysis of tumor section stained with CD31 for blood vessel number. Data are represented as mean±SEM of five mice per group. *P < 0.05 versus control**.**

5.9 Conclusions

In conclusion, we demonstrated that the bioisosteric replacement of the carbonyl bridge between the C-3 position of the benzo[*b*]furan ring and the 3,4,5-trimethoxyphenyl moiety by an anilinic nitrogen resulted in highly bioactive antimitotic agents based on the 2-alkoxycarbonyl-3-(3',4',5'-trimethoxyanilino)benzo[*b*]furan molecular skeleton. Compounds **3g** and **3h** were prepared by an efficient two-step synthetic procedure, and both compounds showed activity comparable with that of CA-4. Our structure-activity relationship studies involved placing the electron-donating methoxy substituent at the C-4, C-5, C-6 or C-7 position on the benzo[*b*]furan ring. For both the series of alkoxycarbonyl derivatives, compounds **3c** and **3d** with the methoxy group at the C-4 position were inactive, and a substantial improvement in antiproliferative activity occurred with the methoxy group at the C-5 position (**3e** and **3f**). Simply moving the methoxy group to C-6 resulted in the highly active compounds **3g** and **3h**, while moving the methoxy to C-7 (**3i** and **3j**) resulted in a drastic reduction in activity. The 2-methoxycarbonyl-3-(3',4',5'-trimethoxyanilino)-6-methoxybenzo[*b*]furan derivative **3g** had the greatest antiproliferative IC_{50} values, ranging from 0.3 to 27 nM against the seven cancer cell lines we examined. Compound **3g** was also a potent inhibitor of tubulin assembly, with an IC_{50} of 1.1 μM, similar to that of CA-4. Nevertheless, this compound was less active than CA-4 as an inhibitor of the binding of [^{3}H]colchicine to tubulin, with 83% and 99% inhibition, respectively. Compound **3g**, *in vitro* was able to induce mitotic arrest followed by apoptosis through mitochondrial depolarization and activation of both caspase-9 and -3. Importantly, it exhibited significant antitumor activity *in vivo* and interesting antivascular properties. Thus, **3g** is a promising new tubulin binding agent with potential as an antitumor and antivascular agent that could improve common anticancer therapies.

5.10 Experimental Section

Chemistry. Materials and methods. ^{1}H NMR and ^{13}C NMR spectra were recorded in $CDCl_3$ solution with a Varian Mercury Plus 400 spectrometer at 400 MHz and 100 MHz, respectively. Peak positions are given in parts per million (δ) downfield from tetramethylsilane as internal standard, and *J* values are given in hertz. Positive-ion electrospray ionization (ESI) mass spectra were measured on a double-focusing Finnigan MAT 95 instrument with BE geometry. High resolution mass spectroscopic (HRMS) measurements were performed using an ESI-Q-TOF mass spectrometer (Agilent Technologies). Analytical HPLC analyses were performed at ambient temperature on a Beckman 125 liquid chromatograph fitted with a Luna C-18 column (4.6 x 100 mm, 3 μm particle size) with 0.1% TFA in H_2O (A) and 0.1% TFA in CH_3CN (B) solvent mixtures and equipped with a Beckman 168 diode array detector. Melting points (mp) were determined on a Buchi-Tottoli apparatus and are uncorrected. The purity of tested compounds was determined by combustion elemental analyses conducted by the Microanalytical Laboratory of the Chemistry Department of the University of Ferrara with a Yanagimoto MT-5 CHN recorder elemental analyzer. All tested compounds yielded data consistent with a purity of at least 95% as compared with the theoretical values. All reactions were carried out under an inert atmosphere of dry nitrogen, unless otherwise indicated. TLC was performed on silica gel (precoated F254 Merck plates), and compounds were visualized with aqueous $KMnO_4$. Flash column chromatography was performed using 230-400 mesh silica gel and the indicated solvent system. Organic solutions were dried over anhydrous Na_2SO_4. All commercial chemicals and solvents were reagent grade and were used without further treatment.

General procedure A for the synthesis of compounds 5a-l. A suspension of the appropriate 2-hydroxybenzonitrile **4a-f** (5 mmol), methyl/ethylbromoacetate (6 mmol, 1.2 equiv.) and K_2CO_3 (1.38 g., 10 mmol, 2 equiv.) in DMF (10 mL) was stirred at 60 °C for 4 h until consumption of the limiting reagent, followed by reflux heating for 8 h. The reaction mixture was cooled to ambient temperature and filtered through Celite, then the filtrate was evaporated *in vacuo*. The residue was dissolved with ethyl acetate (30 mL), and the solution was washed sequentially with water (10 mL) and brine (10 mL). The organic layer was dried, filtered and concentrated under reduced pressure, and the residue was purified by flash column chromatography on silica gel.

Methyl 3-amino-benzofuran-2-carboxylate (5a). Following general procedure A, the crude residue was purified by flash chromatography, using ethyl acetate:petroleum ether 2:8 (v:v) as eluent, to furnish **5a** as a yellow solid. Yield: 78%, mp 95-96 °C. ^{1}H-NMR ($CDCl_3$) δ: 3.97 (s, 3H), 4.99 (bs, 2H), 7.24 (m, 1H), 7.46 (m, 2H), 7.56 (dd, J=7.8 and 1.0 Hz, 1H). MS (ESI): $[M]^+$=191.5.

Ethyl 3-amino-benzofuran-2-carboxylate (5b). Following general procedure A, the crude residue was purified by flash chromatography, using ethyl acetate:petroleum ether 2:8 (v:v) as eluent, to furnish **5b** as a green solid. Yield: 72%, mp 83-84 °C. ^{1}H-NMR ($CDCl_3$) δ: 1.40 (t, J=7.2 Hz, 3H), 4.46 (q, J=7:2 Hz, 2H), 4.97 (bs, 2H), 7.24 (m, 1H), 7.46 (m, 2H), 7.57 (dd, J=7.8 and 1.0 Hz, 1H). MS (ESI): $[M+1]^+$=206.1.

Methyl 3-amino-4-methoxybenzofuran-2-carboxylate (5c). Following general procedure A, the crude residue was purified by flash chromatography, using ethyl acetate:petroleum ether 3:7 (v:v) as eluent, to furnish **5c** as a white solid. Yield: 75%, mp 148-149 °C. ^{1}H-NMR ($CDCl_3$) δ: 3.94 (s, 3H), 3.96 (s, 3H), 5.40 (bs, 2H), 6.58 (d, J=7.8 Hz, 1H), 6.99 (d, J=8.4 Hz, 1H), 7.54 (t, J=8.4 Hz, 1H). MS (ESI): $[M+1]^+$=221.2.

Ethyl 3-amino-4-methoxybenzofuran-2-carboxylate (5d). Following general procedure A, the crude residue was purified by flash chromatography, using ethyl acetate:petroleum ether 3:7 (v:v) as eluent, to furnish **5d** as a colorless oil. Yield: 58%. ^{1}H-NMR ($CDCl_3$) δ: 1.42 (t, J=7.2 Hz, 3H), 3.95 (s, 3H), 4.38 (q, J=7.2 Hz, 2H), 5.42 (bs, 2H), 6.55 (d, J=8.2 Hz, 1H), 7.04 (d, J=8.6 Hz, 1H), 7.32 (t, J=8.6 Hz, 1H). MS (ESI): $[M+1]^+$=236.3.

Methyl 3-amino-5-methoxy-benzofuran-2-carboxylate (5e). Following general procedure A, the crude residue was purified by flash chromatography, using ethyl acetate:petroleum ether 4:6 (v:v) as eluent, to furnish **5e** as a brown solid. Yield: 63%, mp 163-165 °C. ^{1}H-NMR ($CDCl_3$) δ: 3.86 (s, 3H), 3.96 (s, 3H), 4.90 (bs, 2H), 6.92 (d, J=2.4 Hz, 1H), 7.06 (dd, J=9.2 and 2.4 Hz, 1H), 7.61 (d, J=9.2 Hz, 1H). MS (ESI): $[M+1]^+$=222.2.

Ethyl 3-amino-5-methoxy-benzofuran-2-carboxylate (5f). Following general procedure A, the crude residue was purified by flash chromatography, using ethyl acetate:petroleum ether 3:7 (v:v) as eluent, to furnish **5f** as a yellow solid. Yield: 53%, mp 151-153 °C. ^{1}H-NMR ($CDCl_3$) δ: 1.43 (t, J=7.0 Hz, 3H), 3.86 (s, 3H), 4.45 (q, J=7.0 Hz, 2H), 4.89 (bs, 2H), 6.92 (d, J=2.4 Hz, 1H), 7.05 (dd, J=9.0 and 2.4 Hz, 1H), 7.33 (d, J=9.0 Hz, 1H). MS (ESI): $[M+1]^+$=236.2.

Methyl 3-amino-6-methoxybenzofuran-2-carboxylate (5g). Following general procedure A, the crude residue was purified by flash chromatography, using ethyl acetate:petroleum ether 3:7 (v:v) as eluent, to furnish **5g** as a cream colored solid. Yield: 73%, mp 150-151 °C. ^{1}H-NMR ($CDCl_3$) 3.84 (s, 3H), 3.94 (s, 3H), 4.97 (bs, 2H), 6.83 (dd, J=8.6 and 2.2 Hz, 1H), 6.91 (d, J=2.2 Hz, 1H), 7.39 (d, J=8.6 Hz, 1H). MS (ESI): $[M+1]^+$=222.1.

Ethyl 3-amino-6-methoxybenzofuran-2-carboxylate (5h). Following general procedure A, the crude residue was purified by flash chromatography, using ethyl acetate:petroleum ether 3:7 (v:v) as eluent, to furnish **5h** as a yellow solid. Yield: 52%, mp 145-147 °C. ^{1}H-NMR (d_6-DMSO) 1.43 (t, J=7.0 Hz, 3H), 3.85 (s, 3H), 4.40 (q, J=7.0 Hz, 2H), 4.95 (bs, 2H), 6.85 (dd, J=8.8 and 2.2 Hz, 1H), 6.93 (d, J=2.2 Hz, 1H), 7.43 (d, J=8.8 Hz, 1H). MS (ESI): $[M+1]^+$=236.2.

Methyl 3-amino-7-methoxybenzofuran-2-carboxylate (5i). Following general procedure A, the crude residue was purified by flash chromatography, using ethyl acetate:petroleum ether 3:7 (v:v) as eluent, to furnish **5i** as a brown solid. Yield: 61%, mp 149-151 °C. ^{1}H-NMR ($CDCl_3$) 3.94 (s, 3H), 3.98 (s, 3H), 4.96 (bs, 2H), 6.91 (dd, J=7.0 and 2.0 Hz, 1H), 7.14 (m, 2H). MS (ESI): $[M+1]^+$=222.1.

Ethyl 3-amino-7-methoxybenzofuran-2-carboxylate (5j). Following general procedure A, the crude residue was purified by flash chromatography, using ethyl acetate:petroleum ether 3:7 (v:v) as eluent, to furnish **5j** as a yellow solid. Yield: 78%, mp 123-125 °C. ^{1}H-NMR ($CDCl_3$) 1.42 (t,

J=7.0 Hz, 3H), 3.99 (s, 3H), 4.40 (q, J=7.0 Hz, 2H), 4.95 (bs, 2H), 6.90 (dd, J=6.8 and 1.8 Hz, 1H), 7.13 (m, 2H). MS (ESI): $[M+1]^+$=236.2.

Methyl 3-amino-7-ethoxybenzofuran-2-carboxylate (5k). Following general procedure A, the crude residue was purified by flash chromatography, using ethyl acetate:petroleum ether 3:7 (v:v) as eluent, to furnish **5k** as a yellow solid. Yield: 58%, mp 139-141 °C. ^{1}H-NMR ($CDCl_3$) 1.50 (t, J=7.2 Hz, 3H), 3.94 (s, 3H), 4.21 (q, J=7.2 Hz, 2H), 4.95 (bs, 2H), 6.91 (dd, J=6.8 and 2.2 Hz, 1H), 7.12 (m, 2H). MS (ESI): $[M+1]^+$=236.3.

Ethyl 3-amino-7-ethoxybenzofuran-2-carboxylate (5l). Following general procedure A, the crude residue was purified by flash chromatography, using ethyl acetate:petroleum ether 3:7 (v:v) as eluent, to furnish **5l** as a yellow solid. Yield: 62%, mp 112-114 °C. ^{1}H-NMR ($CDCl_3$) 1.42 (t, J=7.2 Hz, 3H), 1.51 (t, J=7.0 Hz, 3H), 4.26 (q, J=7.2 Hz, 2H), 4.41 (q, J=7.0 Hz, 2H), 4.93 (bs, 2H), 6.94 (dd, J=7.0 and 2.2 Hz, 1H), 7.12 (m, 2H). MS (ESI): $[M+1]^+$=250.3.

General procedure B for the preparation of compounds 3a-l. To a dry Schlenk tube, dry toluene (5 mL), 3-aminobenzofuran derivative **5a-l** (0.5 mmol), $Pd(OAc)_2$ (6 mol%, 30 mg), *rac*-BINAP (4 mol%, 30 mg), $CsCO_3$ (230 mg, 0.7 mmol, 1.4 equiv.) and 5-bromo-1,2,3-trimethoxybenzene (148 mg, 0.6 mmol, 1.2 equiv.) were added under Ar, and the mixture was heated with stirring at 120 °C for 18 h. Upon cooling, ethyl acetate was added (5 mL), the mixture was filtered through Celite under vacuum and the filtrate diluted with ethyl acetate (10 mL) and water (5 mL). The aqueous phase was separated and further extracted with ethyl acetate (2x5 mL). The combined organic phases were washed with brine (5 mL), dried, concentrated under reduced pressure and yielded a residue that was purified by flash column chromatography on silica gel.

Methyl 3-[(3,4,5-trimethoxyphenyl)amino]-benzofuran-2-carboxylate (3a). Following general procedure B, the crude residue was purified by flash chromatography, using ethyl acetate:petroleum ether 2:8 (v:v) as eluent, to furnish **3a** as a yellow solid. Yield: 67%, mp 176-178 °C. ^{1}H-NMR ($CDCl_3$) δ: 3.77 (s, 6H), 3.87 (s, 3H), 4.00 (s, 3H), 6.42 (s, 2H), 7.05 (m, 1H), 7.34 (d, J=7.8 Hz, 1H), 7.48 (m, 2H), 7.74 (s, 1H). ^{13}C-NMR ($CDCl_3$) δ: 51.9, 56.2 (2x), 61.2, 99.6 (2x), 112.8, 117.8, 120.9, 122.1, 123.6, 123.8, 128.8, 136.8, 137.1, 153.6 (2x), 154.6, 157.3. MS (ESI): $[M+1]^+$=357.9.

Ethyl 3-[(3,4,5-trimethoxyphenyl)amino]-benzofuran-2-carboxylate (3b). Following general procedure B, the crude residue was purified by flash chromatography, using ethyl acetate:petroleum ether 3:7 (v:v) as eluent, to furnish **3b** as a yellow solid. Yield: 56%, mp 122-124 °C. ^{1}H-NMR ($CDCl_3$) δ: 1.46 (t, J=7.0 Hz, 3H), 3.77 (s, 6H), 3.86 (s, 3H), 4.45 (q, J=7.0 Hz, 2H), 6.41 (s, 2H), 7.12 (m, 1H), 7.32 (d, J=7.8 Hz, 1H), 7.54 (m, 2H), 7.80 (s, 1H). ^{13}C-NMR ($CDCl_3$) δ: 14.6, 56.1 (2x), 60.8, 61.1, 99.4 (2x), 109.9, 112.8, 117.8, 120.9, 121.9, 123.5, 128.6, 136.5, 126.8, 153.5 (2x), 154.4, 158.1. MS (ESI): $[M+1]^+$=372.4.

Methyl 3-(3,4,5-trimethoxyphenylamino)-4-methoxybenzofuran-2-carboxylate (3c). Following general procedure B, the crude residue was purified by flash chromatography, using ethyl acetate:petroleum ether 3:7 (v:v) as eluent, to furnish **3c** as a white solid. Yield: 63%, mp 171-172 °C. ^{1}H-NMR ($CDCl_3$) δ: 3.66 (s, 6H), 3.78 (s, 3H), 3.84 (s, 3H), 3.91 (s, 3H), 6.38 (s, 2H), 7.02 (dd, J=8.6 and 2.0 Hz, 1H), 7.32 (d, J=2.0 Hz, 1H), 7.48 (d, J=8.6 Hz, 1H), 7.77 (s, 1H). ^{13}C-NMR ($CDCl_3$) δ: 51.8, 53.2, 56.8 (2x), 60.9, 99.6 (2x), 105.2, 105.9, 107.2, 119.4, 124.6, 127.7, 135.1, 135.8, 153.6 (2x), 155.8, 155.9, 163.3. MS (ESI): $[M+1]^+$=388.2.

Ethyl 3-(3,4,5-trimethoxyphenylamino)-4-methoxybenzofuran-2-carboxylate (3d). Following general procedure B, the crude residue was purified by flash chromatography, using ethyl acetate:petroleum ether 3:7 (v:v) as eluent, to furnish **3d** as a yellow solid. Yield: 61%, mp 83-85 °C. ^{1}H-NMR ($CDCl_3$) δ: 1.44 (t, J=7.2 Hz, 3H), 3.68 (s, 6H), 3.76 (s, 3H), 3.94 (s, 3H), 4.32 (q, J=7.2 Hz, 2H), 6.32 (s, 2H), 6.49 (d, J=8.2 Hz, 1H), 6.95 (d, J=8.6 Hz, 1H), 7.34 (t, J=8.6 Hz, 1H), 7.77 (s, 1H). ^{13}C-NMR ($CDCl_3$) δ: 14.4, 51.8, 53.3, 56.7 (2x), 99.6 (2x), 104.5, 105.2, 105.7, 107.0, 118.8, 124.5, 127.9, 135.0, 135.6, 153.8 (2x), 155.9, 160.0, 163.8. MS (ESI): $[M+1]^+$=402.2.

Methyl 3-(3,4,5-trimethoxyphenylamino)-5-methoxybenzofuran-2-carboxylate (3e). Following general procedure B, the crude residue was purified by flash chromatography, using ethyl acetate:petroleum ether 3:7 (v:v) as eluent, to furnish **3e** as a yellow solid. Yield: 53% yield, mp 140-142 °C. ^{1}H-NMR ($CDCl_3$) δ: 3.65 (s, 3H), 3.79 (s, 6H), 3.86 (s, 3H), 3.99 (s, 3H), 6.48 (s, 2H), 6.68 (d, J=2.8 Hz, 1H), 7.07 (dd, J=9.0 and 2.8 Hz, 1H), 7.42 (d, J=9.0 Hz, 1H), 7.78 (s, 1H). ^{13}C-NMR ($CDCl_3$) δ: 51.9, 55.9, 56.2 (2x), 61.2, 99.3 (2x), 104.5, 112.8, 113.5, 113.8, 116.5, 118.9, 132.2, 132.6, 135.8, 136.9, 153.6 (2x), 158.2. MS (ESI): $[M+1]^+$=388.0.

Ethyl 3-(3,4,5-trimethoxyphenylamino)-5-methoxybenzofuran-2-carboxylate (3f). Following general procedure B, the crude residue was purified by flash chromatography, using ethyl acetate:petroleum ether 3:7 (v:v) as eluent, to furnish **3f** as a yellow solid. Yield: 56% yield, mp 105-107 °C. ^{1}H-NMR ($CDCl_3$) δ: 1.46 (t, J=7.0 Hz, 3H), 3.65 (s, 3H), 3.79 (s, 6H), 3.86 (s, 3H), 4.44 (q, J=7.0 Hz, 2H), 6.40 (s, 2H), 6.69 (d, J=2.8 Hz, 1H), 7.07 (dd, J=9.2 and 2.8 Hz, 1H), 7.43 (d, J=9.2 Hz, 1H), 7.70 (s, 1H). ^{13}C-NMR ($CDCl_3$) δ: 14.7, 55.9, 55.2 (2x), 60.9, 61.2, 99.1 (2x), 104.5, 113.6, 118.8, 121.3, 128.9, 134.4, 136.4, 137.0, 149.6, 153.6 (2x), 154.9, 161.9. MS (ESI): $[M+1]^+$=402.2.

Methyl 3-(3,4,5-trimethoxyphenylamino)-6-methoxybenzofuran-2-carboxylate (3g). Following general procedure B, the crude residue was purified by flash chromatography, using ethyl acetate:petroleum ether 3:7 (v:v) as eluent, to furnish **3g** as a yellow solid. Yield: 78%, mp 143-145 °C. ^{1}H-NMR ($CDCl_3$) δ: 3.78 (s, 6H), 3.85 (s, 3H), 3.86 (s, 3H), 3.97 (s, 3H), 6.42 (s, 2H), 6.71 (dd, J=8.8 and 1.8 Hz, 1H), 6.94 (d, J=1.8 Hz, 1H), 7.18 (d, J=8.8 Hz, 1H), 7.72 (s, 1H). ^{13}C-NMR ($CDCl_3$) δ: 51.7, 55.7, 56.2 (2x), 61.2, 95.8, 99.7 (2x), 112.3, 114.1, 120.1, 124.1, 136.5, 136.9, 153.6 (2x), 155.8, 156.1, 160.3, 161.3. MS (ESI): $[M+1]^+$=388.0.

Ethyl 3-(3,4,5-trimethoxyphenylamino)-6-methoxybenzofuran-2-carboxylate (3h). Following general procedure B, the crude residue was purified by flash chromatography, using ethyl acetate:petroleum ether 3:7 (v:v) as eluent, to furnish **3h** as a yellow solid. Yield: 57%, mp 110-112 °C. ^{1}H-NMR ($CDCl_3$) δ: 1.45 (t, J=6.8 Hz, 3H), 3.78 (s, 6H), 3.80 (s, 3H), 3.86 (s, 3H), 4.43 (q, J=6.8 Hz, 2H), 6.42 (s, 2H), 6.70 (dd, J=8.8 and 2.2 Hz, 1H), 6.96 (d, J=2.2 Hz, 1H), 7.19 (d, J=8.8 Hz, 1H), 7.77 (s, 1H). ^{13}C-NMR ($CDCl_3$) δ: 14.7, 55.7, 56.2 (2x), 60.7, 61.2, 95.9, 99.5 (2x), 112.2, 113.1, 124.0, 125.9, 127.7, 136.6, 140.0, 153.6 (2x), 154.01, 156.2, 161.2. MS (ESI): $[M+1]^+$=402.2.

Methyl 3-(3,4,5-trimethoxyphenylamino)-7-methoxybenzofuran-2-carboxylate (3i). Following general procedure B, the crude residue was purified by flash chromatography, using ethyl acetate:petroleum ether 3:7 (v:v) as eluent, to furnish **3i** as a yellow solid. Yield: 68%, mp 177-179 °C. ^{1}H-NMR ($CDCl_3$) δ: 3.77 (s, 6H), 3.86 (s, 3H), 3.97 (s, 3H), 4.00 (s, 3H), 6.40 (s, 2H), 6.92 (m, 2H), 6.99 (m, 1H), 7.72 (s, 1H). ^{13}C-NMR ($CDCl_3$) δ: 51.7, 55.9, 56.1 (2x), 61.2, 99.5 (2x), 109.4, 115.4, 121.0, 122.5, 122.7, 124.5, 136.8, 139.1, 146.2, 147.1, 153.6 (2x), 162.3. MS (ESI): $[M+1]^+$=388.2.

Ethyl 3-(3,4,5-trimethoxyphenylamino)-7-methoxybenzofuran-2-carboxylate (3j). Following general procedure B, the crude residue was purified by flash chromatography, using ethyl acetate:petroleum ether 3:7 (v:v) as eluent, to furnish **3j** as a white solid. Yield: 73%, mp 184-186 °C. ^{1}H-NMR ($CDCl_3$) δ: 1.47 (t, J=7.0 Hz, 3H), 3.77 (s, 6H), 3.86 (s, 3H), 4.00 (s, 3H), 4.47 (q, J=7.0 Hz, 2H), 6.40 (s, 2H), 6.91 (m, 2H), 6.99 (m, 1H), 7.78 (s, 1H). ^{13}C-NMR ($CDCl_3$) δ: 14.7, 56.0, 56.1 (2x), 60.8, 61.2, 99.3 (2x), 106.5, 108.6, 109.3, 110.5, 115.4, 122.7, 124.5, 135.9, 137.0, 149.5, 153.6 (2x), 161.5. MS (ESI): $[M+1]^+$=402.2.

Methyl 3-(3,4,5-trimethoxyphenylamino)-7-ethoxybenzofuran-2-carboxylate (3k). Following general procedure B, the crude residue was purified by flash chromatography, using ethyl acetate:petroleum ether 3:7 (v:v) as eluent, to furnish **3k** as a yellow solid. Yield: 73%, mp 135-137 °C. ^{1}H-NMR ($CDCl_3$) δ: 1.52 (t, J=7.0 Hz, 3H), 3.77 (s, 6H), 3.86 (s, 3H), 3.98 (s, 3H), 4.24 (q, J=7.0 Hz, 2H), 6.40 (s, 2H), 6.88 (m, 2H), 6.97 (m, 1H), 7.71 (s, 1H). ^{13}C-NMR ($CDCl_3$) δ: 14.8, 51.6, 56.0 (2x), 61.1, 64.5, 99.3 (2x), 109.2, 110.4, 115.1, 118.2, 122.4, 122.6, 134.5, 136.8, 144.6, 145.4, 153.5 (2x), 162.2. MS (ESI): $[M+1]^+$=402.0.

Ethyl 3-(3,4,5-trimethoxyphenylamino)-7-ethoxybenzofuran-2-carboxylate (3l). Following general procedure B, the crude residue was purified by flash chromatography, using ethyl acetate:petroleum ether 3:7 (v:v) as eluent, to furnish **3l** as a yellow solid. Yield: 52%, mp 149-151 °C. ^{1}H-NMR ($CDCl_3$) δ: 1.41 (t, J=7.2 Hz, 3H), 1.53 (t, J=7.0 Hz, 3H), 3.77 (s, 6H), 3.85 (s, 3H), 4.24 (q, J=7.2 Hz, 2H), 4.44 (q, J=7.0 Hz, 2H), 6.40 (s, 2H), 6.90 (m, 2H), 6.97 (m, 1H), 7.75 (s, 1H). ^{13}C-NMR ($CDCl_3$) δ: 14.6, 14.8, 56.0 (2x), 60.7, 61.1, 64.5, 99.21 (2x), 108.8, 110.4, 115.1, 122.6, 123.5, 133.9, 134.1, 136.7, 136.9, 139.9, 153.5 (2x), 175.3. MS (ESI): $[M+1]^+$=416.2.

Molecular modeling. All molecular docking studies were performed on a MacPro dual 2.66GHz Xeon running Ubuntu 12.04. The simulations were carried out using two tubulin structures (http://www.rcsb.org/-PDB code: 1SA0 [10]; PDB code: 3HKC [174]). Hydrogen atoms were added to the protein, using the Protonate 3D routine of the Molecular Operating Environment (MOE) [150]. Ligand structures were built with MOE and minimized using the MMFF94x forcefield until a RMSD gradient of 0.05 kcal mol^{-1} $Å^{-1}$ was reached. The docking simulations were performed using PLANTS [151]. The docking results obtained using the two different protein structures were equivalent.

Antiproliferative assays. Human T-cell leukemia (Jurkat), human B-cell leukemia (RS4;11) and human promyelocytic leukemia (HL-60) cells were grown in RPMI-1640 medium, (Gibco, Milano, Italy). Breast adenocarcinoma (MCF-7), human non-small cell lung carcinoma (A549), human cervix carcinoma (HeLa) and human colon adenocarcinoma (HT-29) cells were grown in DMEM medium (Gibco, Milano, Italy). Both media were supplemented with 115 units/mL of penicillin G (Gibco, Milano, Italy), 115 μg/mL of streptomycin (Invitrogen, Milano, Italy) and 10% fetal bovine serum (Invitrogen, Milano, Italy). These cell lines were purchased from ATCC. Stock solutions (10 mM) of the different compounds were obtained by dissolving them in dimethyl sulfoxide (DMSO). Individual wells of a 96-well tissue culture microtiter plate were inoculated with 100 μL of complete medium containing $8x10^3$ cells. The plates were incubated at 37 °C in a humidified 5% CO_2 incubator for 18 h prior to the experiments. After medium removal, 100 μL of fresh medium containing the test compound at different concentrations was added to each well and incubated at 37 °C for 72 h. The percentage of DMSO in the medium never exceeded 0.25%. This was also the maximum DMSO concentration in all cell-based assays described below. Cell viability was assayed by the (3-(4,5-dimethylthiazol-2-yl)-2,5-diphenyl tetrazolium bromide test as previously described [170]. The IC_{50} was defined as the compound concentration required to inhibit cell proliferation by 50%, in comparison with cells treated with the maximum amount of DMSO, which was considered 100% viability.

PBLs from healthy donors were obtained by separation on Lymphoprep (Fresenius KABI Norge AS) gradient. After extensive washing, cells were resuspended (1.0×10^6 cells/mL) in RPMI-1640 with 10% fetal bovine serum and incubated overnight. For cytotoxicity evaluations in proliferating PBL cultures, non-adherent cells were resuspended at 5×10^5 cells/mL in growth medium containing 2.5 μg/mL PHA (Irvine Scientific). Different concentrations of the test compounds were added, and viability was determined 72 h later by the MTT test. For cytotoxicity evaluations in resting PBL cultures, non-adherent cells were resuspended (5×10^5 cells/mL) and treated for 72 h with the test compounds, as described above.

Effects on tubulin polymerization and on colchicine binding to tubulin. To evaluate the effect of the compounds on tubulin assembly *in vitro*[161], varying concentrations of compounds were preincubated with 10 μM bovine brain tubulin in glutamate buffer at 30 ˚C and then cooled to 0 ˚C. After addition of 0.4 mM GTP (final concentration), the mixtures were transferred to 0 °C cuvettes in a recording spectrophotometer and warmed to 30 °C. Tubulin assembly was followed turbidimetrically at 350 nm. The IC_{50} was defined as the compound concentration that inhibited the extent of assembly by 50% after a 20 min incubation. The ability of the test compounds to inhibit colchicine binding to tubulin was measured as described [163], except that the reaction mixtures contained 1 μM tubulin, 5 μM [^{3}H]colchicine and 5 μM test compound.

Flow cytometric analysis of cell cycle distribution. 5×10^5 HeLa or Jurkat cells were treated with different concentrations of the test compounds for 24 h. After the incubation period, the cells were collected, centrifuged, and fixed with ice-cold ethanol (70%). The cells were then treated with lysis buffer containing RNase A and 0.1% Triton X-100 and then stained with propidium iodide (PI). Samples were analyzed on a Cytomic FC500 flow cytometer (Beckman Coulter). DNA histograms were analyzed using MultiCycle for Windows (Phoenix Flow Systems).

Apoptosis assay. Cell death was determined by flow cytometry of cells double stained with annexin V/FITC and PI. The Coulter Cytomics FC500 (Beckman Coulter) was used to measure the surface exposure of phosphatidylserine on apoptotic cells according to the manufacturer's instructions (Annexin-V Fluos, Roche Diagnostics).

Assessment of mitochondrial changes. The mitochondrial membrane potential was measured with the lipophilic cationic dye JC-1 (Molecular Probes), as described [175]. The production of ROS was measured by flow cytometry using H_2DCFDA (Molecular Probes), as previously described [175].

Western blot analysis. HeLa cells were incubated in the presence of **3g** or **3h** and, after different times, were collected, centrifuged, and washed two times with ice cold phosphate buffered saline (PBS). The pellet was then resuspended in lysis buffer. After the cells were lysed on ice for 30 min, lysates were centrifuged at 15000 x g at 4 °C for 10 min. The protein concentration in the supernatant was determined using the BCA protein assay reagents (Pierce, Italy). Equal amounts of protein (10 μg) were resolved using sodium dodecyl sulfate-polyacrylamide gel electrophoresis (7.5-15% acrylamide gels) and transferred to PVDF Hybond-P membrane (GE Healthcare). Membranes were blocked with a 5% bovine serum albumin solution in Tween PBS, the membranes being gently rotated overnight at 4 °C. Membranes were then incubated with primary antibodies against Bcl-2, PARP, cleaved caspase-9, cdc25c (Cell Signaling), caspase-3 (Alexis), H2AX (Cell Signaling), p53 (Cell Signaling), cyclin B (Cell Signaling), p-cdc2^{Tyr15} (Cell Signaling), Mcl-1 (Cell Signaling), or β-actin (Sigma-Aldrich) for 2 h at room temperature. Membranes were next incubated with peroxidase labeled secondary antibodies for 60 min. All membranes were visualized using ECL Select (GE Healthcare) and exposed to Hyperfilm MP (GE Healthcare). To confirm equal protein loading, each membrane was stripped and reprobed with anti-β-actin antibody.

Evaluation of antivascular activity *in vitro.* HUVECs were prepared from human umbilical cord veins, as previously described [144]. The adherent cells were maintained in M200 medium supplemented with Low Serum Growth Supplement, containing fetal bovine serum, hydrocortisone, hEGF, bFGF, heparin, gentamycin/amphotericin (Life Technologies, Monza, Italy). Once confluent, the cells were detached by treatment with a trypsin–EDTA solution and used in experiments from the first to sixth passages.

The motility assay for HUVECs was based on "scratch" wounding of a confluent monolayer [176]. Briefly, HUVECs ($1x10^5$) were seeded onto 0.1% collagen type I (BD Biosciences, Italy)-coated six well plates in complete medium until a confluent monolayer was formed. The cells were wounded using a pipette tip, and wells were washed with PBS to remove the detached cells. Then, the cells were treated with the test compounds, and, at different times from the scratch, the cells were photographed under a light microscope. At all indicated time points, the wound width was measured in four areas and compared with the initial width.

Matrigel matrix (Basement Membrane Matrix, BD Biosciences, Italy) was kept at 4 °C for 3 h, when 230 μL of Matrigel solution was added to each well of a 24-well plate. After gelling at 37°C for 30 min, gels were overlaid with 500 μL of medium containing 6×10^4 HUVECs. The cells were incubated over Matrigel for 6 h to allow capillary tubes to form. Different concentrations of test compound were added in the cultures and incubated for different times, and the disappearance of existing vasculature was monitored and photographed (five fields for each well: the four quadrants and the center) at 10x magnification. Phase contrast images were recorded using a digital camera and saved as TIFF files. Image analysis was carried out using ImageJ image analysis software, and the following dimensional parameters (percent area covered by HUVECs and total length of

HUVECs network per field) and topological parameters (number of meshes and branching points per field) were estimated [143]. Values were expressed as percent change from control cultures grown with complete medium.

***In vivo* CAM assay in fertilized chicken eggs.** Alginate pellets containing 0.1-1.0 pmol per pellet of TR-644 or CA4 were grafted on the CAM of fertilized chicken eggs at day 11. After 72 h, new blood vessels converging toward the implant were counted at 5x magnification under a stereomicroscope.

Antivascular activity *in vivo***.** Six week old C57BL/6 mice (Charles River, Calco, Italy) were injected subcutaneously into the dorsolateral flank with 10^5 BL6-B16 murine melanoma cells in 200 µL of PBS. When tumor volume reached 300 mm^3, animals were treated intraperitoneally with **3g** (30 mg/kg) dissolved in DMSO (50 µl). Twenty-four hours later, tumors were harvested, embedded in OCT-compound (Bio-Optica) and immediately frozen in liquid nitrogen for immunohistochemical analysis, as previously described [144]. Excised tumors were cut with a cryostat into 4-5 µm sections. Immunohistochemistry was performed by staining samples with rat anti-mouse CD31 antibody (1:200; BD Biosciences) and biotinylated goat anti-rat secondary antibody (1:100; BD Biosciences). Quantification was performed by counting the number of CD31 positive vessels in 5 fields per section, using a 40x objective.

Antitumor activity *in vivo*. The *in vivo* cytotoxic activity of compound **3g** was investigated using a syngeneic murine hepatocellular carcinoma cell line (BNL 1ME A.7R.1) in Balb/c mice [145]. Male mice, 8 weeks old, were purchased from Harlan (S. Pietro al Natisone Udine, Italy), and tumors were induced by a subcutaneous injection in their dorsal region of 10^7 cells in 200 µL of sterile PBS. Animals were randomly divided into four groups, and, starting on the second day, the first group was daily dosed intraperitoneally with 7 µL/g of vehicle (0.9% NaCl containing 5% polyethylene glycol 400 and 0.5% Tween 80). Groups two and three were treated with compound **3g** at the doses of 5 or 10 mg/kg body weight, respectively. The fourth group received the reference compound CA-4P at 5 mg/kg body weight. Both compound **3g** and CA-4P were dissolved in vehicle. Tumor sizes were measured daily for 7 days using a pair of calipers. Tumor volume (V) was calculated by the rotational ellipsoid formula: $V = A \times B^2/2$, where A is the longer diameter (axial) and B is the shorter diameter (rotational). All experimental procedures followed guidelines recommended by the Institutional Animal Care and Use Committee of Padova University.

Statistical analysis. Unless indicated otherwise, results are presented as mean ± S.E.M. The differences between different treatments were analyzed using the two-sided Student's t test. P values less than 0.05 were considered significant

6. 1-(3',4',5'-Trimethoxyphenyl)-2-Aryl-1*H*-Imidazole, novel potent *in Vitro* and *in Vivo* Anticancer Agents

Due to the importance of the microtubule system of eukaryotic cells for a number of fundamental cellular processes, including mitosis, formation and maintenance of cell shape, regulation of motility, cell signalling, secretion and intracellular transport [14], the design of molecules that bind to tubulin and inhibit the formation of the mitotic spindle resulting in the block of mitosis, remains important strategy for the development of anticancer agents [6].

Combretastatin A-4 (CA-4, **1a**, Figure 1), isolated from the bark of the South African tree *Combretum caffrum,*[108] is one of the well-known natural molecules that strongly inhibits tubulin polymerization by binding to the colchicine site, and **1a** arrests cells in mitosis in nanomolar concentrations [177]. CA-4 shows potent cytotoxicity against a wide variety of human cancer cell lines at low to mid nanomolar concentrations, including those that are multidrug resistant [153]. The vascular disrupting properties of CA-4 and related compounds represent a new approach for cancer treatment [8]. The water-soluble disodium phosphate prodrug of CA-4 (named CA-4P, **1b**) has shown promising results in phase II and III clinical trials on advanced cancer based on the vascular shutdown mechanism of action [178], thus stimulating significant interest in a variety of CA-4 analogues [106].

Because of its activity and structural simplicity, a wide number of CA-4 analogues have been synthesized with modifications to ring A, ring B and the bridge [106].

Previous structure-activity relationship (SAR) studies have demonstrated that both the 3',4',5'-trimethoxy substitution pattern on the A-ring and the *cis*-olefin configuration at the bridge were fundamental requirements for optimal activity, while some B-ring structural modifications were tolerated by the target [106, 124d]. Structural modifications on the B-ring suggest that the 4'-methoxy group is crucial for cytotoxicity, while the 3'-hydroxy moiety is not necessary for potent activity [124d].

However, the *cis*-configuration of CA-4 is prone to isomerize to the thermodynamically more stable *trans*-form during storage and in the course of metabolism in liver microsomes, resulting in a dramatic decrease in antitumor activity. Thus, to retain the appropriate spatial arrangement of the two adjacent aryl groups required for potent bioactivity, chemically stable *cis*-restricted derivatives of CA-4 with general structure **2** were obtained by incorporating the olefinic double bond with vicinal diaryl-substituted five-member aromatic heterocyclic rings, such as pyrazole [179], imidazole [179, 180], thiazole [181], furazan (1,2,5-oxadiazole) [182], isoxazole [183], oxazole [179], 1,2,3-thiadiazole [184], isomeric triazole [185], tetrazole [148], furan [186] and thiophene [186].

In a previous study, Wang and co-workers reported the preparation of 1-(3',4',5'-trimethoxyphenyl)-2-(4'-*N*,*N*-dimethylaminophenyl)-1*H*-imidazole **3a**, with antiproliferative activity inferior to that of CA-4 against HCT-15 (human colon adenocarcinoma) and NCI-H460 (human lung large cell carcinoma) cancer cell lines, with IC_{50} values of 80 and 270 nM, respectively [179]. Moreover, this compound had activity considerably reduced (IC_{50}=35 μM) relative to the activity of CA-4 as an inhibitor of tubulin polymerization.

Among a small series of 1,2-diaryl-1*H*-imidazoles synthesized by Bellina et al. [180], the 1-(3',4',5'-trimethoxyphenyl)-2-substituted-1*H*-imidazole derivatives **3b** and **3c** showed different antiproliferative activity against the HCT-15 and NCI-H460 cell lines. The 4'-methoxyphenyl derivative **3b** showed moderate antiproliferative activity, with IC_{50} values of 1.1 and 1.6 μM against NCI-H460 and HCT-15 cells, respectively, while the 2'-naphthyl derivative **3c** had antiproliferative activity significantly higher than that of **3b**, with IC_{50} values of 57 and 51 nM, respectively. Compounds **3a-c** were regioselectively prepared by the direct C-2 arylation of 1-(3',4',5'-trimethoxy)-1*H*-imidazole with the required aryl iodide.

However this methodology was characterized from several limitations: a) high temperatures and long reaction times; b) the use of twice the stoichiometric amount of copper iodide; c) tedious chromatographic separations; and d) limited commercially available substrate.

In our efforts to discover new potent antimitotic agents in which the *cis*-olefinic bridge of CA-4 was replaced by the polar and ionizable imidazole ring, we developed an efficient and versatile convergent synthetic procedure for the preparation of a new series of 1-(3',4',5'-trimethoxyphenyl)-2-aryl-1*H*-imidazoles with general structure **4**, prepared starting with a 1-(3',4',5'-trimethoxyphenyl)-2-bromo-1*H*-imidazole intermediate.

Because it is well-known that the trimethoxyphenyl skeleton can be essential for maximal tubulin binding activity, all newly prepared compounds maintained one of the aryl groups as a 3',4',5'-trimethoxyphenyl moiety, identical with the A-ring of CA-4. Thus, once the 1-(3',4',5'-trimethoxyphenyl)-1*H*-imidazole motif was identified as the minimum structural requirement for activity, modifications that would further enhance the activity of previously published compounds **3a-c** were focused on varying the other aryl moiety at the 2-position of the imidazole skeleton. This ring corresponds to the B-ring of CA-4, and we replaceed the methoxy group at the *para*-position of the phenyl ring of compound **3b** with various electron-releasing (Me, Et, EtO, *n*-PrO, MeS, EtS) groups. The methoxy and ethoxy groups proved to be favorable for bioactivity, and, in the attempt to further increase antiproliferative activity, we introduced additional substituents (F, Cl, Me and MeO) at the *meta*-position of the *para*-methoxy/ethoxyphenyl ring.

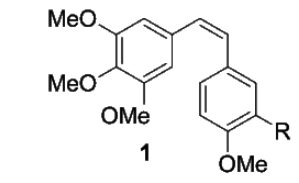

1

R=OH, Combretastatin A-4 (CA-4), **1a**
R=OPO_3Na_2, CA-4P, **1b**

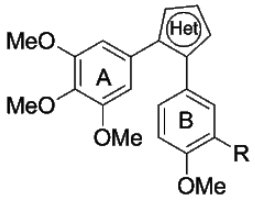

2

R=OH or NH_2
Het=imidazole; pyrazole; thiazole;oxazole; isoxazole; 1,2,3-thiadiazole; 1,2,3- or 1,2,4- or 1,3,4-triazole; 1,2,3,4-tetrazole, furazan, thiophene, furan.

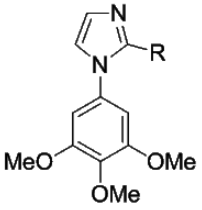

3a-c

3a, R=4'-$N(CH_3)_2$-C_6H_4
3b, R=4'-OMe-C_6H_4
3c, R=2'-naphthyl

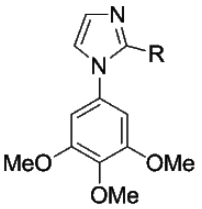

4a-q

4a, R=4'-Me-C_6H_4
4b, R=4'-Et-C_6H_4
4c, R=4'-SMe-C_6H_4
4d, R=4'-OMe-3'-F-C_6H_3
4e, R=4'-OMe-3'-Cl-C_6H_3
4f, R=4'-OMe-3'-Me-C_6H_3
4g, R=4'-Me-3'-OMe-C_6H_3
4h, R=4'-OMe-3',5'-2Me-C_6H_3
4i, R=3',4'-2OMe-C_6H_3
4j, R=4'-$OCF_3C_6H_4$
4k, R=4'-OEt-C_6H_4
4l, R=3'-OEt-C_6H_4
4m, R=2'-OEt-C_6H_4
4n, R=4'-OEt-3'-F-C_6H_3
4o, R=4'-OEt-3'-Cl-C_6H_3
4p, R=4'-SEt-C_6H_4
4q, R=4'-*n*-OPr-C_6H_4

Figure 1. Lead structures of tubulin polymerization inhibitors.

6.1 Chemistry

The synthetic protocol employed for the preparation of 1-(3',4',5'-trimethoxyphenyl)-2-aryl-1*H*-imidazoles with general structure **4** is shown in Figure 2. The 1-(3',4',5'-trimethoxyphenyl)-1*H*-imidazole **5** was obtained by a Ullmann-type direct *N*-arylation procedure of 1*H*-imidazole with 1-bromo-3,4,5-trimethoxybenzene in the presence of Cs_2CO_3 and a catalytic amount of CuI [187]. The regioselective electrophilic bromination at the C-2 position of compound **5** with *N*-bromosuccinimide (NBS) in refluxing acetonitrile led to the formation of the key intermediate **6**, which was subjected to Suzuki cross-coupling conditions in the presence of the appropriate arylboronic acid under heterogeneous conditions [$PdCl_2$(DPPF), CsF] in 1,4-dioxane at 65 °C, to furnish final compounds **4a-q**.

Figure 2. General synthetic procedure followed for the preparation of compounds 4a-q.

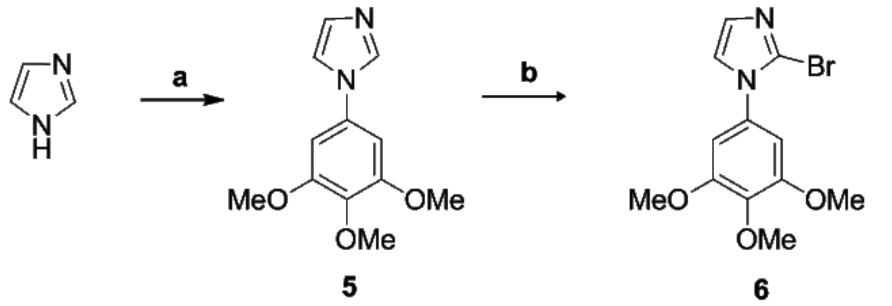

4a, R=4'-Me-C_6H_4
4b, R=4'-Et-C_6H_4
4c, R=4'-SMe-C_6H_4
4d, R=4'-OMe-3'-F-C_6H_3
4e, R=4'-OMe-3'-Cl-C_6H_3
4f, R=4'-OMe-3'-Me-C_6H_3
4g, R=4'-Me-3'-OMe-C_6H_3
4h, R=4'-OMe-3',5'-2Me-C_6H_3
4i, R=3',4'-2OMe-C_6H_3
4j, R=4'-CF_3O-C_6H_4
4k, R=4'-OEt-C_6H_4
4l, R=3'-OEt-C_6H_4
4m, R=2'-OEt-C_6H_4
4n, R=4'-OEt-3'-F-C_6H_3
4o, R=4'-OEt-3'-Cl-C_6H_3
4p, R=4'-SEt-C_6H_4
4q, R=4'-*n*-OPr-C_6H_4

Reagents. **a**: 1-bromo-3,4,5-trimethoxybenzene, Cs_2CO_3, CuI, DMF, 120 °C, 36 h; **b**: NBS, CH_3CN, rx; **c**: $PdCl_2$(DPPF), $ArB(OH)_2$, CsF, 1,4-dioxane, 65 °C.

6.2 Biological Results and Discussion

***In vitro* antiproliferative activities**.

The 1-(3',4',5'-trimethoxyphenyl)-2-aryl-1*H* imidazoles **4a-q** were evaluated for their antiproliferative activity against a panel of seven human tumor cell lines and compared with the known 4'-methoxyphenyl and 2'-naphthyl imidazole analogues **3b** and **3c**, respectively, as well as CA-4 (**1a**) as reference compounds. The data shown in Table 1 indicated the importance of substituents on the phenyl ring at the 2-position of the imidazole system for activity and selectivity against different cancer cell lines. Three of the synthesized compounds, corresponding to the 4'-OEt (**4k**), 3'-F-4'-OEt (**4n**) and 3'-Cl-4'-OEt (**4o**) phenyl analogues were significantly more active than the rest of the derivatives, with IC_{50} values of 1.8-34.7, 1.5-14.2 and 0.4-3.8 nM, respectively, in the seven cell lines, as compared with 1-3100, 210-5400 and 2-62.3 nM for the reference compounds **1a**, **3b** and **3c**. With average IC_{50} values of 7.1, 7.2 and 1.3 nM for **4k**, **4n** and **4o**, respectively, compound **4o** appeared to be the most active compound in the series (for **1a**, **3b** and **3c**, the average IC_{50} values were 523, 1712 and 15 nM, respectively). Derivatives **4k** and **4n** were 2-fold more active than the 2'-naphthyl derivative **3c**, while this latter compound was 12-fold less active than **4o**. In addition to these three highly active new compounds, the 3'-F-4'-OMe and 4'-*n*-OPr phenyl derivatives **4d** and **4q** were more active than CA-4 against HT-29, A549 and RS4;11 cells.

The replacement of the methoxy moiety of **3b** with a less electron-donating methyl group at the 4'-position of the phenyl ring (**4a**) caused a 2-12 fold drop in antiproliferative activity in six of the seven cancer cell lines relative to **3b** (the exception was the HL-60 cell line). The 4'-ethyl homologue **4b** was less active than its methyl counterpart **4a** against four of the seven cancer cell lines. Replacement of 4'-OMe group (**3b**) with a weak electron-releasing 4'-methylsulfanyl moiety (**4c**) reduced antiproliferative activity in five of the cancer cell lines relative to **3b**.

Relative to the activity of **3b**, the insertion of an additional electron-withdrawing or electron-releasing group on the 3'-position of the 4'-methoxyphenyl ring had varying effects on antiproliferative activity. The introduction of a strong electron-withdrawing fluorine, to furnish the 3'-F-4'-OMe phenyl derivative **4d**, resulted in increased antiproliferative activity in all seven cell lines. The introduction of chlorine or methyl substituents at the *meta*-position of **3b**, to yield **4e** and **4f**, respectively, generally resulted in lower activity relative to **3b**. By interchanging the positions of the methoxy and methyl groups in **4f**, we synthesized the corresponding 3'-OMe-4'-Me regioisomeric analogue **4g**, which showed substantially reduced activity relative to **4f**.

Adding an extra methoxy group, to furnish the 3',4'-diOMe derivative **4i**, led to a dramatic decrease in potency against all seven cell lines. A second methyl group, to furnish the 3',5'-diMe-4'-OMe derivative **4h**, also caused a substantial loss in activity relative to **4f**, as did the electron-withdrawing but bulky trifluoromethoxy moiety (compound **4j**).

We found that replacement of methoxy with ethoxy at the *para*-position of the phenyl ring, to furnish derivative **4k**, improved antiproliferative activity 57-933-fold relative to **3b**. Moving the ethoxy group from the *para*- to the *meta*- or *ortho*- position, to furnish isomeric derivatives **4l** and **4m**, respectively, led to a dramatic drop of potency as compared with **4k**. Lengthening the 4'-substituent further, to an isopropoxy group (**4q**) led to reduced activity relative to **4k** in five cell lines.

Table 1. In vitro cell growth inhibitory effects of compounds **3b**, **3c**, **4a-q** and CA-4 (**1a**)

Compd	IC50 (nM) a						
	HeLa	HT-29	A549	MCF-7	Jurkat	RS4;11	HL-60
3b	210±10.2	233±52	1013±104	230±55	133±31	5400±950	4766±120
3c	2.0±0.14	3.6±0.9	7.1±1.5	4.6±2.3	2.5±0.9	62.3±10.3	24.0±12.1
4a	1260±172	1915±354	4733±328	2800±721	760±136	>10000	2100±252
4b	1985±126	1400±200	7000±1153	2090±374	4569±758	5678±259	4800±451
4c	337±48	330±36	5600±352	1363±349.8	407±24	800±58	333±41
4d	51±6.5	112±15	121±56	74±17	90±23	217±46	29±9.5
4e	263±39	647±83	2600±422	666±231	365±25	715±148	453±14
4f	330±25	377±33	4717±509	509±25	136±38	475±106	413±27
4g	623±98	>10000	>10000	>10000	4933±536	2567±784	>10000
4h	9157±1593	>10000	>10000	>10000	>10000	>10000	3466±467
4i	>10000	>10000	>10000	>10000	>10000	>10000	3933±517
4j	>10000	>10000	>10000	>10000	6633±338	>10000	>10000
4k	3.7±0.12	1.8±0.8	1.9±1.0	1.5±0.2	1.2±0.5	34.7±0.0	4.8±1.9
4l	>10000	>10000	>10000	>10000	>10000	>10000	>10000
4m	>10000	>10000	>10000	>10000	>10000	>10000	>10000
4n	1.5±0.32	7.5±1.2	14±2.3	3.4±0.38	12±6.6	8.6±1.1	3.5±0.73
4o	3.8±0.7	0.4±0.06	0.57±0.17	0.7±0.06	0.9±0.2	1.2±0.7	1.8±0.6
4p	48±2.5	174±16	228±81	69±7.0	127±27	85±20	12±2.5
4q	2.9±0.8	15±1.3	63±18.1	1.7±0.6	42±3.9	91±8.9	63.0±17.6
CA-4	4±1	180±30	3100±100	5±0.6	0.8±0.2	370±100	1±0.2

[a]IC_{50}= compound concentration required to inhibit tumor cell proliferation by 50%. Data are expressed as the mean ± SE from the dose-response curves of at least three independent experiments

With the 4'-methoxy and 4'-ethoxy phenyl derivatives **3b** and **4k**, respectively, increasing the size of the 4' substituent modestly with either a by the replacement of the 4'-methylsulfanyl (**4c**) or a 4'-ethylsulfanyl (**4p**) substituent led to a loss in activity. Compound **4c** was less active than **3b** in five of the seven cell lines, and **4p** was less active than **4k** in all seven lines. Because the *para*-ethoxy phenyl moiety of **4k** was favorable for potency, we evaluated the effect on activity by the introduction of a fluorine or chlorine at the *meta*-position, resulting in the 3'-F-4'-OEt and 3'-Cl-4'-OEt phenyl derivatives **4n** and **4o**, respectively. With the fluorine substituent (**4n**), activity improved in only three of the cell lines, while, with the chloro substituent (**4o**), activity improved in six of the cell lines. Moreover, **4o** was more active than **4n** in all cell lines except the HeLa cells.

In contrast, the opposite effect was observed for the 3'-F-4'-OMe and 3'-Cl-4'-OMe phenyl derivatives **4d** and **4e**, respectively, where the fluoro derivative (**4d**) was more active than the chloro derivative (**4c**) in all seven cell lines. These results imply that the 3'-hydroxy-4'-ethoxyphenyl moiety of CA-4 (B-ring) can be replaced by a 3'-chloro-4'-ethoxyphenyl or a 3'-fluoro-4'ethoxyphenyl group.

Evaluation of cytotoxicity in human non-cancer cells.

To obtain a preliminary indication of the cytotoxic potential of these derivatives in normal human cells, one of the most active compounds (**4o**) was evaluated *in vitro* against peripheral blood lymphocytes (PBL) from healthy donors (Table 2). The compound showed an IC_{50} greater than 10 μM in quiescent lymphocytes, while in the presence of the mitogenic stimulus phytohematoaglutinin (PHA), the IC_{50} decreased to about 0.5 μM. This value was almost 600 times higher than that observed against the Jurkat lymphoblastic cell line. These results indicate that **4o** has a significant effect in rapidly proliferating cells but not in quiescent cells, as previously observed for other antimitotic derivatives developed by our group [188].

Table 2. Cytotoxicity of **4o** for human PBL

Cell line	IC_{50} (μM) [a]
$PBL_{resting}$ [b]	>10
PBL_{PHA} [c]	0.52±0.04

[a] Compound concentration required to reduce cell growth by 50%.

[b] PBL not stimulated with PHA.

[c] PBL stimulated with PHA.

Inhibition of tubulin polymerization and colchicine binding.

To investigate whether the antiproliferative activities of compounds **4k**, **4n-o** and **4q** derived from an interaction with tubulin, these agents were evaluated for their inhibition of tubulin polymerization and for effects on the binding of [^{3}H]colchicine to tubulin (Table 3) [161]. For comparison, CA-4 and **3c** were examined in contemporaneous experiments as reference compounds. All tested compounds strongly inhibited tubulin assembly, and the IC_{50} values of 0.63 and 0.57 μM obtained with **4k** and **4n**, respectively, were among the lowest ever observed in this assay and half that obtained in simultaneous experiments with CA-4 (IC_{50}=1.3 μM). While compounds **4k** and **4n** were the best inhibitors of tubulin assembly, about 1.5-fold more potent than **4o**, this latter compound, as described above, was more effective as an inhibitor of cell growth.

Compound **4o** was also 1.5-fold more potent than CA-4 as an inhibitor of tubulin assembly. Compound **4q** was as active as CA-4, while **3c** was less active. Compounds **4k**, **4n-o** and **4q** were from 1.2- to 3-fold more active than the 2-naphthyl derivative **3c** as inhibitors of tubulin assembly.

In the colchicine binding studies, compounds **4k**, **4n**, **4o** and **4q** strongly inhibited binding of colchicine to tubulin (over 50% inhibition when present in the reaction mixture at the same concentration as colchicine). Even when present at 1 μM, 20% of the colchicine concentration, **4k**, **4n** and **4o** inhibited colchicine binding by over 50%. None, however, was quite as potent as CA-4, which in these experiments inhibited colchicine binding by 99% at 5 μM and by 87% at 1 μM.

Compounds **4k**, **4n** and **4o** have activity superior to that of CA-4 as inhibitors of tubulin polymerization and are also highly active as inhibitors of colchicine binding to tubulin. While this group of compounds were all potent in the biological assays (inhibition of cell growth, tubulin assembly and colchicine binding), correlation between the three assay types was imperfect. In general, in these experiments, inhibition of [^{3}H]colchicine binding correlated more closely with inhibition of tubulin assembly than with antiproliferative activity. When comparing inhibition of tubulin polymerization versus antiproliferative activity, we found a positive correlation for most, but not all, of the active compounds. Thus, while compound **4o** was generally more active than **4k** and **4n** as antiproliferative agent, these latter two molecules were 1.5-fold more active than **4o** in the tubulin assembly assay. Also compound **4q** was as active as CA-4 as inhibitor of tubulin polymerization, although this derivative was less active in its effects on cell growth against Jurkat, RS4;11 and HL-60 cells.

Table 3. Inhibition of tubulin polymerization and colchicine binding by compounds **3c**, **4k**, **4n-o**, **4q** and CA-4

Compound	**Tubulin assembly[a]** IC_{50}**±S.D. (μM)**	**Colchicine binding[b] % inhibition ±S.D.**	
		5 μM drug	**1 μM drug**
3c	1.8±0	65±4	n.d.
4k	0.63±0	86±0.5	64±3
4n	0.57±0	89±0.3	71±3
4o	0.87±0	81±0.3	54±1
4q	1.4±0.1	67±0.5	n.d.
CA-4 (1a)	1.3±0.1	99±0.2	87±2

[a] Inhibition of tubulin polymerization. Tubulin was at 10 μM.

[b] Inhibition of [^{3}H]colchicine binding. Tubulin and colchicine were at 1 and 5 μM concentrations, respectively.

n.d.=not determined

6.3 Molecular modeling studies.

A series of molecular docking simulations were performed on compounds **3c**, **4k**, **4n**, **4o** and **4q** to investigate their binding mode in the colchicine site of tubulin.

The proposed binding mode for all the derivatives was consistent with that previously reported for the triazole family [188], and it was very similar to that observed for the co-crystallized DAMA-colchicine. With all derivatives, the trimethoxyphenyl ring is in proximity to βCys241. The phenyl ring with different substituents occupied a small hydrophobic subpocket (Figure 3), making potential hydrophobic interactions with the surrounding amino acids (e.g., βMet259). Tubulin polymerization inhibition appeared to be influenced by the substituent on the phenyl ring, but the explanation for this observation was not evident from the docking studies.

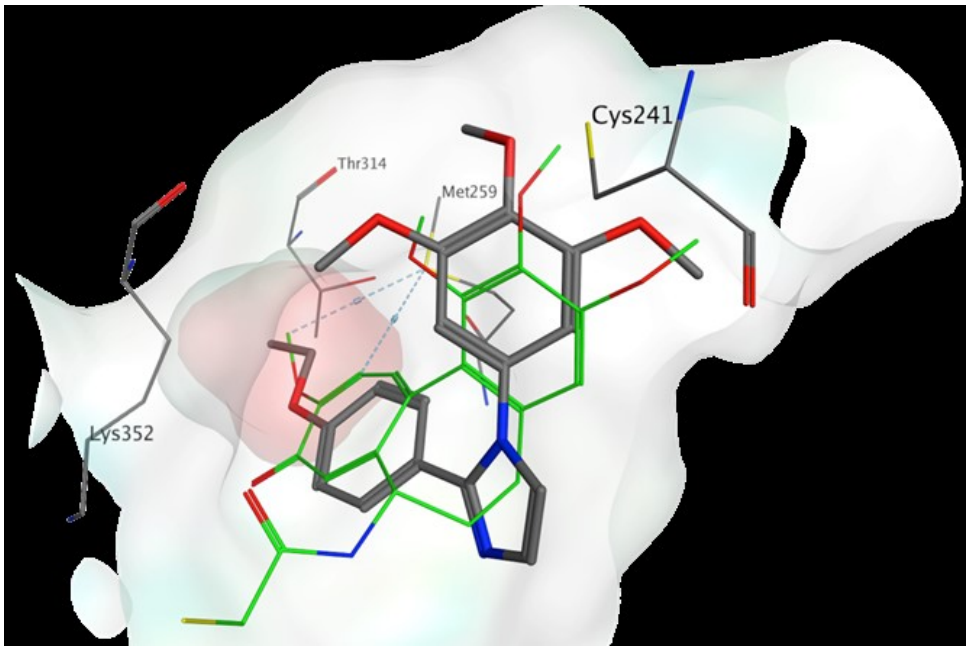

Figure 3. Proposed binding for compound **4k** (in grey) in the colchicine site. Co-crystallized DAMA-colchicine is shown in green. The hydrophobic subpocket is highlighted with a red surface.

For this reason, we investigated the role of the substituent on the phenyl through a series of molecular dynamic (MD) simulations on selected compounds (**3c**, **4k**, **4o**, **4q**). We then evaluated the compounds relative binding free energies ($\Delta G_{binding}$) using the Prime/MM-GBSA based calculation method [189, 190]. After an initial 3 ns of equilibration, all the protein-ligand systems reached stability. We therefore considered only the remaining 7 ns of the simulation in our analysis.

The predicted binding mode, and, in particular, the position of the trimethoxyphenyl ring, was maintained by all derivatives during the entire simulation, confirming the reliability of the docking studies. The lowest calculated $\Delta G_{binding}$ was found for compound **4k**, the ethoxy derivative, whereas derivative **3c** showed the highest estimated energy value. The linear relationship between the estimated $\Delta G_{binding}$ and the IC_{50} for inhibition of tubulin polymerization was found for all the simulations performed (Table 4).

The hydrophobic subpocket can accommodate the different substituted phenyl rings, but only the ethoxy derivatives (**4k** and **4o**) were able to fit into it properly, thereby conferring stability to the protein-ligand system and yielding low energy values.

The insertion of a second, more hindered, substituent at position 3, as in compound **4o** (4-ethoxy-3-Cl derivative), slightly reduced the potency of inhibition of tubulin polymerization, and, indeed, a higher calculated $\Delta G_{binding}$ value was found. Larger groups in a *para* position, such as in the

propoxy (**4q**) and the naphtyl (**3c**) derivatives, could be accommodated in the pocket but with a higher protein-ligand $\Delta G_{binding}$, which is consistent with the reduced capacity of these compounds to inhibit tubulin polymerization.

Table 4. Calculated ligand-interaction energies for the compounds analyzed by Molecular Dynamics and inhibition of tubulin polymerization IC_{50} values.

Compound	$\Delta G_{binding}$ (kJ/mol)[a]	IC_{50} (μM)
3c	-71.543	1.8
4k	-98.652	0.63
4o	-89.506	0.87
4q	-78.846	1.4

[a] Average values of $\Delta G_{binding}$ calculated excluding the first 3ns of MD in which the protein-ligand system reached stability.

The MD simulation results confirmed the importance of the trimethoxyphenyl ring for the interaction of the ligand with the colchicine site. Furthermore, the binding energy calculations confirmed the importance of the hydrophobic sub-pocket in the colchicine site and provide a plausible explanation for the different activities observed with the different substituents on the phenyl ring.

6.4 Compound 4o induced mitotic arrest of the cell cycle.

The effects of a 24 h treatment with different concentrations of **4o** on cell cycle progression in Jurkat, and HeLa cells were determined by flow cytometry, following propidium iodide (PI) staining of the cells (Figure 4, Panels A and B). The compound caused a significant G2/M arrest in a concentration-dependent manner in the cell lines tested, with a rise in G2/M cells occurring at a concentration as low as 25 nM, while at the highest concentration more than 80% of the cells were arrested in G2/M in HeLa cells.

In the HeLa cells, the G2/M block was accompanied by a significant reduction of both G1 and S phase cells. In order to determine whether **4o** was able to block cells at the mitotic phase (M), cells were stained with an immunofluorescent antibody to p-histone H3, a well known mitotic marker [191], as well as PI, and analyzed by flow cytometry.

As shown in Figure 4 (Panel C), in which representative histograms are presented, Hela cells arrested in M phase by treatment with **4o** are readily distinguished from G2 cells by the higher level of p-histone H3.

In particular, treatment with **4o** induced an increase in the percentage of mitotic cells from the 2% observed in untreated cells to about 30% with both 50 and 100 nM **4o** at 24 h (Figure 4, Panel D).

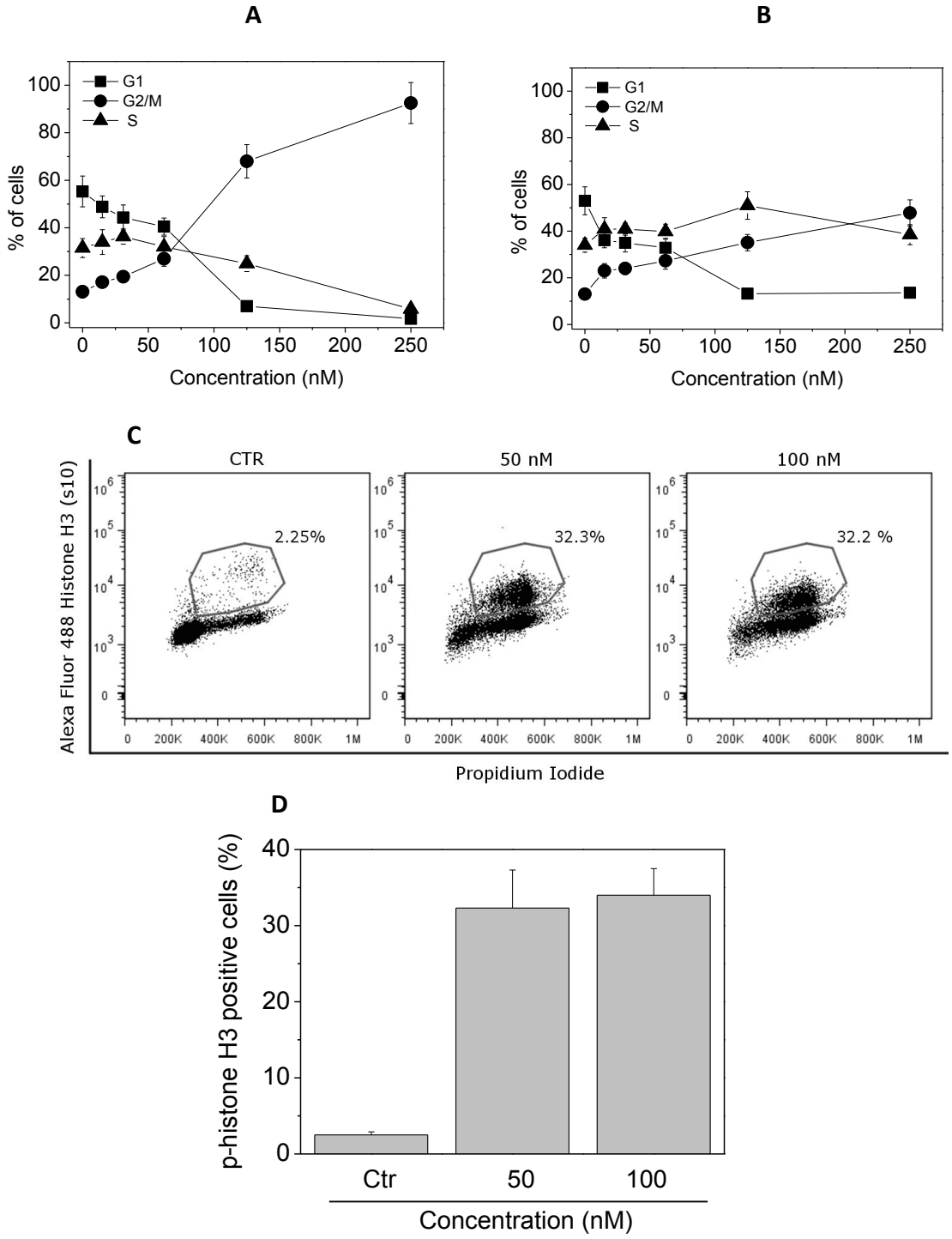

Figure 4. Percentage of cells in each phase of the cell cycle in HeLa (Panel A) and Jurkat cells (Panel B) treated with compound 4o at the indicated concentrations for 24 h. Cells were fixed and labeled with PI and analyzed by flow cytometry as described in the Experimental Section. Data are represented as mean±SEM of three independent experiments. Representative histograms of mitotic cells with phosphorylated histone-H3 (Panel C) and quantitative analysis (Panel D) after treatment with 4o at the indicated concentrations in HeLa cells. Data are represented as mean±SEM of two independent experiments

Compound 4o induced alteration in both cell cycle and spindle assembly checkpoint proteins.

We investigated the effects of **4o** on the expression of several proteins involved in regulation of the cell cycle and in spindle assembly. Cyclin B1 is involved in the G2 to M transition as a complex with cdc2, and the activation of the cdc2/cyclin B1 complex through cdc25c-dependent dephosphorylation of phospho-cdc2 and phosphorylation of cyclin B1 triggers cells to enter mitosis [165,192]. As shown in Figure 5 (Panel A) a marked increase of cyclin B1 was observed after a 24 h treatment with 50 nM **4o**. At this time point, total cdc25c expression was strongly reduced, while more slowly migrating forms of cdc25c appeared both at 24 and 48 h, indicating changes in the phosphorylation state of this protein. Moreover, in good agreement, the expression of phosphorylated cdc2 strongly decreased after both 24 and 48 h treatments. Thus, our results indicate that cdc2/cyclin B1 complexes failed to be activated, preventing cells from exiting mitosis, which would eventually lead to apoptotic cell death.

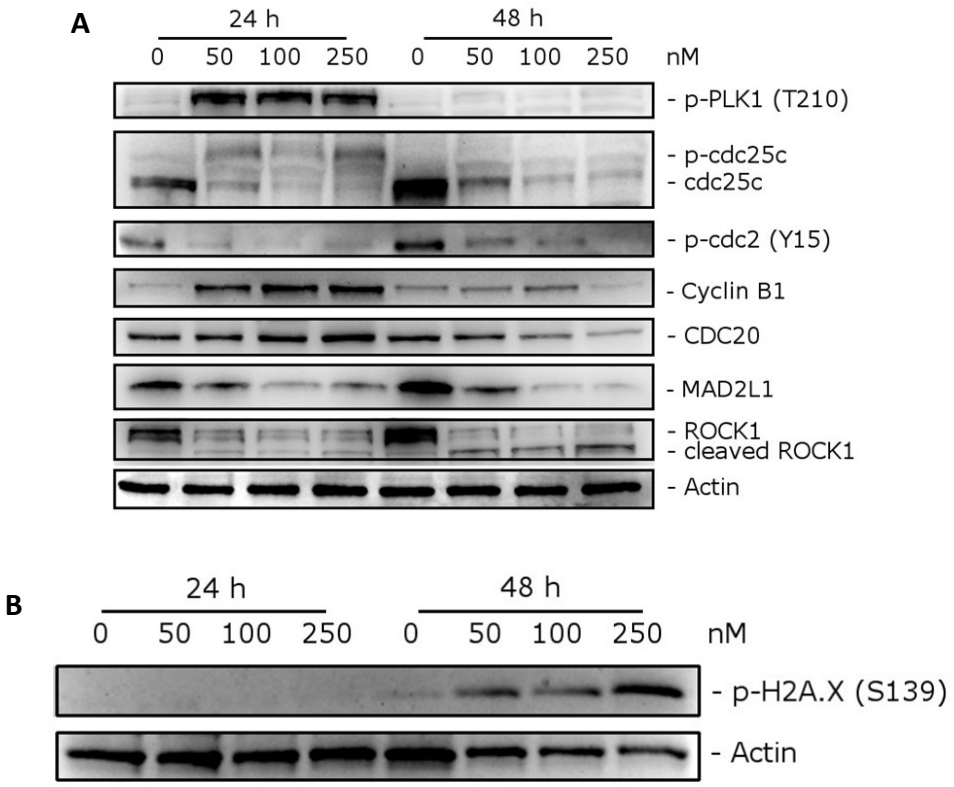

Figure 5. Effect of 4o on cell cycle and spindle assembly checkpoint proteins (Panel A), and expression of p-H2A.X^{Ser139}(Panel B). HeLa cells were treated for 24 or 48 h with the indicated concentrations of 4o. The cells were harvested and lysed for detection of the expression of the indicated protein by western blot analysis. To confirm equal protein loading, each membrane was stripped and reprobed with anti-β-actin antibody

Formation of the microtubular mitotic spindle is of fundamental importance in mitosis for the correct segregation of chromosomes and a proper mitotic exit. Thus, we also examined the levels of several proteins regulating spindle assembly, such as PLK1, MAD2, cdc20 and ROCK1 [193]. First, we examined if **4o** inhibited the anaphase promoting complex/cyclosome (APC/C). To do this, we analyzed the expression of cdc20, which is associated with its inhibitory protein MAD2. Although the level of cdc20 remained unaffected after a 24 h treatment, MAD2 expression was substantially decreased at both 24 and 48 h, suggesting that **4o** would inhibit the formation of the MAD2/cdc20 checkpoint complex and thus impair the spindle checkpoint machinery.

Polo-like kinase (PLK1) has many functions in mitosis, including centrosome maturation, kinetochore-spindle attachment, chromosome segregation and cytokinesis [194]. Moreover, PLK1 can phosphorylate and activate cdc25c [195]. We observed a marked increase in the

phosphorylation of PLK1 after a 24 h treatment with **4o**, when mitotic arrest occurred, and then this effect disappeared at 48 h. This was probably due to DNA damage, which reduces PLK1 phosphorylation [196]. Indeed, examining the expression of phosphorylated histone H2A.X at Ser139 (γH2A.X), a well known marker of DNA damage [197], we observed (Figure 5, Panel B) a remarkable increase of the phosphorylation of γH2A.X, suggesting that DNA damage occur following treatment with **4o**.

ROCK1 (Rho-associated coiled-coil kinase1) is a protein involved in proper microtubule dynamics and centrosome integrity during mitosis, and, in addition, it is also involved in cell motility and contractility [198]. It is also interesting to note that ROCK1 is cleaved by caspase-3 during apoptosis and is responsible for the formation of apoptotic blebs [199]. As shown in Figure 5 (Panel A), western blot analysis showed that cleaved bands of ROCK1 appeared after a 48 h treatment with **4o**. Altogether, our results showed that **4o** induced cell cycle arrest at the mitotic phase and impaired spindle checkpoint functions that ultimately should lead to apoptosis.

6.5 Compound 4o induced apoptosis.

To evaluate the induction of apoptosis by compound **4o** in two cell lines (HeLa and Jurkat), we used an annexin-V/PI assay. Dual staining for annexin-V and with PI permits discrimination between live cells (annexin-V^-/PI^-), early apoptotic cells (annexin-V^+/PI^-), late apoptotic cells (annexin-V^+/PI^+) and necrotic cells (annexin-V^-/PI^+). As shown in Figure 6, both HeLa (Panels A, B) and Jurkat (Panels C, D) cells treated with **4o** showed a significant accumulation of annexin-V positive cells after a 24 h treatment at the lowest concentration used (50 nM). The percentage of apoptotic cells increased further after 48 h in comparison with untreated Jurkat cells, whereas, in the HeLa cells, we observed a marked increase of necrotic cells, indicating that the compound at this time induced massive cellular death.

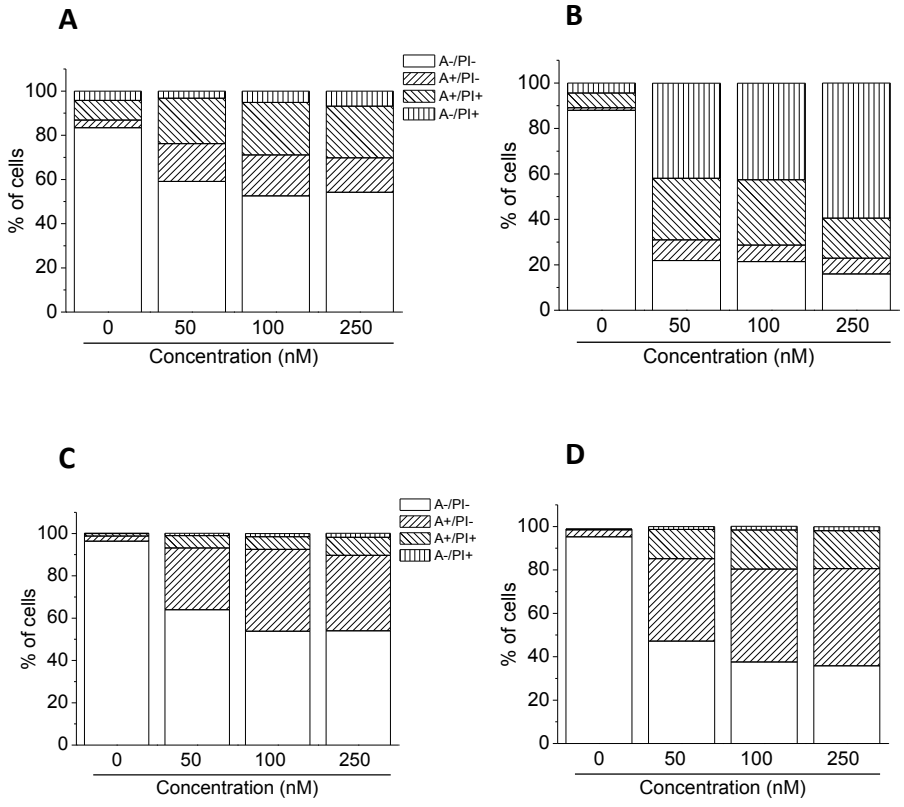

Figure 6. Flow cytometric analysis of apoptotic cells after treatment of HeLa (Panels A and B) and Jurkat (Panels C and D) cells with 4o at the indicated concentrations after incubation for 24 (Panels A and C) or 48 h (Panels B and D). The cells were harvested and labeled with annexin-V-FITC and PI and analyzed by flow cytometry**.**

Compound 4o induced apoptosis through the mitochondrial pathway.

Mitochondria play an essential role in the propagation of apoptosis [200]. It is well established that, at an early stage, apoptotic stimuli alter the mitochondrial transmembrane potential ($\Delta\psi_{mt}$). $\Delta\psi_{mt}$ was monitored by the fluorescence of the dye JC-1. In normal conditions (high $\Delta\psi_{mt}$), JC-1 displays a red fluorescence (590 nm). Both HeLa and Jurkat cells treated with **4o** (50, 100 and 250 nM) exhibited a remarkable increase in the percentage of cells with low $\Delta\psi_{mt}$ (Figure 7, Panels A, C). This occurred in a time- and concentration-dependent fashion, and, in both cell lines, a significant increase was observed after a 6 h treatment. The disruption of $\Delta\psi_{mt}$ is associated with the appearance of annexin-V positivity in the treated cells when they are in an early apoptotic stage. In fact, the dissipation of $\Delta\psi_{mt}$ is characteristic of apoptosis and has been observed with both microtubule stabilizing and destabilizing agents, including CA-4, in different cell types [188, 201, 202].

It is also well known that dissipation of mitochondrial potential is associated with mitochondrial production of ROS [203]. Superoxide anion is produced by mitochondria due to a shift from the normal 4-electron reduction of O_2 to a 1-electron reduction when cytochrome *c* is released from mitochondria upon apoptosis. Therefore, we investigated whether ROS production increased after treatment with compound **4o**. We utilized the dye 2,7-dichlorodihydrofluorescein diacetate (H_2-DCFDA), which is oxidized to the fluorescent compound dichlorofluorescein (DCF) upon ROS induction.

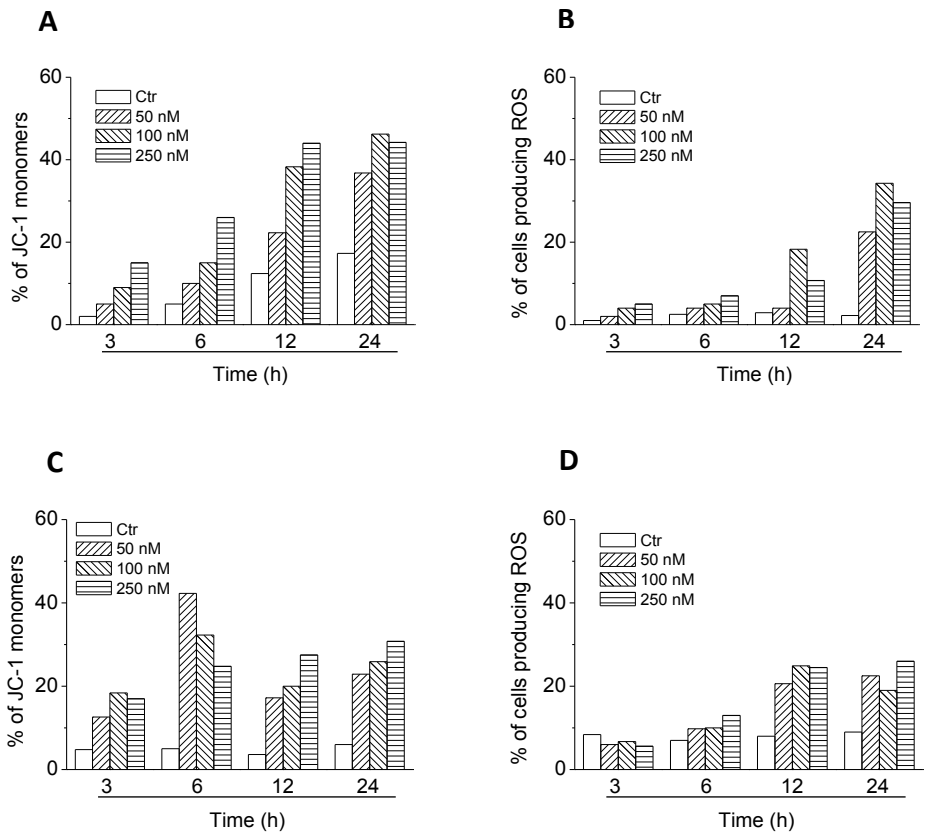

Figure 7. Assessment of mitochondrial membrane potential ($\Delta\psi_{mt}$) and production of ROS after treatment of HeLa (Panels A and B) or Jurkat (Panels C and D) cells with compound 4o. Cells were treated with the indicated concentration of compound for 24 or 48 h and then stained with the fluorescent probe JC-1 for analysis of mitochondrial potential or H_2-DCFDA for the evaluation of ROS levels. Cells were then analyzed by flow cytometry as described in the experimental section

The results shown in Figure 7 (Panels B and D), indicate that **4o** induced the production of large amounts of ROS in comparison with control cells, in both Jurkat and HeLa cells, and this agrees with the dissipation of $\Delta\psi_{mt}$ described above. In fact, the ROS increase was detected only after mitochondrial depolarization, indicating that the ROS are produced as a consequence of mitochondrial damage.

Compound 4o induced caspase-dependent apoptosis.

To further study the apoptotic process induced by **4o**, we analyzed by immunoblot the expression of caspase-3 and its substrate poly(ADP)ribose polymerase (PARP). We treated HeLa cells with different concentrations (50, 100 and 250 nM) of compound **4o** for 24 and 48 h. As shown in Figure 8, we observed an activation of the effector caspase-3, as demonstrated by the appearance of its cleaved fragments, in particular after the 48 h treatment. In good agreement, we observed the cleavage of PARP, a caspase-3 substrate. PARP cleavage is a typical marker of apoptosis. It is worth noting to note that these effects occurred at all the **4o** concentrations used.

We also investigated the expression of two anti-apoptotic proteins, specifically Mcl-1 and Bcl-2. Mcl-1 is a member of the Bcl-2 family of anti-apoptotic proteins. Mcl-1 is overexpressed in many cancers and has been implicated in the apoptotic response to multiple stimuli. Recently, it was reported that sensitivity to antimitotic drugs is regulated by Mcl-1 levels [204]. Bcl-2 controls the apoptotic machinery and plays a central role in mitochondrial membrane permeabilization [205]. As shown in Figure 8, both Mcl-1 and Bcl-2 undergo a dramatic decrease after a 24 h treatment at all compound concentrations examined, indicating that **4o** induced downregulation of these proteins to disable their anti-apoptotic function.

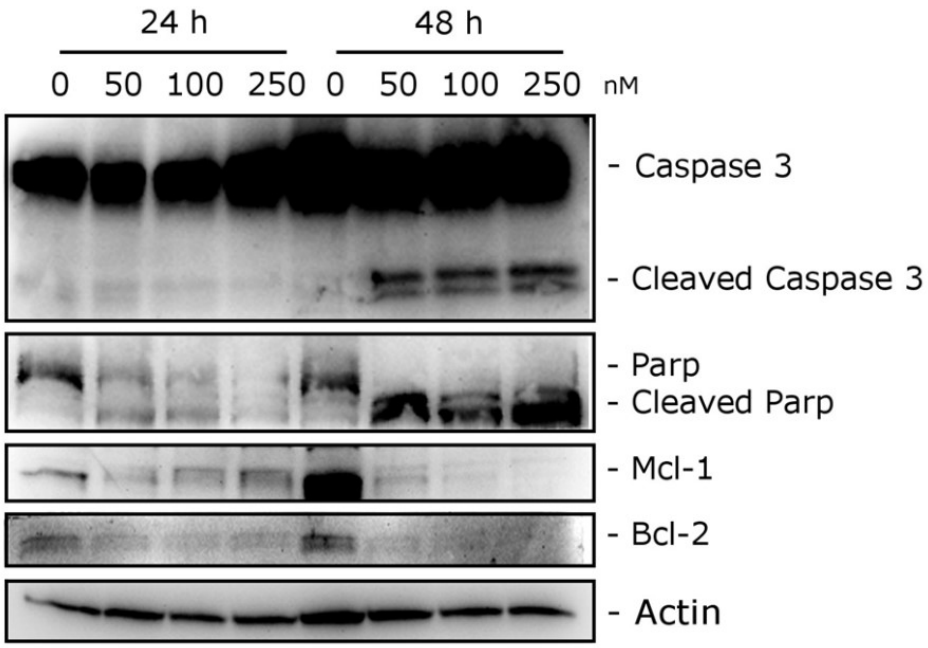

Figure 8. Western blot analysis of caspase-3, PARP, Bcl-2 and Mcl-1 after treatment of HeLa cells with 4o at the indicated concentrations and for the indicated times. To confirm equal protein loading, each membrane was stripped and reprobed with anti-β-actin antibody

6.6 Tumor growth was significantly inhibited by 4o in a mouse allograft tumor model.

To elucidate its antitumor effect *in vivo*, **4o** was administered by the intraperitoneal route each other day, at different doses (1, 3 and 7.5 mg/kg) in a tumor model developed in mice [206]. As reference compound, CA-4P (**1b**) was used at 30 mg/kg. The BL6-B16 mouse melanoma cell line, injected subcutaneously in syngeneic C57/BL6 mice, is able to proliferate and generate tumor masses.

As shown in Figure 9, after six days of treatment (doses administered on days 9, 11 and 14), **4o** was able to significantly reduce tumor burden in a dose-dependent manner, even at the lowest dose tested (1 mg/kg). We observed a reduction of tumor mass of 26.0, 32.2 and 45.8% at the doses of 1, 3.5 and 7.5 mg/kg, respectively. The reference compound CA-4P (**1b**) at 30 mg/kg induced only a 26.5% reduction of tumor mass. Notably, the *in vivo* efficacy clearly indicates an increased antitumor efficacy of **4o** as compared with CA-4P. Even at the highest dose, **4o** did not present any sign of toxicity and did not cause a decrease in animal body weight (data not shown)

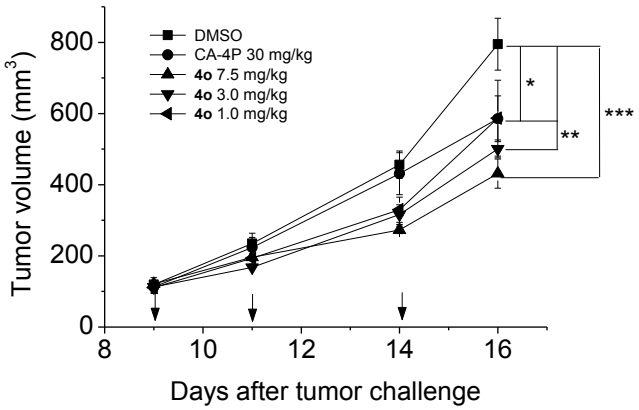

Figure 9. Inhibition of mouse allograft growth *in vivo* by compound 4o. Male C57BL/6 mice were injected subcutaneously at their dorsal region with 10^7 BL6-B16 murine melanoma cells. Tumor-bearing mice were administered the vehicle, as control, or 1, 3 or 7.5 mg/kg of 4o or CA-4P as reference compound at the dose of 30 mg/kg. Injections were given intraperitoneally at the days indicated by the arrows. Data are presented as mean ± SEM of tumor volume at each time point for 5 animals per group. *p<0.05, **p<0.01 ***p<0.001 *vs*. control.

6.7 Conclusions

The structural refinement of compounds **3a-c** led to the discovery of a novel series of synthetic inhibitors of tubulin polymerization with general structure **4**, based on the 1-(3',4',5'-trimethoxyphenyl)-2-aryl-1*H*-imidazole molecular skeleton. These molecules were prepared in mild conditions *via* a palladium-catalyzed Suzuki cross coupling reaction, starting from an easily accessible key intermediate, 1-(3',4',5'-trimethoxyphenyl)-2-bromo-1*H*-imidazole. We retained the 3',4',5'-trimethoxyphenyl moiety as ring A throughout the present investigation, and a SAR was elucidated with several variations of substituents on the second aryl ring at the 2-position of the imidazole nucleus.

The best results for inhibition of antiproliferative activity was obtained with 4'-OEt, 3'-F-4'-OEt and 3'-Cl-4'-OEt phenyl analogues **4k**, **4n** and **4o**, respectively. In particular, compound **4o** exhibited the strongest growth inhibitory activity in the series, with IC_{50} values ranging from 0.4 to 3.8 nM against seven cancer cells lines. Compound **4o** was also more potent as an antiproliferative agent than the corresponding 1-(3',4',5'-trimethoxyphenyl)-5-(3'-chloro-4'-ethoxyphenyl)triazole previously published by us [185]. This compound has IC_{50} values ranging from 3 to 20 nM, as compared with the range 0.4-3.8 nM obtained with **4o** in the same seven cell lines.

Importantly, **4o** showed very low cytotoxicity in proliferating lymphocytes obtained from healthy volunteers, and it was practically ineffective in resting lymphocytes, suggesting that it preferentially was toxic in proliferating cells as compared with quiescent cells. In this context, further experiments will be needed to better characterize the toxicological profile of **4o**.

Compound **4o** strongly inhibited tubulin assembly, exhibiting activity about 1.5-2-fold greater than that of CA-4, while in the colchicine binding studies, it was slightly less potent than CA-4, which, in these experiments, inhibited colchicine binding by 99%. These results were supported by a series of molecular docking and MD simulations.

The pharmacological investigation demonstrated that **4o** was able to induce mitotic arrest even at low concentrations and caused a strong impairment of both cell cycle and spindle assembly checkpoint proteins. This ultimately led to a massive apoptosis that employed the mitochondrial pathway, as demonstrated by the induction of mitochondrial depolarization. Finally, this excellent pharmacological profile was confirmed through *in vivo* experiments in which the compound was very effective in reducing tumor mass at doses 3-30 times lower in comparison with CA-4P. In short, our findings demonstrate that **4o** is a promising antitumor compound that warrants further preclinical development.

6.8 Experimental Section

Chemistry. Materials and methods.

^{1}H NMR and ^{13}C NMR spectra were recorded in $CDCl_3$ solution with a Varian Mercury Plus 400 spectrometer at 400 MHz and 100 MHz, respectively. Peak positions are given in parts per million (δ) downfield from tetramethylsilane as internal standard, and J values are given in hertz. Positive-ion electrospray ionization (ESI) mass spectra were measured on a double-focusing Finnigan MAT 95 instrument with BE geometry. Melting points (mp) were determined on a Buchi-Tottoli apparatus and are uncorrected. The purity of tested compounds was determined by combustion elemental analyses conducted by the Microanalytical Laboratory of the Chemistry Department of the University of Ferrara with a Yanagimoto MT-5 CHN recorder elemental analyzer. All tested compounds yielded data consistent with a purity of at least 95% as compared with the theoretical values. TLC was performed on silica gel (precoated F_{254} Merck plates), and compounds were visualized with aqueous $KMnO_4$. Flash column chromatography was performed using 230-400 mesh silica gel and the indicated solvent system. Organic solutions were dried over anhydrous Na_2SO_4. All commercial chemicals and solvents were reagent grade and were used without further treatment.

Preparation of 1-(3',4',5'-trimethoxyphenyl)-1*H*-imidazole (5). A stirred suspension of imidazole (954 mg, 14 mmol), 5-bromo-1,2,3-trimethoxybenzene (2.47 g., 10 mmol), CuI (381 mg, 2 mmol) and Cs_2CO_3 (6.5 g., 20 mmol) in DMF (20 mL) was evacuated and then back filled with Ar, and this sequence was repeated three times. The reaction mixture was stirred for 30 min at room temperature and then heated at 120 °C under Ar for 36 h. After being cooled at room temperature, the reaction mixture was diluted with a mixture of EtOAc (40 mL) and water (10 mL). The organic phase was washed with water (3 x 10 mL), brine (10 mL), dried over Na_2SO_4 and concentrated under reduced pressure. The residue was purified by column chromatography on silica gel (EtOAc-MeOH 9-1 v/v as eluent) to furnish the desired product **5** as a yellow oil. Yield: 77%. ^{1}H-NMR (400 MHz, *d*$_6$-DMSO) δ: 3.67 (s, 3H), 3.86 (s, 6H), 6.92 (s, 2H), 7.08 (m, 1H), 7.74 (m, 1H), 8.23 (m, 1H). MS (ESI): $[M+1]^+$=235.2.

Preparation of 2-bromo-1-(3',4',5'-trimethoxyphenyl)-1*H*-imidazole (6). To a solution of 1-(3',4',5'-trimethoxyphenyl)-1*H*-imidazole (1.17 g, 5 mmol) in dry acetonitrile (50 mL), NBS (980 mg, 5.5 mmol) was added, and the reaction mixture was heated at reflux for 3 h. The solvent was removed under reduced pressure, and the residue was diluted with EtOAc (30 mL), and the EtOAc solution was washed with 5% aqueous $NaHCO_3$ (10 mL), water (10 mL), and brine (50 mL), dried (Na_2SO_4) and concentrated. The residue was purified by column chromatography on silica gel (EtOAc-petroleum ether 6-4 v/v), to furnish the desired product **6** as a pink solid, mp 145-147 °C.

Yield: 81%. ^{1}H-NMR (400 MHz, *d*$_6$-DMSO) δ: 3.71 (s, 3H), 3.81 (s, 6H), 6.80 (s, 2H), 7.09 (d, J=1.4 Hz, 1H), 7.56 (d, J=1.4 Hz, 1H). ^{13}C-NMR (100 MHz, *d*$_6$-DMSO) δ: 56.16 (2C), 60.01, 104.18 (2C), 118.67, 124.82, 129.48 (2C), 132.28, 137.42, 152.90. MS (ESI): $[M+1]^+$=312.9 and 314.8.

General procedure A for the synthesis of compounds 4a-q. A stirred solution of **6** (156 mg, 0.5 mmol) and the appropriate phenylboronic acid (0.75 mmol) in 1,4-dioxane (6 mL containing 1 drop of water) was degassed under a stream of N_2 over 10 min, then treated with $PdCl_2$(DPPF) (41 mg, 0.05 mmol) and CsF (190 mg, 1.25 mmol). The reaction mixture was heated under N_2 at 45 °C for 30 min, then at 75 °C for 5 h. The reaction mixture was cooled to ambient temperature, diluted with CH_2Cl_2 (10 mL), filtered through a pad of celite and evaporated *in vacuo*. The residue was dissolved with CH_2Cl_2 (15 mL), and the resultant solution was washed sequentially with water (5 mL) and brine (5 mL). The organic layer was dried and evaporated, and the residue was purified by flash chromatography on silica gel.

1-(3',4',5'-Trimethoxyphenyl)-2-*p*-tolyl-1*H*-imidazole (4a). Following general procedure A, the crude residue was purified by flash chromatography, using EtOAc-petroleum ether 7-3 as eluent, to furnish **4a** as a white solid, mp 142-144 °C. Yield: 62%. ^{1}H-NMR (400 MHz, $CDCl_3$) δ: 2.32 (s, 3H), 3.72 (s, 6H), 3.87 (s, 3H), 6.42 (s, 2H), 7.05 (d, J=8.2 Hz, 2H), 7.12 (d, J=1.2 Hz, 1H), 7.21 (d, J=1.2 Hz, 1H), 7.30 (d, J=8.8 Hz, 2H). ^{13}C-NMR (100 MHz, $CDCl_3$) δ: 21.32, 56.31 (2C), 61.14, 103.63 (2C), 122.69, 127.53, 128.37 (2C), 128.85, 128.94 (2C), 134.40, 136.53, 138.34, 146.92, 153.58 (2C). MS (ESI): $[M+1]^+$=325.2.

2-(4'-Ethylphenyl)-1-(3',4',5'-trimethoxyphenyl)-1*H*-imidazole (4b). Following general procedure A, the crude residue was purified by flash chromatography, using ethyl acetate as eluent, to furnish **4b** as a white solid, mp 130-132 °C. Yield: 59%. ^{1}H-NMR (400 MHz, $CDCl_3$) δ: 1.20 (t, J=7.6 Hz, 3H), 2.61 (q, J=7.5 Hz, 2H), 3.71 (s, 6H), 3.87 (s, 3H), 6.40 (s, 2H), 7.11 (d, J=8.4 Hz, 2H), 7.14 (d, J=1.2 Hz, 1H), 7.23 (d, J=1.2 Hz, 1H), 7.31 (d, J=8.4 Hz, 2H). ^{13}C-NMR (100 MHz, $CDCl_3$) δ: 15.48, 28.70, 56.30 (2C), 61.14, 103.59 (2C), 122.45, 127.06, 127.41, 127.73 (2C), 128.52, 128.68, 134.18, 134.62, 144.88, 146.86, 153.57 (2C). MS (ESI): $[M+1]^+$=339.0.

1-(3',4',5'-Trimethoxyphenyl)-2-(4'-(methylthio)phenyl)-1*H*-imidazole (4c). Following general procedure A, the crude residue was purified by flash chromatography, using ethyl acetate-petroleum ether 8-2 as eluent, to furnish **4c** as a white solid, mp 158-160 °C. Yield: 79%. ^{1}H-NMR (400 MHz, $CDCl_3$) δ: 2.45 (s, 3H), 3.73 (s, 6H), 3.88 (s, 3H), 6.43 (s, 2H), 7.12 (m, 3H), 7.21 (d, J=1.2 Hz, 1H), 7.34 (d, J=8.8 Hz, 2H). ^{13}C-NMR (100 MHz, $CDCl_3$) δ: 15.39, 56.37 (2C), 61.15, 103.64 (2C), 122.96, 125.72 (2C), 126.88, 128.67 (2C), 128.98, 134.29, 137.90, 139.26, 146.34, 153.69 (2C). MS (ESI): $[M+1]^+$=357.2.

2-(3'-Fluoro-4'-methoxyphenyl)-1-(3',4',5'-trimethoxyphenyl)-1*H*-imidazole (4d). Following general procedure A, the crude residue was purified by flash chromatography, using ethyl acetate as eluent, to furnish **4d** as a white solid, mp 126-127 °C. Yield: 68%. ^{1}H-NMR (400 MHz, $CDCl_3$) δ: 3.76 (s, 6H), 3.87 (s, 3H), 3.89 (s, 3H), 6.44 (s, 2H), 6.84 (t, J=8.4 Hz, 1H), 7.11 (d, J=1.2 Hz, 1H), 7.13 (m, 1H), 7.20 (d, J=1.2 Hz, 1H), 7.22 (dd, J=12.8 and 2.4 Hz, 1H). ^{13}C-NMR (100 MHz, $CDCl_3$) δ: 56.38 (2C), 60.46, 61.17, 103.68 (2C), 112.83, 116.12, 123.00, 123.47, 124.46, 128.91, 134.10, 138.05, 145.49, 147.92, 153.05, 153.74 (2C). MS (ESI): $[M+1]^+$=359.2.

2-(3'-Chloro-4'-methoxyphenyl)-1-(3',4',5'-trimethoxyphenyl)-1*H*-imidazole (4e). Following general procedure A, the crude residue was purified by flash chromatography, using ethyl acetate-petroleum ether 7-3 as eluent, to furnish **4e** as a white solid, mp 176-178 °C. Yield: 54%. ^{1}H-NMR (400 MHz, $CDCl_3$) δ: 3.75 (s, 6H), 3.86 (s, 3H), 3.89 (s, 3H), 6.44 (s, 2H), 6.79 (d, J=8.6 Hz, 1H), 7.12 (d, J=1.2 Hz, 1H), 7.22 (m, 2H), 7.56 (d, J=2.2 Hz, 1H). ^{13}C-NMR (100 MHz, $CDCl_3$) δ: 56.24, 56.47 (2C), 61.21, 103.76 (2C), 111.53, 122.41, 122.97, 127.23, 127.92, 128.40, 129.12, 130.35, 133.86, 145.19, 153.81 (2C), 155.26. MS (ESI): $[M+1]^+$=375.2.

2-(4'-Methoxy-3'-methylphenyl)-1-(3',4',5'-trimethoxyphenyl)-1*H*-imidazole (4f). Following general procedure A, the crude residue was purified by flash chromatography, using EtOAc-petroleum ether 7-3 as eluent, to furnish **4f** as a white solid, mp 128-130 °C. Yield: 62%. ^{1}H-NMR (400 MHz, $CDCl_3$) δ: 2.13 (s, 3H), 3.72 (s, 6H), 3.78 (s, 3H), 3.86 (s, 3H), 6.43 (s, 2H), 6.64 (d, J=8.4 Hz, 1H), 7.05 (dd, J=8.4 and 2.4 Hz, 1H), 7.09 (d, J=1.2 Hz, 1H), 7.17 (d, J=1.2 Hz, 1H), 7.36 (d, J=2.4 Hz, 1H). ^{13}C-NMR (100 MHz, $CDCl_3$) δ: 16.19, 55.36, 56.35 (2C), 61.14, 103.75 (2C), 109.33, 122.41, 126.50, 127.03, 128.65 (2C), 130.97, 134.56, 137.76, 146.92, 153.55 (2C), 157.96. MS (ESI): $[M+1]^+$=355.2.

2-(4'-Methyl-3'-methoxyphenyl)-1-(3',4',5'-trimethoxyphenyl)-1*H*-imidazole (4g). Following general procedure A, the crude residue was purified by flash chromatography, using EtOAc-petroleum ether 7-3 as eluent, to furnish **4g** as a colorless oil. Yield: 59%. ^{1}H-NMR (400 MHz, $CDCl_3$) δ: 2.17 (s, 3H), 3.70 (s, 3H), 3.74 (s, 6H), 3.87 (s, 3H), 6.46 (s, 2H), 6.79 (dd, J=7.6 and 1.6 Hz, 1H), 6.97 (d, J=7.6 Hz, 1H), 7.05 (d, J=1.2 Hz, 1H), 7.12 (d, J=1.2 Hz, 1H), 7.21 (d, J=1.6 Hz, 1H). ^{13}C-NMR (100 MHz, $CDCl_3$) δ: 16.12, 55.27, 56.39 (2C), 61.12, 103.84 (2C), 110.04, 120.32, 122.87, 127.13, 128.77, 122.87, 130.27, 134.54, 137.87, 146.91, 153.63 (2C), 157.43. MS (ESI): $[M+1]^+$=355.1.

2-(4'-Methoxy-3',5'-dimethylphenyl)-1-(3',4',5'-trimethoxyphenyl)-1*H*-imidazole (4h) Following general procedure A, the crude residue was purified by flash chromatography, using EtOAc-petroleum ether 7-3 as eluent, to furnish **4h** as a white solid, mp 153-155 °C. Yield: 52%. ^{1}H-NMR (400 MHz, $CDCl_3$) δ: 2.17 (s, 6H), 3.68 (s, 3H), 3.72 (s, 6H), 3.87 (s, 3H), 6.43 (s, 2H), 7.07 (s, 2H), 7.11 (d, J=1.2 Hz, 1H), 7.18 (d, J=1.2 Hz, 1H). ^{13}C-NMR (100 MHz, $CDCl_3$) δ: 16.13 (2C), 56.39 (2C), 59.77, 61.17, 103.74 (2C), 122.47, 125.84, 128.79 (2C), 129.12 (2C), 130.66, 124.37, 137.87, 146.69, 153.54 (2C), 157.32. MS (ESI): $[M+1]^+$=369.2..

1-(3',4',5'-Trimethoxyphenyl)-2-(3',4'-dimethoxyphenyl)-1*H*-imidazole (4i). Following general procedure A, the crude residue was purified by flash chromatography, using EtOAc as eluent, to furnish **4i** as a yellow oil. Yield: 63%. ^{1}H-NMR (400 MHz, $CDCl_3$) δ: 3.74 (s, 6H), 3.75 (s, 3H), 3.78 (s, 3H), 3.87 (s, 3H), 6.46 (s, 2H), 6.70 (d, J=8.6 Hz, 1H), 6.85 (dd, J=8.6 and 1.8 Hz, 1H), 7.12 (m, 2H), 7.20 (d, J=1.2 Hz, 1H). ^{13}C-NMR (100 MHz, $CDCl_3$) δ: 55.81, 55.91, 56.40, 61.12, 103.83 (2C), 110.62, 111.52, 121.11, 122.74, 123.03, 126.50, 128.72, 134.54, 137.88, 146.61, 148.56, 152.21, 153.67 (2C). MS (ESI): $[M+1]^+$=371.2.

1-(3',4',5'-Trimethoxyphenyl)-2-(4'-(trifluoromethoxy)phenyl)-1*H*-imidazole (4j). Following general procedure A, the crude residue was purified by flash chromatography, using EtOAc-petroleum ether 6-4 as eluent, to furnish **4j** as a yellow solid, mp 125-127 °C. Yield: 68%. ^{1}H-NMR (400 MHz, $CDCl_3$) δ: 3.72 (s, 6H), 3.88 (s, 3H), 6.41 (s, 2H), 7.12 (dd, J=8.8 and 2.8 Hz, 2H), 7.16 (d, J=1.2 Hz, 1H), 7.23 (d, J=1.2 Hz, 1H), 7.46 (dd, J=8.8 and 2.8 Hz, 2H). ^{13}C-NMR (100 MHz, $CDCl_3$) δ: 56.32 (2C), 61.16, 103.53 (2C), 118.2 (q, J=262 Hz), 120.67 (2C), 123.26, 129.09, 129.22, 129.94 (2C), 133.92, 138.04, 145.38, 149.19, 153.78 (2C). MS (ESI): $[M+1]^+$=395.1.

2-(4'-Ethoxyphenyl)-1-(3',4',5'-trimethoxyphenyl)-1*H*-imidazole (4k). Following general procedure A, the crude residue was purified by flash chromatography, using EtOAc as eluent, to furnish **4k** as a white solid, mp 132-134 °C. Yield: 64%. ^{1}H-NMR (400 MHz, $CDCl_3$) δ: 1.40 (t, J=7.0 Hz, 3H), 3.73 (s, 6H), 3.88 (s, 3H), 4.03 (q, J=7.0 Hz, 2H), 6.43 (s, 2H), 6.77 (d, J=8.8 Hz, 2H), 7.11 (d, J=1.2 Hz, 1H), 7.20 (d, J=1.2 Hz, 1H), 7.33 (d, J=8.8 Hz, 2H). ^{13}C-NMR (100 MHz, $CDCl_3$) δ: 14.83, 56.35 (2C), 61.14, 63.52, 103.68 (2C), 114.21 (2C), 122.46, 122.85, 128.75, 129.89 (2C), 134.46, 137.80, 146.82, 153.63 (2C), 159.15. MS (ESI): $[M+1]^+$=355.2.

2-(3'-Ethoxyphenyl)-1-(3',4',5'-trimethoxyphenyl)-1*H*-imidazole (4l). Following general procedure A, the crude residue was purified by flash chromatography, using EtOAc as eluent, to furnish **4l** as a white solid, mp 121-122 °C. Yield: 73%. ^{1}H-NMR (400 MHz, $CDCl_3$) δ: 1.42 (t, J=7.2 Hz, 3H), 3.75 (s, 6H), 3.89 (s, 3H), 4.12 (q, J=7.2 Hz, 2H), 6.44 (s, 2H), 6.76 (dd, J=8.4 and 1.2 Hz, 1H), 6.91 (dt, J=8.2 and 1.4 Hz, 1H), 7.05 (d, J=1.2 Hz, 1H), 7.11 (m, 1H), 7.15 (d, J=1.2 Hz, 1H), 7.23 (d, J=1.2 Hz, 1H). ^{13}C-NMR (100 MHz, $CDCl_3$) δ: 15.36, 56.37 (2C), 60.48, 63.12,

103.69 (2C), 113.79 (2C), 115.83, 120.85, 122.95, 128.96, 129.23, 131.51, 134.34, 146.68, 153.65 (2C), 158.76. MS (ESI): $[M+1]^+$=355.1.

2-(2'-Ethoxyphenyl)-1-(3',4',5'-trimethoxyphenyl)-1*H*-imidazole (4m). Following general procedure A, the crude residue was purified by flash chromatography, using EtOAc as eluent, to furnish **4m** as a white solid, mp 130-132 °C. Yield: 64%. ^{1}H-NMR (400 MHz, $CDCl_3$) δ: 1.00 (t, J=7.2 Hz, 3H), 3.63 (s, 6H), 3.64 (q, J=7.2 Hz, 2H), 3.79 (s, 3H), 6.32 (s, 2H), 6.71 (d, J=8.4 Hz, 1H), 6.99 (dt, J=7.6 and 0.8 Hz, 1H), 7.23 (d, J=1.2 Hz, 1H), 7.26 (d, J=1.2 Hz, 1H), 7.31 (dt, J=8.4 and 1.6 Hz, 1H), 7.5 (dd, J=7.6 and 2.0 Hz, 1H). ^{13}C-NMR (100 MHz, $CDCl_3$) δ: 14.44, 56.03 (2C), 61.01, 63.24, 101.26 (2C), 111.44 (2C), 120.62, 120.70, 129.07, 130.70, 132.14, 134.84, 136.73, 145.00, 153.09 (2C), 156.45. MS (ESI): $[M+1]^+$=355.3.

2-(3'-Fluoro-4'-ethoxyphenyl)-1-(3',4',5'-trimethoxyphenyl)-1*H*-imidazole (4n). Following general procedure A, the crude residue was purified by flash chromatography, using EtOAc as eluent, to furnish **4n** as a cream colored solid, mp 127-129 °C. Yield 58%. ^{1}H-NMR (400 MHz, $CDCl_3$) δ: 1.46 (t, J=6.8 Hz, 3H), 3.82 (s, 6H), 3.94 (s, 3H), 4.12 (q, J=6.8 Hz, 2H), 6.54 (s, 2H), 7.07 (m, 2H), 7.36 (dd, J=7.8 and 2.2 Hz, 1H), 7.82 (m, 2H). ^{13}C-NMR (100 MHz, $CDCl_3$) δ: 14.60, 56.90 (2C), 61.30, 65.13, 103.78 (2C), 105.36, 113.61, 114.79, 116.27, 120.24, 123.58, 127.50, 130.39, 140.03, 150.51, 152.98 (2C), 154.51. MS (ESI): $[M+1]^+$=373.4.

2-(3'-Chloro-4'-ethoxyphenyl)-1-(3',4',5'-trimethoxyphenyl)-1*H*-imidazole (4o). Following general procedure A, the crude residue was purified by flash chromatography, using EtOAc as eluent, to furnish **4o** as a white solid, mp 140-142 °C. Yield: 67%. ^{1}H-NMR (400 MHz, $CDCl_3$) δ: 1.45 (t, J=7.2 Hz, 3H), 3.75 (s, 6H), 3.88 (s, 3H), 4.07 (q, J=7.2 Hz, 2H), 6.44 (s, 2H), 6.76 (d, J=8.4 Hz, 1H), 7.12 (d, J=1.2 Hz, 1H), 7.18 (dd, J=8.4 and 2.2 Hz, 1H), 7.20 (d, J=1.2 Hz, 1H), 7.57 (d, J=2.2 Hz, 1H). ^{13}C-NMR (100 MHz, $CDCl_3$) δ: 14.69, 56.43 (2C), 61.19, 64.77, 103.72 (2C), 112.50, 122.62, 122.89, 123.57, 127.69, 128.93, 130.37, 134.11, 138.06, 145.42, 153.73 (2C), 154.54. MS (ESI): $[M+1]^+$=389.0.

2-(4'-(Ethylthio)phenyl)-1-(3',4',5'-trimethoxyphenyl)-1*H*-imidazole (4p). Following general procedure A, the crude residue was purified by flash chromatography, using EtOAc-petroleum ether 8-2 as eluent, to furnish **4p** as a white solid, mp 143-145 °C. Yield: 72%. ^{1}H-NMR (400 MHz, $CDCl_3$) δ: 1.29 (t, J=7.4 Hz, 3H), 2.92 (q, J=7.4 Hz, 2H), 3.73 (s, 6H), 3.88 (s, 3H), 6.43 (s, 2H), 7.13 (d, J=1.2 Hz, 1H), 7.17 (d, J=8.6 Hz, 2H), 7.22 (d, J=1.2 Hz, 1H), 7.33 (d, J=8.6 Hz, 2H). ^{13}C-NMR (100 MHz, $CDCl_3$) δ: 14.23, 27.08, 56.35 (2C), 61.17, 63.52, 103.62 (2C), 122.97, 127.54, 127.88 (2C), 128.74 (2C), 129.05, 134.27, 137.60, 146.33, 153.70 (2C). MS (ESI): $[M+1]^+$=371.2.

1-(3',4',5'-Trimethoxyphenyl)-2-(4'-*n*-propoxyphenyl)-1*H*-imidazole (4q). Following general procedure A, the crude residue was purified by flash chromatography, using EtOAc as eluent, to furnish **4q** as a yellow oil. Yield: 69%. ^{1}H-NMR (400 MHz, $CDCl_3$) δ: 1.01 (t, J=7.4 Hz, 3H), 1.80 (m, 2H), 3.73 (s, 6H), 3.86 (s, 3H), 3.89 (q, J=7.4 Hz, 2H), 6.43 (s, 2H), 6.76 (d, J=8.8 Hz, 2H), 7.11 (d, J=1.2 Hz, 1H), 7.29 (d, J=1.2 Hz, 1H), 7.36 (d, J=8.8 Hz, 2H). ^{13}C-NMR (100 MHz, $CDCl_3$) δ: 10.54, 22.59, 56.33 (2C), 61.14, 69.56, 103.63 (2C), 114.21 (2C), 122.46, 122.74, 128.71, 129.85 (2C), 134.46, 137.73, 146.82, 153.61 (2C), 159.32. MS (ESI): $[M+1]^+$=369.2.

Molecular Modeling.

All molecular modeling studies were performed on a MacPro dual 2.66 GHz Xeon running Ubuntu 14.04. The tubulin structure was downloaded from the PDB data bank (http://www.rcsb.org/; PDB code 1SA0) [10]. Hydrogen atoms were added to the protein, using the Protonate 3D routine of the Molecular Operating Environment (MOE) [150]. Ligand structures were built with MOE and minimized using the MMFF94x force field until a RMSD gradient of 0.05 kcal mol−1 Å−1 was reached. The docking simulations were performed using PLANTS [151].

Molecular dynamics were performed using the Desmond package for MD simulation [207]: OPLS-AA force field in explicit solvent, employing the TIP3 water model was used. The initial coordinates for MD simulation were taken from the best docking experiment results for each single ligand. A cubic water box was used for the solvation of the system, ensuring a buffer distance of approximately 11 Å between each box side and the complex atoms. The system was neutralized adding 30 sodium counter ions. The systems were minimized and pre-equilibrated using the default relaxation routine implemented in Desmond. A 10 ns MD simulation was performed, during which the equation of motion were integrated using a 2 fs time step in the NPT ensemble, with temperature (300 K) and pressure (1 atm) constant. All other parameters were set using the Desmond default values. Data were collected every 4 ps (energy) and every 16 ps (trajectory). Visualization of protein-ligand complexes and MD trajectory analysis were carried out using Maestro, and the RMSD analyses were performed using the Simulation Event Analysis tool of Desmond. Protein-ligand frames, for each compound simulation, were extracted every 0.3 ns (total of 24 frames for each single ligand) from the last 7 ns of simulation. For each frame, the ligand and the protein were separated and their $\Delta G_{binding}$ was calculated using the MM/GBSA method as implemented in the Prime module from Maestro using the default settings. Finally, the average of the computed $\Delta G_{binding}$ for the 24 frames were plotted against the experimental data (Fig S2).

Biological assays

Materials and Methods

Cell growth conditions and antiproliferative assay.

Human T-cell leukemia (CCRF-CEM and Jurkat) and human B-cell leukemia (SEM) cells were grown in RPMI-1640 medium (Gibco, Milano, Italy). Breast adenocarcinoma (MCF7), human cervix carcinoma (HeLa), and human colon adenocarcinoma (HT-29) cells were grown in DMEM medium (Gibco, Milano, Italy), all supplemented with 115 units/mL penicillin G (Gibco, Milano, Italy), 115 μg/mL streptomycin (Invitrogen, Milano, Italy), and 10% fetal bovine serum (Invitrogen, Milano, Italy). Stock solutions (10 mM) of the different compounds were obtained by dissolving them in dimethyl sulfoxide (DMSO). Individual wells of a 96-well tissue culture microtiter plate were inoculated with 100 µL of complete medium containing 8×10^3 cells. The plates were incubated at 37 °C in a humidified 5% CO_2 incubator for 18 h prior to the experiments. After medium removal, 100 µL of fresh medium containing the test compound at different concentrations was added to each well in triplicate and incubated at 37 °C for 72 h. The percentage of DMSO in the medium never exceeded 0.25%. This was also the maximum DMSO concentration in all cell-based assays described below. Cell viability was assayed by the (3-(4,5-dimethylthiazol-2-yl)-2,5-diphenyltetrazolium bromide test as previously described [188]. The IC_{50} was defined as the compound concentration required to inhibit cell proliferation by 50%, in comparison with cells treated with the maximum amount of DMSO (0.25%) and considered as 100% viability. PBL from healthy donors were obtained by separation on a Lymphoprep (Fresenius KABI Norge AS) gradient. After extensive washing, cells were resuspended (1.0×10^6 cells/mL) in RPMI-1640 with 10% fetal bovine serum and incubated overnight. For cytotoxicity evaluations in proliferating PBL cultures, non-adherent cells were resuspended at 5×10^5 cells/mL in growth medium, containing 2.5 μg/mL PHA (Irvine Scientific). Different concentrations of the test compounds were added, and viability was determined 72 h later by the MTT test. For cytotoxicity evaluations in resting

PBL cultures, non-adherent cells were resuspended (5 x 10^5 cells/mL) and treated for 72 h with the test compounds, as described above.

Effects on tubulin polymerization and on colchicine binding to tubulin.

To evaluate the effect of the compounds on tubulin assembly *in vitro* [149a], varying concentrations of compounds were preincubated with 10 μM bovine brain tubulin in glutamate buffer at 30 ˚C and then cooled to 0 ˚C. After addition of 0.4 mM GTP (final concentration), the mixtures were transferred to 0 °C cuvettes in a recording spectrophotometer equipped with an electronic temperature controller and warmed to 30 °C. Tubulin assembly was followed turbidimetrically at 350 nm. The IC_{50} was defined as the compound concentration that inhibited the extent of assembly by 50% after a 20 min incubation. The ability of the test compounds to inhibit colchicine binding to tubulin was measured as described [149a], except that the reaction mixtures contained 1 μM tubulin, 5 μM [^{3}H]colchicine and 1 or 5 μM test compound.

Flow Cytometric Analysis of Cell Cycle Distribution.

5×10^5 HeLa or Jurkat cells were treated with different concentrations of the test compounds for 24 h. After the incubation period, the cells were collected, centrifuged, and fixed with ice-cold ethanol (70%). The cells were then treated with lysis buffer containing RNase A and 0.1% Triton X-100 and then stained with PI. Samples were analyzed on a Cytomic FC500 flow cytometer (Beckman Coulter). DNA histograms were analyzed using MultiCycle for Windows (Phoenix Flow Systems).

Apoptosis Assay.

Cell death was determined by flow cytometry of cells double stained with annexin V/FITC and PI. The Coulter Cytomics FC500 (Beckman Coulter) was used to measure the surface exposure of phosphatidyl serine on apoptotic cells according to the manufacturer's instructions (Annexin-V Fluos, Roche Diagnostics).

Western Blot Analysis.

HeLa cells were incubated in the presence of **4o** and, after different times, were collected, centrifuged, and washed two times with ice cold phosphate buffered saline (PBS). The pellet was then resuspended in lysis buffer. After the cells were lysed on ice for 30 min, lysates were centrifuged at 15000 x g at 4 °C for 10 min. The protein concentration in the supernatant was determined using the BCA protein assay reagents (Pierce, Italy). Equal amounts of protein (10 μg) were resolved using sodium dodecyl sulfate-polyacrylamide gel electrophoresis (SDS-PAGE) (Criterion Precast, BioRad, Italy) and transferred to a PVDF Hybond-P membrane (GE Healthcare). Membranes were blocked with a bovine serum albumin solution (5% in Tween PBS 1X), the membranes being gently rotated overnight at 4 °C. Membranes were then incubated with primary antibodies against Bcl-2, PARP, cdc25c, CDC20, ROCK1, MAD2, p-H2AX^{Ser139}, cyclin B, p-cdc2^{Tyr15}, p-PLK1^{Tyr210} (all from Cell Signaling), caspase-3 (Alexis), or β-actin (Sigma-Aldrich) for 2 h at room temperature. Membranes were next incubated with peroxidase labeled secondary antibodies for 60 min. All membranes were visualized using ECL Select (GE Healthcare), and images were acquired using an Uvitec-Alliance imaging system (Uvitec, Cambridge, UK). To ensure equal protein loading, each membrane was stripped and reprobed with anti-β-actin antibody.

***In vivo* animal studies.**

Procedures involving animals and their care conformed with institutional guidelines that comply with national and international laws and policies (EEC Council Directive 86/609, OJ L 358, 12 December 1987) and with "ARRIVE" guidelines (Animals in Research Reporting In Vivo Experiments). Six week old C57BL/6 mice (Charles River, Calco) were injected subcutaneously into the dorsolateral flank with $2.5x10^5$ BL6-B16 murine melanoma cells in 200 µL-total volume of PBS. When tumors were palpable, animals were treated intraperitoneally every other day with different doses of test compounds dissolved in 50 µL of DMSO. Tumors were measured in two dimensions, and tumor volume was calculated according to the formula $V=(D \times d^2)/2$, where D and d are the major and minor perpendicular tumor diameters, respectively.

Statistical analysis.

Unless indicated differently, the results are presented as mean ± SEM. The differences between different treatments were analyzed, using the two-sided Student's t test. P values lower than 0.05 were considered significant

7. References

[1] Nasmyth, K. Segregating sister genomes: the molecular biology of chromosome separation. *Science* **2002**, *297*, 559-565

[2] Hartwell, L. H.; Kastan, M. B. Cell cycle control and cancer. *Science* **1994**, *266*, 1821-1828

[3] Hartwell, L. H.; Weinert, T. A. Checkpoints: controls that ensure the order of cell cycle events. *Science* **1989**, *246*, 629-634

[4] White, E. Life, death, and the pursuit of apoptosis. *Genes Dev.* **1996**, *10*, 1-15

[5] Sampath, D.; Plunkett, W. Design of new anticancer therapies targeting cell cycle checkpoint pathways. *Curr. Opin. Oncol.* **2001**, *13*, 484-490

[6] Nepali, K.; Ojha, R.; Sharma, S.; Bedi, P. M. S.; Dhar, K. L. Tubulin inhibitors: a patent survey, *Recent Pat. Anticancer Drug Discov*. **2014**, *9*, 1-45.

[7] Jordan, M. A.; Wilson, L. Microtubules as a target for anticancer drugs. *Nature* **2004**, *4*, 253-265.

[8] Mita MM, Sargsyan L, Mita AC, Spear M. Vascular-disrupting agents in oncology. *Expert Opinion on Investigational Drugs*, **2013**, *22 (3)*, 317-328.

[9] Eva Nogales, Sharon G. Wolf & Kenneth H. Downin, Structure of the α,β tubulin dimer by electron crystallography. *Nature*, **1998**, *391*, 199-203.

[10] Ravelli, R. B. G.; Gigant, B.; Curmi, P. A.; Jourdain, I.; Lachkar, S.; Sobel, A.; Knossow, M. Insight into tubulin regulation from a complex with colchicine and a stathmin-like domain. *Nature* **2004**, *428*, 198-202.

[11] Walker, R. A.; O'Brien, E. T.; Pryer, N. K.; Soboeiro, M. F.; Voter, W. A.; Erickson, H. P.; Salmon, E. D. Dynamic instability of individual microtubules analyzed by video light microscopy: Rate constants and transition frequencies. *J. Cell. Biol.* **1988**, *107*, 1437-1448.

[12] Bailly, E.; Bornens, M. Cell biology. Centrosome and cell division. *Nature* **1992**, *355*, 300-3

[13] Justin M. Kollman, Andreas Merdes. Microtubule nucleation by γ-tubulin complexes, *Nature Reviews Molecular Cell Biology*, **2011**, *12*,709-721.

[14] Kueh, H. Y.; Mitchison, T. J. Structural plasticity in actin and tubulin polymer dynamics. *Science* **2009**, *325*, 960-963

[15] S. Honore, E. Pasquier, D. Braguer. Understanding microtubule dynamics for improved cancer therapy. *Cellular and Molecular Life Sciences*, **2005**, *62,(24),*3039–3056.

[16] Mitchison, T.; Kirschner, M. Microtubule assembly nucleated by isolated centrosomes. *Nature* **1984**, *312*, 232-237.

[17] Mitchison, T.; Kirschner, M. Dynamic instability of microtubule growth. *Nature* **1984**, *312*, 237-242

[18] Leung, C. L.; Green, K. J.; Liem, R. K. Plakins: A family of versatile cytolinker proteins. *Trends Cell Biol.* **2002**, *12*, 37-45

[19] Sammak PJ, Gorbsky GJ, Borisy GG. Microtubule dynamics in vivo: a test of mechanisms of turnover. *J Cell Biol* **1987**,*104*: 395–405.

[20] Schulze E, Kirschner M. Microtubule dynamics in interphase cells. *J Cell Biol* **1986** *102*: 1020–1031.

[21] Margolis RL. Role of GTP hydrolysis in microtubule treadmilling and assembly. *Proc Natl Acad Sci USA* **1981**,*78*: 1586–1590.

[22] Andersen, S. S. Spindle assembly and the art of regulating microtubule dynamics by MAPs and Stathmin/Op18. *Trends Cell Biol.* **2000**, *10*, 261-267

[23] Mandelkow, E.; Mandelkow, E. M. Microtubules and microtubule-associated proteins. *Curr. Opin. Cell Biol.* **1995**, *7*, 72-81.

[24] Masson, D.; Kreis, T. E. Binding of E-MAP-115 to microtubules is regulated by cell cycle-dependent phosphorylation. *J. Cell. Biol.* **1995**, *131*, 1015-1024

[25] Ookata, K.; Hisanaga, S. I.; Sugita, M.; Okuyama, A.; Murofushi, H.; Kitazawa, H.; Chari, S.; Bulinski, J. C.; Kishimoto, T. MAP4 is the in vivo substrate for CDC2 kinase in HeLa cells: Identification of an M-phase specific and a cell cycle-independent phosphorylation site in MAP4. *Biochemistry* **1997**, *36*, 15873-15883

[26] Ookata, K.; Hisanaga, S.; Bulinski, J. C. Cyclin B interaction with microtubule-associated protein 4 (MAP4) targets p34cdc2 kinase to microtubules and is a potential regulator of M-phase microtubule dynamics. *J. Cell Biol.* **1995**, *128*, 849-862.

[27] Belmont, L.; Mitchison, T.; Deacon, H. W. Catastrophic revelations about Op18/stathmin. *Trends Biochem. Sci.* **1996**, *21*, 197-198.

[28] Belmont, L. D.; Mitchison, T. J. Identification of a protein that interacts with tubulin dimers and increases the catastrophe rate of microtubules. *Cell* **1996**, *84*, 623-631.

[29] Marklund, U.; Osterman, O.; Melander, H.; Bergh, A.; Gullberg, M. The phenotype of a "Cdc2 kinase target site-deficient" mutant of oncoprotein 18 reveals a role of this protein in cell cycle control. *J. Biol. Chem.* **1994**, *269*, 30626-30635

[30] Marklund, U.; Larsson, N.; Brattsand, G.; Osterman, O.; Chatila, T. A.; Gullberg, M. Serine 16 of oncoprotein 18 is a major cytosolic target for the Ca2+/calmodulin-dependent kinase-Gr. *Eur. J. Biochem.* **1994**, *225*, 53-60

[31] Walczak, C. E.; Mitchison, T. J.; Desai, A. XKCM1: A Xenopus kinesinrelated protein that regulates microtubule dynamics during mitotic spindle assembly. *Cell* **1996**, *84*, 37-47

[32] Mandelkow, E.; Hoenger, A. Structures of kinesin and kinesinmicrotubule interactions. *Curr. Opin. Cell Biol.* **1999**, *11*, 34-44

[33] Wilson L, Jordan MA: Microtubule dynamics: taking aim at a moving target L *Chem Bio***1995***,2*,569-573.

[34] Schiff PB, Horwitz SB: Taxol stabilizes microtubules in mouse fibroblast cells. *Proc Nat/ Acad Sci USA* **1980,** *77*:1561-1565.

[35] Hung DT, Chen J, Schreiber SL: (+)-Discodermolide binds to microtubules in stoichiometric ratio to tubulin dimers, blocks taxol binding and results in mitotic arrest. *Chem Bio***1996***, 3:287-293.*

[36] Dhamodharan RI, Jordan MA, Thrower D, Wilson L, Wadsworth P: Vinblastine suppresses dynamics of individual microtubules in living cells. *Mol Bio/Cell* **1995**, *6*:1215-1229.

[37] Panda D, Jordan MA, Chin K, Wilson L: Differential effects of vinblastine on polymerization and dynamics at opposite microtubule ends. *J Bio/Chem* **1996**, *271*:29807-29812.

[38] Panda D, Daljo JE, Jordan MA, Wilson L: Kinetic stabilization of microtubule dynamics at steady state *in vitro* by substoichiometric concentrations of tubulin-colchicine complex. *Biochemistry* **1995**, *34*:9921-9929.

[39] Mary Ann Jordan, Leslie Wilson. Microtubules and actin filaments: dynamic targets for cancer chemotherapy, *Current Opinion in Cell Biology*, **1998**, *10 (1)*, 123-130.

[40] Jordan MA, Toso R J, Thrower D, Wilson L: Mechanism of mitotic block and inhibition of cell proliferation by taxol at low concentrations. *Proc Natl Acad Sci USA* **1993**, *90*:9552-9556.

[41] Li X, Nicklas RB: Mitotic forces control a cell-cycle checkpoinL *Nature* **1995**, *373*:630-632.

[42] Nicklas RB, Ward SC, Gorbsky G J: Kinetochore chemistry is sensitive to tension and may link mitotic forces to a cell cycle checkpoint. *J Cell Biol* **1995**, *130*:929-939.

[43] Rieder CL, Cole RW, Khodjakov A, Sluder G: The checkpoint delaying anephase in response to chromosome monorientation is mediated by an inhibitory signal produced by unattached kinetchores. *J Cell Bio***1995***, 130*:941-946.

[44] Wendell KL, Wilson L, Jordan MA: Mitotic block in HeLa cells by vinblastine: ultrastructural changes in kinetochore-microtubule attachment and in centrosomes. *J Cell Sci* **1993**, *104*:261-274.

[45] Jordan MA, Thrower D, Wilson L: Effects of vinblastine, podophyllotoxin and nocodezole on mitotic spindles. Implications for the role of microtubule dynamics in mitosis. *J Cell Sci* **1992**, *102*:401-416.

[46] Fukasawa K, Choi T, Kuriyama R, Rulong S, Vande Woude GF: Abnormal centrosome amplification in the absence of p53**.** *Science* **1996**, *271*:1744-1747.

[47] Jordan MA, Wendell KL, Gardiner S, Derry WB, Copp H, Wilson L: Mitotic block induced in HeLa cells by low concentrations of paclitaxel (Taxol) results in abnormal mitotic exit and apoptotic cell death. *Cancer Res* **1996**, *56*:616-625.

[48] Bhalla K, Ilerado AM, Tourkina E, Tang C, Mahoney ME, Huang Y: Taxol induces internucleosomal DNA fragmentation associated with programmed cell death in human myeloid leukemia cells. *Leukemia* **1993**, *7*:563-568.

[49] Donaldson KL, Goolsby G, Kiener PA, Wahl AF: Activation of p34cdc2 coincident with taxol-induced apoptosis. *Cell Growth Differ* **1994**, *5*:1041-1050.

[50] Dumontet, C.; Jordan, M. A. Microtubule-binding agents: a dynamic field of cancer therapeutics *Nat. Rev. Drug Disc*. **2010**, *9*, 790.

[51] Amos, L. A. Semin. What tubulin drugs tell us about microtubule structure and dynamics. *Cell Dev. Biol*. **2011**, *22*, 916.

[52] Wahl, A. F.; Donaldson, K. L.; Fairchild, C. Lee, F. Y. F.; Foster, S. A.; Demers, G. W.; Galloway, D. A. Loss of normal p53 function confers sensitization to Taxol by increasing G2/M arrest and apoptosis. *Nat. Med.* **1996**, *2*, 72-79.

[53] Vikhanskaya, F.; Vignati, S.; Beccaglia, P.; Ottoboni, C.; Russo, P.; D'Incalci, M.; Broggini, M. Inactivation of p53 in a human ovarian cancer cell line increases the sensitivity to paclitaxel by inducing G2/M arrest and apoptosis. *Exp. Cell. Res.* **1998**, *241*, 96-101.

[54] Pries AR, Reglin B. Modeling of angioadaptation: insights for vascular developments, *Int J Biol* **2011**; *55*, 399-405.

[55] Denekamp J. Vascular attack as a therapeutic strategy for cancer, *Cancer Metastasis Rev* **1990**; *9*, 267-282.

[56] Tozer GM, Kanthon C, Baguley BC, Disrupting tumor blood vessels. *Nat Rev Cancer* **2005**; 5, 423-435.

[57] Nogales E, Wolf S. A structure of tubulin at 6.5 Å and location of taxol binding site. *Nature* **1995** *275*, 424-427.

[58] Denis, J. N.; Greene, A. E.; Gue´nard, D.; Gue´ritte-Voegelein, F.; Mangatal, L.; Potier, P. *J. Am. Chem. Soc*. **1988**, *110*, 5917-5919

[59] He, L.; Jagtap, P. G.; Kingston, D. G. I.; Shen, H. J.; Orr, G. A.; Horwitz, S. B. A Common Pharmacophore for Taxol and the Epothilones Based on the Biological Activity of a Taxane Molecule Lacking a C-13 Side Chain. *Biochemistry* **2000**, *39,* 3972-3978

[60] Nicolaou, K. C.; Yang, Z.; Liu, J. J.; Ueno, H.; Nantermet, P. G.; Guy, R. K.; Claiborne, C. F.; Renaud, J.; Couladouros, E. A.; Paulvannan, K.; Sorensin, E. J. Total synthesis of taxol. *Nature* **1994**, *367*, 630-634

[61] Eisenhauer, E. A.; Vermorken, The taxoids. Comparative clinical pharmacology and therapeutic potential *J. B. Drugs* **1998**, *55*, 5-30.

[62] Derry, W.; B.; Wilson, L.; Jordan, M.A. Substoichiometric Binding of Taxol Suppresses Microtubule Dynamics *Biochemistry,* **1995**, *34*, 2203-2211

[63] Caplow, M.; Shanks, J.; Ruhlen, R. How taxol modulates microtubule disassembly, *Biochemistry,* **1994**, *269*, 23399-23402.

[64] Yvon, A.-M.; Wadsworth, P.; Jordan, M.A. Taxol Suppresses Dynamics of Individual Microtubules in Living Human Tumor Cells. *Mol. Biol. Cell,* **1999**, *10*, 947-949

[65] Kingston, D. G. I. Recent Advances in the Chemistry of Taxol. *J. Nat. Prod*. **2000**, *63*, 726-734

[66] Appendino, G.; Dannieli, B.; Jackupovic, J.; Belloro, E.; Scambia, G.; Bomberdelli, E. Synthesis and evaluation of C-seco paclitaxel analogs. *Tetrahedron Lett.* **1997**, *38*, 4273-4276

[67] Parness, J.; Kingston, D. G. I.; Powel, R. C.; Harracksing, C.; Horwitz, S. B. Structure-activity study of cytotoxicity and microtubule assembly in vitro by taxol and related taxanes. *Biochem. Biophys. Res. Commun.* **1982**, *105*, 1082- 1089

[68] Gueritte-Voegelein, F.; Guenard, D.; Lavelle, F.; Le Goff, M. T.; Mangatal, L.; Potier, P. Relationships between the structure of taxol analogs and their antimitotic activity. *J. Med. Chem.* **1991**, *34*, 992-998

[69] Saicic, R. N.; Matovic, R. An efficient semisynthesis of 7-deoxypaclitaxel from taxine. *J. Chem. Soc. Perkin Trans.* **2000**, *1*, 59-65

[70] Ojima, I.; Kuduk, S. D.; Pera, P.; Veith, J. M.; Bernacki, R. J. Synthesis and Structure-Activity Relationships of Non-aromatic Taxoids: Effects of Alkyl and Alkenyl Ester Groups on Cytotoxicity. *J. Med. Chem.* **1997**, *40*, 279-285

[71] Ojima, I.; Slater, J. C.; Kuduk, S. D.; Takeuchi, C. S.; Gimi, R. H.; Sun, C. M.; Park, Y. H.; Pera, P.; Veith, J. M.; Bernacki, R. J. Syntheses and Structure- Activity Relationships of Taxoids Derived from 14β-hydroxy-10-deacetylbaccatin III. *J. Med. Chem.* **1997**, *40*, 267-278

[72] Ojima, I.; Lin, S.; Wang, T. Recent advances in the medicinal chemistry of taxoids with novel β-amino acid side chains. *Curr. Med. Chem.* **1999**, *6*, 927-954.

[73] Moon, C.; Verschraegen, C. F.; Bevers, M.; Freedman, R.; Kudelka, A. P.; Kavanagh, J. J. Use of docetaxel (taxotere) in patients with paclitaxel (taxol) hypersensitivity. *Anti-Cancer Drugs* **2000**, *11*, 565-568

[74] Cheng, Q.; Oritani, T.; Horiguchi, T.; Yamada, T.; Mong, Y. Synthesis and biological evaluation of novel 9-functional heterocyclic coupled 7-deoxy-9- dihydropaclitaxel analogue. *Bioorg. Med. Chem. Lett.* **2000**, *10*, 517-521

[75] Klar, U.; Graf, H.; Schenk, O.; Rohr, B.; Schulz, H. New synthetic inhibitors of microtubule depolymerisation. *Bioorg. Med. Chem. Lett.* **1998**, *8*, 1397- 1402

[76] Huang, C. M.; Wu, Y. T.; Chen, S. T. Targeting delivery of paclitaxel into tumor cells via somatostatin receptor endocytosis. *Chem. Biol.* **2000**, *7*, 453-461

[77] Neuss, N.; Gorman, M.; Svoboda, G. H.; Maciak, G.; Beer, C. T. Vinca alkaloids. III. Characterization of leurosine and vincaleukoblastine, new alkaloids from Vinca rosea. *J. Am. Chem. Soc.* **1959**, *81*, 4754-4755

[78] Svoboda, G. H. Alkaloids of Vinca rosea. IX. Extraction and characterization of leurosidine and leurocristine. *Lloydia* **1961**, *24*, 173-178

[79] Mukherjee, A. K.; Basu, S.; Sarkar, N.; Ghosh, A. C. Advances in cancer therapy with plant based natural products. *Curr. Med. Chem.* **2001**, *8*, 1467-1486

[80] B. Gigant, C. Wang, Raimond B. G. Ravelli, F. Roussi, M. O. Steinmetz, P. A. Curmi, A. Sobel & M. Knossow. Structural basis for the regulation of tubulin by vinblastine, *Nature* **2005**, *435*, 519

[81] Jordan, M.A.; Thrower, D.; Wilson. Mechanism of inhibition of cell proliferation by Vinca Alkaloids. *Cancer Res* **1991**; *51*, 2212-2222.

[82] M. A. Jordan, Mechanism of Action of Antitumor Drugs that Interact with Microtubules and Tubulin, *Curr. Med. Chem. – Anti-Cancer Agents,* **2002***, 2,* 1-17

[83] Pettit, G. R. Progress in the Discovery of Biosynthetic Anticancer Drugs. *J. Nat. Prod.* **1996**, *59*, 812-821

[84] Bensch, K.G.; Malawista, S.E., Microtubule crystals in mammalian cells *J. Cell Biol.,* **1969**, *40*, 95- 107.

[85] Malawista, S.E.; Sato, H. Vinblastine produced uniaxial crystals in starfish oocytes, *J. Cell Biol.,* **1969**, *42*, 596-599

[86] Barnett, C. J.; Cullinan, G. J.; Structure- activity relationships of dimeric Catharanthus alkaloids. 1. Deacetyl vinblastine amide (vindesine) sulfate. *J. Med. Chem.* **1978**, *21*, 88-96

[87] Budman, D. R. New vinca alkaloids and related compounds. *Sem. Oncol.* **1992**,*19*, 639-645.

[88] Canobbio, L.; Boccardo, F; Pastorino, G.; Brema, F.; Martini, C.; Resasco, M.; Santi, L. Phase-II study of Navelbine in advanced breast cancer. *Sem. Oncol.* **1989**, *16*, 33-36.

[89] Martins, R. G.; Dienstmann, R.; de Biasi, Phase II trial of neoadjuvant chemotherapy using alternating doublets in non-small-cell lung cancer. *Clin. Lung Cancer* **2007**, *8*, 257-263

[90] Kruczynski, A.; Etievant, Hill, B. T. Characterization of cell death induced by vinflunine, the most recent Vinca alkaloid in clinical development. *Br. J. Cancer* **2002**, *86*, 143-150

[91] Niel, E.; Scherrmann, J. M. Colchicine today. *Joint Bone Spine* **2006**, *73*, 672-678.

[92] D. A. Skoufias, L. Wilson, Mechanism of inhibition of microtubule polymerization by colchicine: Inhibitory potencies of unliganded colchicine and tubulin-colchicine complexes, *Biochemistry* **1992**, *31*, 738 –746

[93] Bai, R.; Covell, D. G.; Pei, X. F.; Ewell, J. B.; Nguyen, N. Y.; Brossi, A.; Hamel, E. Mapping the binding site of colchicinoids on β-tubulin: 2- chloroacetyl-2-demethylthiocolchicine covalently reacts predominantly with cysteine 239 and secondarily with cysteine 354. *J. Biol. Chem.* **2000**, *275*, 40443-40452

[94] Sapra, S., Bhalla, Y., Nandani, S. Sharmaet, G. Singh, K. Nepali, A. Budhiraja, K. L. Dhar al., Colchicine and its various physicochemical and biological aspects, *Med Chem Res* **2013**, *22*: 531

[95] Ruoli Bai, Xue-Feng Pei, Olivier Boye´, Zelleka Getahun, Surinder Grover, Joseph Bekiszi, Nga Y. Nguyeni, Arnold Brossi¶, and Ernest Hamel. Identification of Cysteine 354 of b-Tubulin as Part of the Binding Site for the A Ring of Colchicine. *The journal of Biol. Chem*. **1996**, *271 (21)*, 12639–12645.

[96] Andreu, J. M.; Perez-Ramirez, B.; Gorbunoff, M. J.; Ayala, D.; Timasheff, S. N. Role of the Colchicine Ring A and Its Methoxy Groups in the Binding to Tubulin and Microtubule Inhibition. *Biochemistry* **1998**, *37*, 8356-8368

[97] Andreu, J. M.; Timasheff, S. N. Conformational states of tubulin liganded to colchicine, tropolone methyl ether, and podophyllotoxin. *Biochemistry* **1982**, *21*, 6465-6476

[98] Bhabatarak Bhattacharyya, Dulal Panda, Suvroma Gupta, Mithu Banerjee. Anti-mitotic activity of colchicine and the structural basis for its interaction with tubulin. *Medicinal Research Rew*. **2008**, *28*, 155-183.

[99] Shi, Q.; Chen, K.; Morris-Natschke, S. L.; Lee, K. H. Recent progress in the development of tubulin inhibitors as antimitotic antitumor agents. *Curr. Pharm. Des.* **1998**, *4*, 219-248

[100] Al-Tel, T. H.; Abu Zarga, M. H.; Sabri, S. S.; Freyer, A. J.; Shamma, M. New natural colchicinoids: indications of two possible catabolic routes for the colchicine alkaloids. *J. Nat. Prod.* **1990**, *53*, 623-629

[101] Hamel, E. Antimitotic natural products and their interactions with tubulin. *Med. Res. Rev.* **1996**, *16*, 207-231

[102] Lee, K. H.; Xiao, Z. Antitumor agents 240. Podophyllotoxins and analogs. *Anticancer Agents Nat. Prod.* **2005**, *1*, 71-87

[103] Ji, Z.; Wang, H. K.; Bastow, K. F.; Zhu, X. K.; Cho, S. J.; Cheng, Y. C.; Lee, K. H. Antitumor agents. 177. Design, syntheses, and biological evaluation of novel etoposide analogs bearing pyrrolecarboxamidino group as DNA topoisomerase II inhibitors. *Bioorg. Med. Chem. Lett.* **1997**, *7*, 607-6

[104] Lee, K. H. Anticancer drug design based on plant-derived natural products. *J. Biomed. Sci.* **1999**, *6*, 236 250

[105] Solary, E.; Leteurtre, F.; Paull, K. D.; Scudiero, D.; Hamel, E.; Pommier, Y. Dual inhibition of topoisomerase II and tubulin polymerization by azatoxin, a novel cytotoxic agent. *Biochem. Pharmacol.* **1993**, *45*, 2449-2456

[106] Y. Shan, J. Zhang, Z. Liu, M. Wang and Y Dong. Developments of Combretastatin A-4 Derivatives as Anticancer Agents, *Current Medicinal Chemistry,***2011**, *18(4)*: 523-538.

[107] Pettit, G. R.; Singh, S. B.; Boyd, M. R.; Hamel, E.; Pettit, R. K.; Schmidt, J. M.; Hogan, F. Antineoplastic Agents. 291. Isolation and Synthesis of Combretastatins A-4, A-5, and A-6. *J. Med. Chem.* **1995**, *38*, 1666-1672.

[108] Pettit, G. R.; Singh, S. B.; Hamel, E.; Lin, C. M.; Alberts, D. S.; Garcia- Kendall, D. Isolation and structure of the strong cell growth and tubulin inhibitor combretastatin A-4. *Experientia* **1989**, *45*, 209-211.

[109] Nabha SM, Mohammad RM, Wall NR, Dutcher JA, Salkini BM, Pettit GR, Al-Katib AM. Evaluation of combretastatin A-4 prodrug in a non-Hodgkin's lymphoma xenograft model: preclinical efficacy. *Anticancer Drugs* **2001**; *12*: 57–63.

[110] Mcgowan AT, Fox BW. Differential cytotoxicity of the combretastatins A1 and A4 in two daunorubicin P388 resistant cell lines. *Cancer Chemother Pharma* **1990**; *26*: 79.

[111] Rajak H, Dewangan PK, Patel V, Jain DK, Singh A, Design of combretastatin A-4 analogs as tubulin targeted vascular disruptingagent with special emphasis on their cis-restricted isomers. *Curr. Pharm. Des*. **2013**, *19*, 1923-1955.

[112] Ter-Haar E, Rosenkranz HS, Hamel E, Day BW. Computational and molecular modeling evaluation of the structural basis for tubulin polymerization inhibition by colchicine site agents. *Bioorg Med Chem* **1996**; *4*: 1659.

[113] K. Ohsumi, R. Nakagawa, Y. Fukuda, T. Hatanaka, Y. Morinaga, Y. Nihei, K. Ohishi, Y. Suga, Y. Akiyama, T. Tsuji. Novel combretastatin analogs effective against murine solid tumors: design and structure-activity, *J Med Chem* **1998**; *41*: 3022-3032

[114] Chaplin DJ, Petti GR, Hill SA. Anti-vascular approaches to solid tumour therapy: evaluation of combretastatin A4 phosphate. *Anticancer Res* **1999**; *19*: 189. (b) West CM, Price P. Combretastatin A4 phosphate. *Anticancer Drugs* **2004**; *15*: 179.

[115] Zweifel, M.; Jayson, G. C.; Reed, N. S.; Osborne, R.; Hassan, B.; Ledermann, J.; Shreeves, G.; Poupard, L.; Lu, S. P.; Balkissoon, J.; Chaplin, D. J.; Rustin, G. J. S. Phase II trial of combretastatin A4 phosphate, carboplatin, and paclitaxel in patients with platinum resistant ovarian cancer. *Ann. Oncol.* **2011**, *22*, 2036-2041

[116] Rustin, G. J.; Shreeves, G.; Nathan, P. D.; Gaya, A.; Ganesan, T. S.; Wang, D.; Boxall, J.; Poupard, L.; Chaplin, D. J.; Stratford, M. R. L.; Balkissoon, J.; Zweifel, M. A. Phase Ib trial of CA4P (combretastatin A-4 phosphate), carboplatin, and paclitaxel in patients with advanced cancer. *Br. J. Cancer*, **2010**, *102*, 1355-1360

[117] Rowinsky, E. K. The development and clinical utility of the taxane class of antimicrotubule chemotherapy agents. *Annu. Rev. Med.* **1997**, *48*, 353-374

[118] Verrills, N. M.; Kavallaris, M. Improving the targeting of tubulin-binding agents: Lessons from drug resistance studies. *Curr. Pharm. Des.* **2005**, *11*, 1719-1733

[119] Pettit, G. R.; Temple, C. Jr.; Narayanan, V. L.; Varma, R.; Boyd, M. R.; Rener, G. A.; Bansal, N. Antineoplastic agents 322. Synthesis of combretastatin A-4 prodrugs. *Anti-Cancer Drug Des.* **1995**, *10*, 299-309

[120] Siemann, D. W.; Chaplin, D. J.; Walike, P. A. A review and update of the current status of the vasculature-disabling agent combretastatin-A4 phosphate (CA4P). *Expert Opin. Investig. Drugs* **2009**, *18*, 189-197

[121] Romagnoli, R.; Baraldi, P. G.; Carrion, M. D.; Cruz-Lopez, O.; Lopez-Cara, C.; Basso, G.; Viola, G.; Khedr, M.; Balzarini, J.; Mahboobi, S.; Sellmer, A.; Brancale, A.; Hamel, E. 2-Arylamino-4-amino-5-aroylthiazoles. "One-pot" synthesis and biological evaluation of a new class of inhibitors of tubulin polymerization. *J. Med. Chem.* **2009**, *52*, 5551-5555

[122] Moreira Lima, L.; Barreiro, E. J. Bioisosterism: a useful strategy for molecular modification and drug design. *Curr. Med. Chem.* **2005**, *12*, 23-49

[123] Lange, J. H. M.; van Stuivenberg, H. H.; Coolen, H. K. A. C.; Adolfs, T. J. P.; McCreary, A. C.; Keizer, H. G.;. Wals, H. C.; Veerman, W.; Borst, A. J. M. ; de Looff, W.; Verveer, P. C.; Kruse, C. G. Bioisosteric replacements of the pyrazole moiety of rimonabant: Synthesis, biological properties, and molecular modeling investigations of thiazoles, triazoles, and imidazoles as potent and selective CB1 cannabinoid receptor antagonists. *J. Med. Chem.* **2005**, *48*, 1823-1838

[124] For anticancer molecules based on the 1,2,4-triazole ring see: a) Zhang, Q.; Peng, Y.; Wang, X. I.; Keeman, S. M.; Aurora. S.; Welsh, W. J. Highly potent triazole-based tubulin polymerization inhibitors. *J. Med. Chem.* **2007**, *50*, 749-754, b) Romagnoli, R.; Baraldi, P. G.; Cruz-Lopez, O.; Lopez-Cara, C.; Carrion, M. D.; Brancale, A.; Hamel, E.; Chen, L.; Bortolozzi, R.; Basso, G.; Viola, G. Synthesis and antitumor activity of 1,5-disubstituted 1,2,4-triazoles as *cis*-restricted combretastatin analogs. *J. Med. Chem.* **2010**, *53*, 4248-4258; c) Ouyang, X.; Chen, X.; Piatnitski, E. L.; Kiselyov, A. S.; He, H.-Y.; Mao, Y.; Pattaropong, V.; Yu, Y.; Kim, K. H.; Kincaid, J.; Smith II, L.; Wong, W. C.; Lee, S. P.; Milligan, D. L.; Malikzay, A.; Fleming, J.; Gerlak, J.; Deevi, D.; Doody, J. F.; Chiang, H.-H.; Patel, S. N.; Wang, Y.; Rolser, R. L.; Kussie, P.; Labelle, M.; Tuma, M. C. Synthesis and structure-activity relationships of 1,2,4-triazoles as a novel class of potent tubulin polymerization inhibitors. *Bioorg. Med. Chem. Lett.* **2005**, *15*, 5154-5158; d) Ohsumi, K.; Hatanaka, T.; Fujita, K.; Nakagawa, R.; Fukuda, Y.; Nihai, Y.; Suga, Y.; Morinaga, Y.; Akiyama, Y.; Tsuji, T. Synthesis and antitumor activity of *cis*-restricted combretastatins 5-membered heterocyclic analogues. *Bioorg. Med. Chem. Lett.* **1988**, *8*, 3153-3158; e) Shi, Y.-J., Song, X.-J.; Li, X.; Ye, T.-H.; Xiong, Y.; Yu, L.-T. Synthesis and biological evaluation of 1,2,4-triazole and 1,3,4-thiadiazole derivatives as potential cytotoxic agents. *Chem. Pharm. Bull.* **2013**, *61*, 1099-1104; f) Singha, T., Singh, J.; Naskar, A.; Ghosh, T.;

Mondal, A.; Kundu, M.; Harwansh, R. K.; Maity, T. K. Synthesis and evaluation of antiproliferative activity of 1,2,4-triazole derivatives against EAC bearing mice model. *Ind. J. Pharm. Edu. Res.* **2012**, *46*, 346-351; g) Li, X., li, X.-Q.; Liu, H.-M.; Zhou, X.-Z.; Shao, Z.-H. Synthesis and evaluation of antitumor activities of novel chiral 1,2,4-triazole Schiff bases bearing γ-butenolide moiety. *Org. Med. Chem. Lett.* **2012**, *2*, 26-31

[125] a) Gaukroger, K.; Hadfield, J. A.; Lawrence, N. J.; Nlan, S.; McGown, A. T. Structural requirements for the interaction of combretastatins with tubulin: how important is the trimethoxy unit? *Org. Biomol. Chem.* **2003**, *1*, 3033-3037; b) Cushman, M.; Nagarathnam, D.; Gopal, D.; He, H.-M.; Lin, C. M.; Hamel, E. Synthesis and evaluation of analogues of (Z)-1-(4-methoxyphenyl)-2-(3,4,5-trimethoxyphenyl)ethene as potential cytotoxic and antimitotic agents. *J. Med. Chem.* **1992**, *35*, 2293-2306

[126] Thomae, D.; Perspicace, E.; Hesse, S.; Kirsch, G.; Seck, P. Synthesis of substituted [1,3]thiazolo[4,5-*d*][1,2.3]triazines. *Tetrahedron*, **2008**, *64*, 9306-9314

[127] Webb, R. L.; Eggleston, D. S.; Labaw, C. S.; Lewis, J. J.; Wert, K. Diphenyl cyancarbonimidate and dichlorodiphenoxymethane as synthons for the construction of heterocyclic systems of medicinal interest. *J. Heterocycl. Chem.* **1987**, *24*, 275-278

[128] Szakács, G.; Paterson, J.K.; Ludwig, J.A.; Booth-Genthe, C.; Gottesman, M.M. Targeting multidrug resistance in cancer. *Nat. Rev. Drug Discov*. **2006**, 5, 219-234

[129] Baguley B.C. Multidrug resistance mechanism in cancer. *Mol. Biotechnol.* **2010**, *46*, 308-316

[130] Toffoli, G.; Viel, A.; Tumiotto, I.; Biscontin, G.; Rossi, G.; Boiocchi, M. Pleiotropic-resistant phenotype is a multifactorial phenomenon in human colon carcinoma cell lines. *Br. J. Cancer* **1991**, *63*, 51–56

[131] Dupuis, M.; Flego, M.; Molinari, A.; Cianfriglia, M. Saquinavir induces stable and functional expression of the multidrug transporter P-glycoprotein in human CD4 T-lymphoblastoid CEM rev cells. *HIV Medicine* **2003,** *4*, 338–345

[132] Clarke, P. R.; Allan, L. A. Cell-cycle control in the face of damage- a matter of life or death. *Trends Cell Biol.* **2009**, *19*, 89-98

[133] Mollinedo, F.; Gajate, C. Microtubules, microtubule-interfering agents and apoptosis. *Apoptosis* **2003**, *8*, 413-450

[134] Ganem, N. J.; Pellman, D. Linking abnormal mitosis to the acquisition of DNA damage. *J Cell Biol.* **2012**, *199*, 871-881

[135] Orth, J. D.; Loewer, A.; Lahav, G.; Mitchison, T. J. Prolonged mitotic arrest triggers partial activation of apoptosis, resulting in DNA damage and p53 induction. *Mol Biol Cell*. **2012,** *23*, 567-576

[136] Fernandez-Capetillo, O.; Lee, A.; Nussenzweig, M.; Nussenzweig, A. H2AX: the histone guardian of the genome. *DNA Repair* **2004**, *3*, 959-967

[137] Weiss, R. H. p21Waf1/Cip1 as a therapeutic target in breast and other cancers *Cancer Cell* **2003,** *4*, 425-429

[138] Vermes, I.; Haanen, C.; Steffens-Nakken, H.; Reutelingsperger, C. A novel assay for apoptosis. Flow cytometric detection of phosphatidylserine expression on early apoptotic cells using fluorescein labelled annexin V. *J. Immunol. Methods* **1995**, *184*, 39-51

[139] Baeriswyl, V.; Christofori, G. The angiogenic switch in carcinogenesis. *Semin. Cancer Biol.* **2009**, *19*, 329-337

[140] Siemann, D.; Bibby, M.; Dark, G. Differentiation and definition of vascular-targeted therapies. *Clin. Cancer Res.* **2005**, *2*, 416-420

[141] Kanthou, C.; Tozer, G. M. The tumor vascular targeting agent combretastatin A-4-phosphate induces reorganization of the actin cytoskeleton and early membrane blebbing in human endothelial cells. *Blood* **2002**, *99*, 2060-2069

[142] Bergers, G.; Benjamin L, E. Tumorigenesis and the angiogenic switch. *Nat. Rev. Cancer*. **2003**, *3*, 401-410

[143] Guidolin, D.; Vacca, A.; Nussdorfer, G. G.; Ribatti, D. A new image analysis method based on topological and fractal parameters to evaluate the angiostatic activity of docetaxel by using the Matrigel assay in vitro. *Microvasc. Res.* **2004**, *67*, 117-124

[144] Porcù, E.; Viola, G.; Bortolozzi, R.; Mitola, S.; Ronca, R.; Presta, M.; Persano, L.; Romagnoli, R.; Baraldi, P. G.; Basso, G. TR-644 a novel potent tubulin binding agent induces impairment of endothelial cells function and inhibits angiogenesis. *Angiogenesis* **2013**, *16*, 647-662

[145] Gasparotto, V.; Castagliuolo, I.; Chiarelotto, G.; Pezzi, V.; Montanaro, D.; Brun, P.; Palù, G.; Viola, G., Ferlin, M. G. Synthesis and biological activity of 7-phenyl-6,9-dihydro-3H-pyrrolo[3,2-*f*]quinolin-9-ones: a new class of antimitotic agents devoid of aromatase activity. *J. Med. Chem*. **2006**, *49*, 1910-1915

[146] Altomare, A.; Burla, M. C.; Camalli, M.; Cascarano, G.; Giacovazzo, C.; Guagliardi, A.; Moliterni, A. G:, Polidori, G:; Spagna, R. *SIR*97: a new tool for crystal structure determination and refinement. *J. Appl. Crystallogr*. **1999**, *32*, 115-121

[147] Sheldrick, G. M. SHELXL-97, *Program for Refinement of Crystal Structures*. University of Göttingen, Germany, **1997**

[148] Romagnoli, R.; Baraldi, P. G.; Kimatrai Salvador, M.; Brancale, A.; Fu, X-H.; Li, J.; Zhang, S.-Z.; Hamel, E.; Bortolozzi, R.; Basso, G.; Viola, G. Synthesis and evaluation of 1,5-disubstituted tetrazoles as rigid analogues of combretastatin A-4 with potent antiproliferative and antitumor activity. *J. Med. Chem.* **2012**, *55*, 475-488

[149] a) Hamel, E. Evaluation of antimitotic agents by quantitative comparisons of their effects on the polymerization of purified tubulin. *Cell Biochem. Biophys.* **2003**, *38*, 1-21; b) Verdier-Pinard, P.; Lai J.-Y.; Yoo, H.-D.; Yu, J.; Marquez, B.; Nagle D.G.; Nambu, M.; White, J.D.; Falck, J.R.; Gerwick, W.H.; Day, B.W.; Hamel, E. Structure-activity analysis of the interaction of curacin A, the potent colchicine site antimitotic agent, with tubulin and effects of analogs on the growth of MCF-7 breast cancer cells. *Mol. Pharmacol.* **1998**, *53*, 62-67

[150] Molecular Operating Environment (MOE 2008.10). Chemical Computing Group, Inc. Montreal, Quebec, Canada. http://www.chemcomp.com

[151] Korb, O.; Stützle, T.; Exner, T. E. PLANTS: Application of ant colony optimization to structure-based drug design. In Dorigo, M.; Gambardella, L. M.; Birattari, M.; Martinoli, A.; Poli, R.; Stützle, T. (Eds.). *Ant Colony Optimization and Swarm Intelligence*, 5th International Workshop, ANTS 2006, Springer: Berlin, **2006**; LNCS 4150, pp 247-258

[152] Liang, C. C.; Park, A. Y; Guan, J. L. In vitro scratch assay: a convenient and inexpensive method for analysis of cell migration in vitro. *Nat Protoc*. **2007, *2*,** 329-333

[153] McGown, A. T.; Fox, B. W. Differential cytotoxicity of combretastatins A1 and A4 in two daunobucin-resistant P388 cell lines. *Cancer Chemother. Pharmacol.* **1990**, *26*, 79-81

[154] Kamal, A.; Reddy, N. V. S.; Nayak, V. L.; Reddy, V. S.; Prasad, B.; Nimbarte, V. D.; Srinivasulu, V.; Vishunuvardhan, M. V. P. S.; Reddy, C. S. Synthesis and biological evaluation of benzo[*b*]furans as inhibitors of tubulin polymerization and inducers of apoptosis. *ChemMedChem* **2014**, *9*, 117-128

[155] Romagnoli, R.; Baraldi, P. G.; Sarkar, T.; Carrion, M. D.; Cruz-Lopez, O.; Lopez-Cara, C.; Tolomeo, M.; Grimaudo, S.; Di Cristina, A.; Pipitone, M. R.; Balzarini, J.; Gambari, R.; Lampronti, I.; Saletti, R.; Brancale, A.; Hamel, E.. Synthesis and biological evaluation of 2-(3',4',5'-trimethoxybenzoyl)-3-*N,N*-dimethylamino benzo[*b*]furan derivatives as inhibitors of tubulin polymerization. *Bioorg. Med. Chem.* **2008**, *16*, 8419-8426

[156] Romagnoli, R.; Baraldi, P. G.; Lopez Cara, C.; Cruz-Lopez, O.; Carrion, M. D.; Kimatrai Salvador, M.; Bermejo, J., Estévez , S.; Estévez , F.; Balzarini, J.; Brancale, A.; Ricci, A.; Chen, L.; Gwan Kim, J.; Hamel, E. Synthesis and antitumor molecular mechanism of agents based on amino 2-(3',4',5'-trimethoxybenzoyl)-benzo[*b*]furan: inhibition of tubulin and induction of apoptosis. *ChemMedChem* **2011**, *6*, 1841-1853

[157] Flynn, B. L.; Hamel, E.; Jung, M. K. One-pot synthesis of benzo[*b*]furan and indole inhibitors of tubulin polymerization. *J. Med. Chem.* **2002**, *45*, 2670-2673

[158] Flynn, B. L.; Gill, G. S.; Grobelny, D. S.; Chaplin, J. H.; Paul, D.; Leske, A. F.; Lavranos, T. C.; Chalmers, D. K.; Charman, S. A.; Kostewicz, E.; Shackleford, D. M.; Morizzi, J.; Hamel, E.; Jung, M. K.; Kremmidiotis, G. Discovery of 7-hydroxy-6-methoxy-2-methyl-3 (3,4,5-trimethoxybenzoyl)benzo[*b*]furan (BNC 105), a tubulin polymerization inhibitor with potent antiproliferative and tumor vascular disrupting properties. *J. Med. Chem.* **2011**, *5*4, 6014-6027

[159] Kremmidiotis, G.; Leske, A. F.; Lavranos, T. C.; Beaumont, D.; Gasic, J.; Hall, A.; O'Callaghan, M.; Matthews, C. A.; Flynn, B. L. BNC105: a novel tubulin polymerization inhibitor that selectively disrupts tumor vasculature and displays single-agent antitumor efficacy. *Mol. Cancer Ther.* **2010**, *9*, 1562–1573

[160] Chaplin, J. H.; Gill, G. S.; Grobelny, D. W.; Flynn, B. L.; Kremmidiotis, G. Substituted benzofurans, benzothiophenes, benzoselenophenes and indoles and their use as tubulin polymerization inhibitors. PCT Int. Appl. WO2007087684, **2007**

[161] Hamel, E. Evaluation of antimitotic agents by quantitative comparisons of their effects on the polymerization of purified tubulin. *Cell Biochem. Biophys.* **2003**, *38*, 1-21

[162] Bhattacharyya, B.; Panda, D.; Gupta, S.; Banerjee, M. Antimitotic activity of colchicine and the structural basis for its interaction with tubulin. *Med. Res. Rev.* **2008**, *28*, 155-183

[163] Verdier-Pinard, P.; Lai J.-Y.; Yoo, H.-D.; Yu, J.; Marquez, B.; Nagle, D. G.; Nambu, M.; White, J. D.; Falck, J. R.; Gerwick, W. H.; Day, B. W.; Hamel, E. Structure-activity analysis of the interaction of curacin A, the potent colchicine site antimitotic agent, with tubulin and effects of analogs on the growth of MCF-7 breast cancer cells. *Mol. Pharmacol.* **1998**, *53*, 62-76

[164] Massarotti, A.; Coluccia, A.; Silvestri, R.; Sorba, G.; Brancale, A., The tubulin colchicine domain: a molecular modeling perspective. *ChemMedChem* **2012,** *7*, 33-42

[165] Clarke, P. R.; Allan, L. A. Cell-cycle control in the face of damage- a matter of life or death. *Trends Cell Biol.* **2009**, *19*, 89-98

[166] a) Kiyokawa H.; Ray, D. In vivo roles of cdc25 phosphatases: biological insight into the anti-cancer therapeutic targets. *Anticancer Agents Med. Chem*. **2008**, *8,* 832-836. b) Donzelli, M.; Draetta, G. F. Regulating mammalian checkpoints through Cdc25 inactivation. *EMBO Rep.* **2003**, *4*, 671-677

[167] Vermes, I.; Haanen, C.; Steffens-Nakken, H.; Reutelingsperger, C. A novel assay for apoptosis. Flow cytometric detection of phosphatidylserine expression on early apoptotic cells using fluorescein labelled annexin V. *J. Immunol. Methods* **1995**, *184*, 39-51

[168] Rovini, A.; Savry, A.; Braguer, D.; Carré, M. Microtubule-targeted agents: when mitochondria become essential to chemotherapy. *Biochim. Biophys. Acta* **2011**, *1807,* 679-88

[169] Chiu, W. H.; Luo, S. J.; Chen, C. L.; Cheng, J. H.; Hsieh, C. Y.; Wang, C. Y.; Huang, W. C.; Su, W. C.; Lin, C. F. Vinca alkaloids cause aberrant ROS-mediated JNK activation, Mcl-1 downregulation, DNA damage, mitochondrial dysfunction, and apoptosis in lung adenocarcinoma cells. *Biochem. Pharmacol.* **2012**, *83*, 1159-1171

[170] Romagnoli, R; Baraldi, P.G.; Cruz-Lopez, O.; Lopez Cara C.; Carrion, M.D.; Brancale, A.; Ricci, A.; Hamel, E.; Bortolozzi, R.; Basso, G.; Viola, G. Convergent synthesis and biological evaluation of 2-amino-4-(3',4',5'-trimethoxyphenyl)-5-aryl thiazoles as microtubule targeting agents. *J. Med. Chem.* **2011**, *54*, 5144-5153

[171] a) Cai, J.; Jones, D. P. Superoxide in apoptosis. Mitochondrial generation triggered by cytochrome *c* loss. *J. Biol. Chem.* **1998**, *273*, 11401-11404; b) Nohl, H.; Gille, L.; Staniek, K. Intracellular generation of reactive oxygen species by mitochondria. *Biochem. Pharmacol.* **2005**, *69*, 719-723

[172] Soldani, C.; Scovassi, A. Poly(ADP-ribose) polymerase cleavage during apoptosis: an update. *Apoptosis* **2002**, *74*, 321-328

[173] a) Matson, D. R.; Stukenberg, P. T. Spindle poisons and cell fate: a tale of two pathways. *Mol. Interv*. **2011**, *11*, 141-150. b) Wertz, I. E.; Kusam, S.; Lam, C.; Okamoto, T.; Sandoval, W.; Anderson, D. J.; Helgason, E.; Ernst, J. A.; Eby, M.; Liu, J.; Belmont, L. D.; Kaminker, J. S.; O'Rourke, K. M.; Pujara, K.; Kohli, P. B.; Johnson, A. R.; Chiu, M. L.; Lill, J. R., Jackson, P. K.; Fairbrother, W. J.; Seshagiri, S.; Ludlam, M. J.; Leong, K. G.; Dueber, E. C.; Maecker, H., Huang, D. C.; Dixit, V. M. Sensitivity to antitubulin chemotherapeutics is regulated by MCL1 and FBW7. *Nature* **2011** *471*, 110-114.

[174] Dorleans, A.; Gigant, B.; Ravelli, R. B.; Mailliet, P.; Mikol, V.; Knossow, M., Variations in the colchicine-binding domain provide insight into the structural switch of tubulin. *Proc. Natl Acad. Sci. U. S. A.* **2009,** *106*, 13775-13779

[175] Pistollato, F.; Abbadi, S.; Rampazzo, E.; Viola, G.; Della Puppa, A.; Cavallini, L.; Frasson, C.; Persano, L.; Panchision, D.M.; Basso, G. Succinate and hypoxia antagonizes 2-deoxyglucose effects on glioblastoma. *Biochem. Pharmacol.* **2010**, *80*, 1517-1527

[176] Liang, C.C.; Park, A.Y; Guan, J.L. In vitro scratch assay: a convenient and inexpensive method for analysis of cell migration in vitro. *Nat. Protoc*. **2007,** *2*, 329-333

[177] Pettit, G.R.; Singh, S.B.; Hamel, E.; Lin, C.M.; Alberts, D.S.; Garcia-Kendall, D. Isolation and structure of the strong cell growth and tubulin inhibitor combretastatin A-4. *Experientia* **1989**, *45*, 209-211.

[178] Nathan, P.; Zweifel, M.; Padhani, A. R.; Koh, D.-M.; Ng, M.; Collins, D. J.; Harris, A.; Carden, C.; Smythe, J.; Fisher, N.; Taylor, N. J.; Stirling, J. J.; Lu, S.-P.; Leach, M. O.; Rustin, G. J. S.; Judson, I. Phase I trial of combretastatin A4 phosphate (CA4P) in combination with bevacizumab in patients with advanced cancer. *Clin. Cancer Res.* **2012**, *18*, 3428-3439.

[179] Wang, L.; Woods, K. W.; Li, Q.; Barr, K. J.; McCroskey, R. W.; Hannick, S. M.; Gherke, L.; Credo, R. B.; Hui, Y.-H.; Marsh, K.; Warner, R.; Lee, J. Y.; Zielinski-Mozng, N.; Frost, D.; Rosenberg, S. H.; Sham, H. L. Potent, orally active heterocycle-based combretastatin A-4 analogues: synthesis, structure-activity relationship, pharmaokinetics, and in vivo antitumor activity evaluation. *J. Med. Chem.* **2002**, *45*, 1697-1711.

[180] Bellina, F., Cauteruccio, S., Monti, S. & Rossi, R. Novel imidazole-based combretastatin A-4 analogues: Evaluation of their in vitro antitumor activity and molecular modeling study of their binding to the colchicine site of tubulin. *Bioorg. Med. Chem. Lett.* **2006**,*16*, 5757-5762.

[181] Wang, F.; Yang, Z.; Liu, Y.; Ma, L.; Wu, Y.; He, L.; Shao, S.; Yu, K.; Wu, W.; Pu, Y.; Nie, C.; L. Chen, L. Synthesis and biological evaluation of diarylthiazole derivatives as antimitotic and antivascular agents with potent antitumor activity. *Bioorg. Med. Chem.* **2015**, *23*, 3337-3350.

[182] Tron, G. C., Pagliai, F., Sel Grosso, E., Genazzani, A. A. & Sorba, G. Synthesis and cytotoxic evaluation of combretafurazans. *J. Med. Chem.* **2005**, *48*, 3260-3258.

[183] Liu, T.; Dong, X.; Xue, N.; Wu, R.; He, Q.; Yang, B.; Hu, Y. Synthesis and biological evaluation of 3,4-biaryl-5-aminoisoxazole derivatives. *Bioorg. Med. Chem.* **2009**, *17*, 6279-6285.

[184] Wu, M.; Li, W.; Yang, C.; Chen, D.; Ding, J.; Chen, Y.; Lin, L.; Xie, Y. Synthesis and activity of combretastatin A-4 analogues: 1,2,3-thiadiazoles as potent antitumor agents. *Bioorg. Med. Chem. Lett.* **2007**, *17*, 869-873.

[185] Madadi, N. R.; Penthala, N. R.; Howk, K.; Ketkar, A.; Eoff, R. L.; Borrelli, M. J.; Crooks, P. A. Synthesis and biological evaluation of novel 4,5-disubstituted 2*H*-1,2,3-triazoles as *cis*-constrained analogues of combretastatin A-4. *Eur. J. Med. Chem.* **2015**, *103*, 123-132.

[186] Theeramunkong, S.; Caldarelli, A.; Massarotti, A.; Aprile, S.; Caprifoglio, D.; Zaninetti, R.; Teruggi, A.; Pirali, T.; Grosa, G.; Tron, G. C.; Genazzani, A. A. Regioselective Suzuki coupling of dihaloheteroaromatic compounds as a rapid strategy to synthesize potent rigid combretastatin analogues. *J. Med. Chem.* **2011**, *54*, 4977-4986.

[187] Zhu, L.; Guo, P.; Li, G.; Lan, J.; Xie, R.; You, J. Simple copper salt-catalyzed N-arylation of nitrogen-containing heterocycles with aryl and heteroaryl halides. *J. Org. Chem.* **2007**, *72*, 8535-8538.

[188] Romagnoli, R.; Baraldi, P.G.; Salvador, M.K.; Prencipe, F.; Bertolasi, V.; Cancellieri, M.; Brancale, A.; Hamel, E.; Castagliuolo, I.; Consolaro, F.; Porcù, E.; Basso, G.; Viola, G. Synthesis, antimitotic and antivascular activity of 1-(3′,4′,5′-trimethoxybenzoyl)-3-arylamino-5-amino-1,2,4-triazoles. *J. Med. Chem.* **2014**, *57*, 6795-6808.

[189] Adasme-Carreño, F., Muñoz-Guiterrez, C., Caballero, J. & Alzate-Morales, J.H. Performace of the MM/GBSA scoring using a binding site hydrogen bond network-based frame selection: the protein kinase case. *Phys. Chem. Chem. Phys.* **2014**, *16*, 14047-14058.

[190] Schrödinger Release 2014-4: Prime, version 3.8, Schrödinger, LLC, New York, NY, (**2014**).

[191] Goto, H; Tomono, Y.; Ajiro, K.; Kosako H.; Fujita M.; Sakurai, M.; Okawa K.; Iwamatsu, A.; Okigaki, T.; Takahashi, T., Inagaki, M. Identification of a novel phosphorylation site on histone H3 coupled with mitotic chromosome condensation. *J. Biol. Chem.* **1999**, *274*, 25543-25549.

[192] Weaver, B. A. A. & Cleveland, D. W. Decoding the links between mitosis, cancer, and chemotherapy: the mitotic checkpoint, adaptation, and cell death. *Cancer Cell* **2005**, *8*, 7-12.

[193] Musacchio, A. & Salmon E. D. The spindle-assembly checkpoint in space and time. *Nat. Rev. Mol. Cell Biol.* **2007**, *8*, 379-393.

[194] Van Vugt, M. A. T. M., Brás, A. & Medema, R.H. Polo-like kinase-1 controls recovery from a G2 DNA damage-induced arrest in mammalian cells. *Mol. Cell*, **2004**, *15*, 799-811.

[195] Degenhardt, Y. & Lampkin, T. Targeting polo-like kinase in cancer therapy. *Clin. Cancer Res.* **2010**, *16*, 384-389.

[196] Tsvetkov, L. & Stern, D. F. Phosphorylation of PLK1 at S137 and T210 is inhibited in response to DNA damage. *Cell Cycle* **2005**, *4*, 166-171.

[197] Fernandez-Capetillo, O., Lee, A., Nussenzweig, M. & Nussenzweig, A. H2AX: the histone guardian of the genome. *DNA Repair* **2004**, *3*, 959-967.

[198] Julian, L. & Olson, M. F. Rho-associated coiled-coil containing kinases (ROCK): structure, regulation, and functions. *Small GTPases* **2014**, *5*, 29846.

[199] Sebbagh, M.; Renvoizé, C.; Hamelin, J.; Riché, N.; Bertoglio, J.; Bréard, J. Caspase-3-mediated cleavage of ROCK I induces MLC phosphorylation and apoptotic membrane blebbing. *Nat. Cell Biol.* **2001**, *3*, 346-352.

[200] Xiong, S., Mu, T., Wang, G., Jiang, X. Mitochondria-mediated apoptosis in mammals. *Protein Cell* **2014**, *5*, 737-749.

[201] Rovini, A., Savry, A., Braguer, D. & Carré, M. Microtubule-targeted agents: when mitochondria become essential to chemotherapy. *Biochim. Biophys. Acta-Bioenerg.* **2011**, *1807*, 679-688.

[202] Mendez, G., Policarpi, C., Cenciarelli, C., Tanzarella, C. & Antoccia, A. Role of Bim in apoptosis induced in H460 lung tumor cells by the spindle poison combretastatin-A4. *Apoptosis*. **2011**, *16*, 940-949.

[203] Zamzami, N.; Marchetti, P.; Castedo, M.; Decaudin, D.; Macho, A.; Hirsch, T.; Susin, S.A.; Petit, P.X.; Mignotte, B.; Kroemer, G. Sequential reduction of mitochondrial transmembrane potential and generation of reactive oxygen species in early programmed cell death. *J. Exp. Med*. **1995**, *182*, 367-377.

[204] Wertz, I.E.; Kusam, S.; Lam, C.; Okamoto, T.; Sandoval, W.; Anderson, D. J.; Helgason, E.; Ernst, J. A.; Eby, M.; Liu, J.; Belmont, L. D.; Kaminker, J. S.; O'Rourke, K. M.; Pujara, K.; Kohli, P. B.; Johnson, A. R.; Chiu, M. L.; Lill, J. R., Jackson, P. K.; Fairbrother, W. J.;

Seshagiri, S.; Ludlam, M. J.; Leong, K. G.; Dueber, E. C.; Maecker, H.; Huang, D. C.; Dixit, V. M. Sensitivity to antitubulin chemotherapeutics is regulated by MCL1 and FBW7. *Nature* **2011**, *471*, 110-114.

[205] Czabotar, P. E., Lessene, G., Strasser, A. & Adams, J.M. Control of apoptosis by the BCL-2 protein family: implications for physiology and therapy. *Nature Rev. Mol. Cell Biol*. **2014**, *15*, 49-63.

[206] Ronca, R.; Di Salle, E.; Giacomini, A.; Leali, D.; Alessi, P.; Coltrini, D.; Ravelli, C.; Matarazzo, S.; Ribatti, D.; Vermi, W.; Presta, M. Long Pentraxin-3 inhibits epithelial-mesenchymal transition in melanoma cells. *Mol. Cancer Ther.* **2013**, *12*, 2760-2771.

[207] Schrödinger Release 2014-1: Desmond Molecular Dynamics System, version 3.7, D. E. Shaw Research, New York, NY, 2014. Maestro-Desmond Interoperability Tools, version 3.7, Schrödinger, New York, NY, (**2014**).

Acknowlegments

Prof. Pier Gionanni Baraldi, Prof. Romeo Romagnoli, Dott. Mojgan Aghazadeh Tabrizi, Dott. Stefania Baraldi, Dott. Delia Preti, Dipartimento di scienze chimiche e farmaceutiche, Università di Ferrara, Italy.

Prof. Andrea Brancale, Prof. Andrew Westwell, Dott. Salvatore Ferla, School of Pharmacy and Pharmaceutical Sciences, Cardiff University UK.

Prof. Luisa Carlota Lopez-Cara, Departamento de Quimica Organica y Farmaceutica, Facultad de Farmacia, Campus de Cartuja s/n, 18071, Granada, Spain

Ernest Hamel, National Cancer Institute, National Institutes of Health, Frederick, Maryland, USA

Giuseppe Basso and Giampietro Viola, Dipartimento di Salute della Donna e del Bambino, Laboratorio di Oncoematologia, Università di Padova, Italy.